HAW HAMBURG

BACHELORTHESIS
Niklas Frewer

Development of a phased array antenna demonstrator for 5.6 GHz

FAKULTÄT TECHNIK UND INFORMATIK
Department Informations- und Elektrotechnik

Faculty of Computer Science and Engineering
Department of Information and Electrical Engineering

HOCHSCHULE FÜR ANGEWANDTE WISSENSCHAFTEN HAMBURG
Hamburg University of Applied Sciences

Niklas Frewer

Development of a phased array antenna demonstrator for 5.6 GHz

Bachelorthesis based on the examination and study regulations
for the Bachelor of Science in Electrical Engineering and Information Technology
at the Department of Information and Electrical Engineering
of the Faculty of Engineering and Computer Science
of the Hamburg University of Applied Sciences

Supervising examiner: Prof. Dr.-Ing. Ralf Wendel
Second examiner: Prof. Dr. Annabella Rauscher-Scheibe

Day of delivery: 25.08.2021

Niklas Frewer

Thema der Arbeit

Entwicklung eines Phased Array Antennen-Demonstrators für 5.6 GHz

Stichworte

Phased Array Antenne, Microstrip Antenne, Phasenschieber, Speisenetzwerk

Kurzzusammenfassung

In dieser Thesis wird ein Antennen-Demonstrator entwickelt, dessen Abstrahlrichtung elektronisch gesteuert werden kann. Die Phasen der Einzelelemente des planaren Arrays können mit einem Phasenschieber eingestellt werden. Auf diese Weise kann die Abstrahlrichtung der Antenne bis zu 20 ° im Raum geschwenkt werden. Der Demonstrator ist für 5,6 GHz in Microstrip Form entwickelt.

Niklas Frewer

Title of Thesis

Development of a phased array antenna demonstrator for 5.6 GHz

Keywords

Phased array antenna, Microstrip antenna, Phase shifter, Feed network

Abstract

In this thesis, an antenna demonstrator is developed whose radiation can be electronically controlled. The phase excitation of each individual element of the planar antenna can be adjusted with a phase shifter. In this way the radiation of the antenna can be scanned up to 20 ° in the hemisphere. The demonstrator is developed for 5,6 GHz in microstrip form.

Contents

List of Figures

List of Tables

1 Introduction

1.1 Objective of the thesis

The objective of this work is to develop a planar phased array antenna demonstrator. The demonstrator shall be developed for a center frequency of 5,6 GHz in microstrip form using *RO4350B* [8] as substrate, which is used as standard at *HAW Hamburg*. The given conditions are displayed in table 1.1 and comprise inter alia the substrates parameters. The square phased array must consist of 9 elements to keep the effort moderate. A phase shifter must be developed to enable scanning and, furthermore, a feed network must be developed to drive the demonstrator. The system must be simulated using *CST Studio Suite* and A*WR Design Environment*. The designed components have to be fabricated and measured.

Resonant frequency f	5,6 GHz
Antenna type	Microstrip antenna
Substrate	R04350B
Thickness h of substrate	0,76 mm
Relative dielectric constant ε_r of substrate	3,66
Metallisation thickness t	0,017 mm
Loss tangent δ_{eff} of substrate	0,005
Number of antenna elements	9
Excitation mode of the antenna	TM_{10}
Reference impedance Z_0	50 Ω

Table 1.1: Predetermined parameters for the phased array antenna demonstrator

The demonstrator can be accessed at HAW Hamburg. Contact person is the supervising examiner Prof. Dr.-Ing. Ralf Wendel.

1.2 Structure of the thesis

The phased array antenna demonstrator can be divided into three main components, which are displayed in figure 1.1.

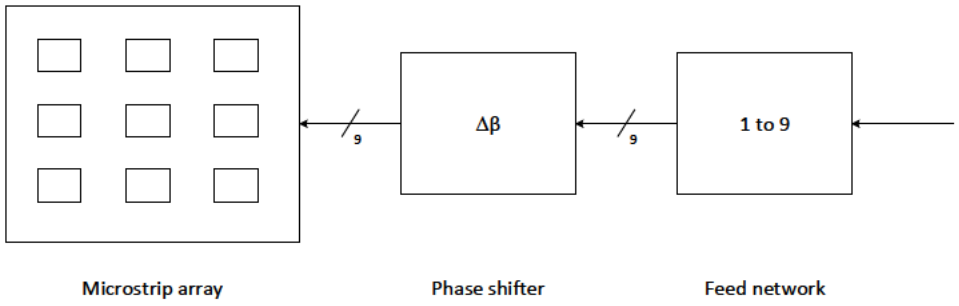

Figure 1.1: Draft of the phased array antenna demonstrator

Furthermore, every main component can be divided into subcomponents. The 3x3 microstrip array consists of the assembly of linear three-element arrays, where one linear array consists of three microstrip antennas. The phase shifter consists of a quadrature hybrid and a reactive load. The phase shifter has the ability to change a signals phase β. The subcomponent of the feed network is a Wilkinson power divider.

Every chapter of this thesis covers the mentioned subcomponents. Firstly, the theoretical basics are introduced. Then the technical requirements of the components are described to create a basis for an evaluation. Afterwards, the design procedure including calculations and simulations is explained. Finally, the measured components are analyzed and evaluated according to the requirements. For the measurements of the demonstrator the components are finally combined. The assembly of the phase shifter and the feed network is here termed feed network module.

Simulations regarding the antennas are performed using *CST*, which is a 3D electromagnetic field solving software. Transmission circuit analysis is performed using *AWR*, which is a software based on equivalent circuit analysis. A data medium, that can be viewed by the supervising examiner, is attached to this thesis. The medium contains all simulation files as well as all measurement files. A structure of the data medium is shown in appendix A.

2 Theoretical principles

In this chapter fundamental concepts of the work are explained. Regarding the design, elementary relations are shown with the help of approximations. The phased array antenna demonstrator is explained by breaking the demonstrator down into its main components. Furthermore, the planar array is analyzed by introducing the microstrip antenna and the linear array.

2.1 Phase shifter

A phase shifter is a circuit with the ability to change a signals phase. Common phase shifters can be classified into digital or analog as well as continuous or successive. In order to not exceed the framework only an analog reflection phase shifter, consisting of a quadrature hybrid terminated by a reactive load, is described. It permits planar circuitry and is easy to fabricate.

In section 2.4.1 it is shown that the beam of an array can be scanned continuously by shifting the phase of individual elements. The phase shift of an element can be controlled by adjusting the reactive load of the hybrid. Therefore, the phase shifter is an elementary component of the demonstrator.

2.1.1 Quadrature hybrid

The quadrature hybrid is a four-port network. Regarding port 1 as the input, port 4 is isolated and the power is equally split between its output ports 2 and 3 [14, p. 343-347]. Between the output ports is a 90° phase shift. The geometry of a quadrature hybrid is shown in figure 2.1.

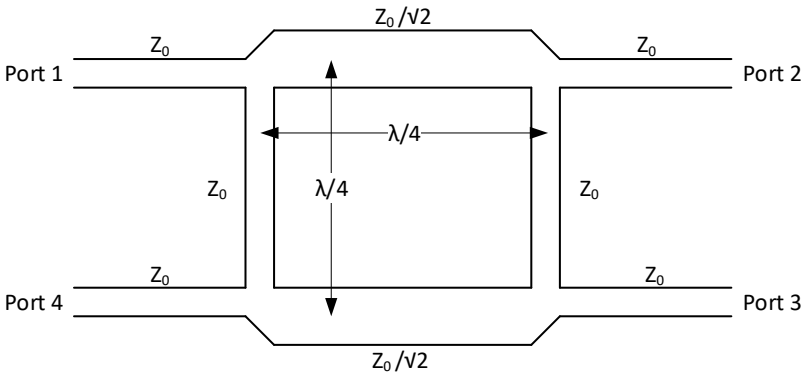

Figure 2.1: Geometry of a quadrature hybrid, following [14, p. 343]

The vertical arms have an impedance of Z_0, whereas the inner horizontal arms have an impedance of $Z_0/\sqrt{2}$. The length of all lines equals quarter-wavelength. The scattering matrix can be determined by even-odd mode analysis and has the form [14, p. 343]

$$[\mathbf{S}] = \frac{-1}{\sqrt{2}} \begin{bmatrix} 0 & j & 1 & 0 \\ j & 0 & 0 & 1 \\ 1 & 0 & 0 & j \\ 0 & 1 & j & 0 \end{bmatrix}. \tag{2.1}$$

From the scattering matrix it is apparent that the output ports 2 and 3 have half of the input power with a phase shift of $-90°$ respectively $-180°$ to port 1. The four-port network can be described by the relation

$$[\mathbf{b}] = [\mathbf{S}][\mathbf{a}], \tag{2.2}$$

where $\underline{a}_i$ is an incident power wave and $\underline{b}_i$ is a reflected power wave.

Assuming port 2 and 3 are terminated with an impedance $\underline{Z}_L$ the reflection coefficient can be expressed as

$$\underline{r}_L = \frac{\underline{a}_i}{\underline{b}_i} = \frac{\underline{Z}_L - Z_0}{\underline{Z}_L + Z_0}. \tag{2.3}$$

Hence, using equations 2.2 and 2.3 the reflected power wave of port 2 can be written as

$$\underline{b}_2 = \frac{\underline{a}_2}{\underline{r}_L} = -j\frac{1}{\sqrt{2}}\,\underline{a}_1 - \frac{1}{\sqrt{2}}\,\underline{a}_4 \tag{2.4}$$

and the reflected power wave of port 3 can be written as

$$\underline{b}_3 = \frac{\underline{a}_3}{\underline{r}_L} = -\frac{1}{\sqrt{2}}\,\underline{a}_1 - j\frac{1}{\sqrt{2}}\,\underline{a}_4. \tag{2.5}$$

Solving equation 2.4 for $\underline{a}_2$ yields

$$\underline{a}_2 = -j\frac{\underline{r}_L}{\sqrt{2}}\,\underline{a}_1 - \frac{\underline{r}_L}{\sqrt{2}}\,\underline{a}_4 \tag{2.6}$$

and solving 2.5 for $\underline{a}_3$ yields

$$\underline{a}_3 = -\frac{\underline{r}_L}{\sqrt{2}}\,\underline{a}_1 - j\frac{\underline{r}_L}{\sqrt{2}}\,\underline{a}_4. \tag{2.7}$$

In accordance with equation 2.2 the reflected power of port 1 can be expressed as

$$\underline{b}_1 = -j\frac{1}{\sqrt{2}}\,\underline{a}_2 - \frac{1}{\sqrt{2}}\,\underline{a}_3 \tag{2.8}$$

and the reflected power of port 4 can be expressed as

$$\underline{b}_4 = -\frac{1}{\sqrt{2}}\,\underline{a}_2 - j\frac{1}{\sqrt{2}}\,\underline{a}_3. \tag{2.9}$$

Substituting equations 2.4 and 2.5 in equation 2.8 yields

$$\underline{b}_1 = j\underline{r}_L\,\underline{a}_4 \tag{2.10}$$

and substituting in equation 2.9 yields

$$\underline{b}_4 = j\underline{r}_L\,\underline{a}_1. \tag{2.11}$$

Thus, regarding the circuit as a two-port network its scattering matrix can be written as

$$[\mathbf{S}_2] = \begin{bmatrix} 0 & j\underline{r}_L \\ j\underline{r}_L & 0 \end{bmatrix}. \tag{2.12}$$

From the two-port scattering matrix it is apparent that no power is reflected. Furthermore, the transmitted power undergoes a 180° phase shift, effected by the geometry of the hybrid, plus a phase shift effected by the load $\underline{Z}_L$. The transmitted power is attenuated by the factor $|\underline{r}_L|$.

2.1.2 Varactor diode

Varactor diodes possess an intrinsic layer with adjustable size and doping profile. When reverse biasing the varactor diode a desired junction capacitance can be adjusted. Therefore, the diode can be used as electronically adjustable reactive load. In figure 2.2 a schematic of the real diode, including its parasitic characteristics, is shown.

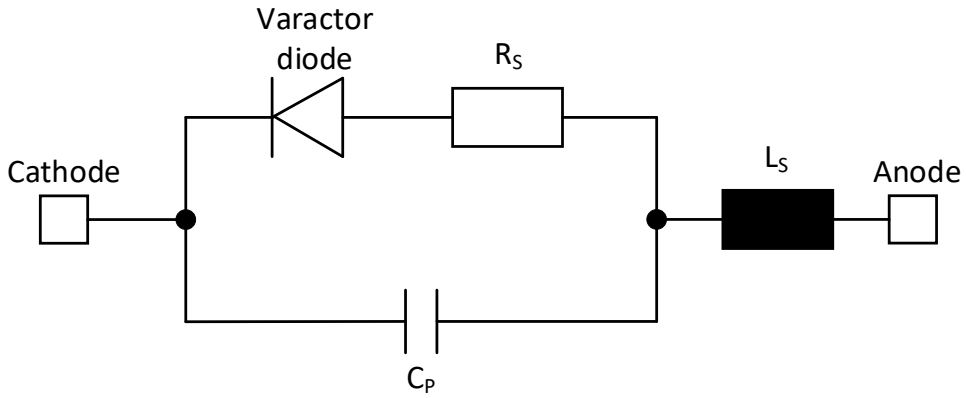

Figure 2.2: Schematic of a real varactor diode, following [9, p. 6]

The parasitic elements due to the package of the varactor diodes have to be taken into account in the design. Manufacturers often provide *SPICE* models, that include the parasitic elements, for simulation purpose.

2.2 Wilkinson power divider

From figure 1.1 one can see that the feed network of the demonstrator must have one input port and nine output ports. Power dividers enable power division from one port to two or more output ports.

The Wilkinson power divider enables power division with adjustable ratio. It can be matched at all ports and its output ports are isolated. The divider can be easily realized in microstrip line form. In figure 2.3 a two-way Wilkinson power divider is shown.

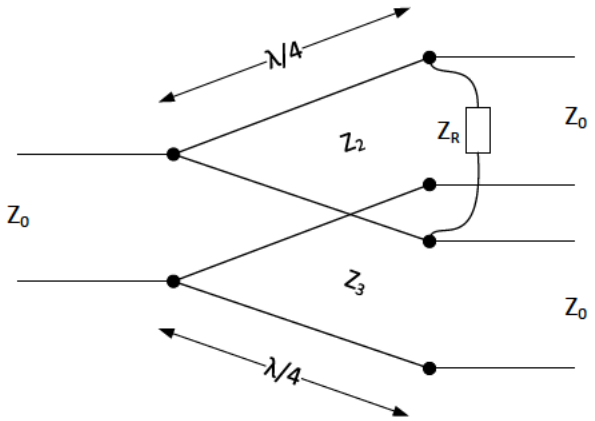

Figure 2.3: Transmission line circuit of an equal splitting Wilkinson power divider, following [14, p. 328]

The input and output microstrip lines have the characteristic impedance Z_0 and the quarter-wavelength lines have the impedances Z_2 and Z_3. The shunt resistor at the end of the quarter-wavelength lines is of value Z_R. The power ratio $k^2 = P_3/P_2$ between the output ports can be adjusted by Z_2, Z_3 and Z_R.

The value of the shunt resistor Z_R is given by [14, p. 332]

$$Z_R = Z_0\left(k + \frac{1}{k}\right) \tag{2.13}$$

and for the impedances of the quarter-wavelength lines the following equations apply

$$Z_2 = Z_0 \sqrt{\frac{1+k^2}{k^3}} \tag{2.14}$$

and

$$Z_3 = Z_0 \sqrt{k(1+k^2)}. \tag{2.15}$$

A N-way power divider, with $N \in \mathbb{N}^*$, can be realized with a cascade of Wilkinson power dividers.

The characteristic impedance of a microstrip line can be adjusted by its width w. For microstrip lines with $w/h \geq 1$, the impedance is given by [14, p. 148]

$$Z = \frac{120\pi}{\sqrt{\varepsilon_e} \cdot \left(w/h + 1,393 + 0,667 \cdot ln(w/h + 1,444)\right)}. \tag{2.16}$$

In a practical design the quarter-wavelength lines of the quadrature hybrid and the Wilkinson power divider are approximately shortened by the factor $1/\sqrt{\varepsilon_e}$ and equal one quarter-wavelength in the substrate. The wavelength in the substrate is referred to as λ_d.

The relative dielectric constant ε_r does not take into account that a fraction of the microstrip field lines is in the air above the substrate. Therefore, an effective dielectric constant ε_e is given, which describes a homogeneous medium replacing the air and the dielectric of the microstrip line. It is approximately given by [14, p. 148]

$$\varepsilon_e = \frac{\varepsilon_r + 1}{2} + \frac{\varepsilon_r - 1}{2} \cdot \frac{1}{\sqrt{1 + 12\, h/w}}. \tag{2.17}$$

2.3 Microstrip antenna

A microstrip antenna, which is often referred to as patch antenna, is a thin conductor of arbitrary shape printed on a grounded dielectric substrate. The dielectric substrate has the thickness h and the relative permittivity ε_r. Most common antenna shapes are rectangular and circular. In figure 2.4 a rectangular patch of length L and width W is shown. The metallic patch as well as the metallic ground are of thickness t, which is usually a few microns.

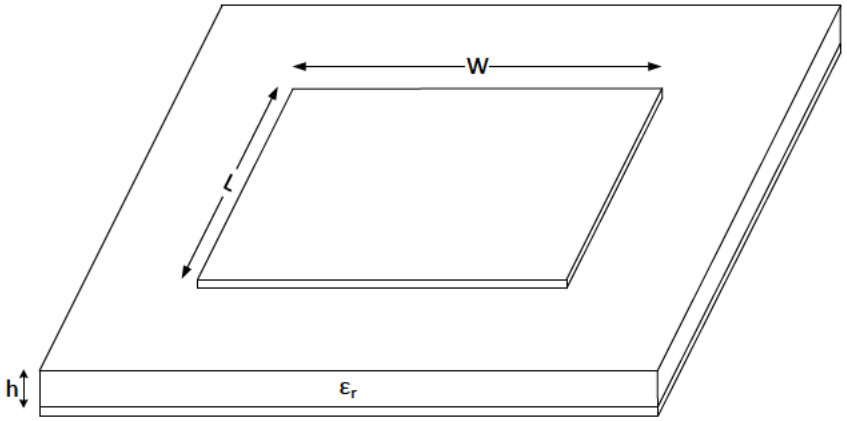

Figure 2.4: Geometry of a rectangular microstrip antenna

There are several analytical methods to analyse microstrip antennas. The most precise results are delivered by full wave methods, solving Maxwell's equations. These challenging methods are complex and, therefore, often solved by powerful software tools like CST. In the following subsections the most important figures of merit are described and useful design guidelines are explained. Appropriate full wave formulas as well as further references can be taken from the specialist literature [2].

The microstrip antenna is ideally treated as an open-circuited transmission line [1, p. 798-801]. Hence, the current at the beginning and the end of the patch is zero, whereas the current is maximum in the center of the patch. In accordance with the viewed open-circuited transmission line, the voltage is maximum at the beginning and the end and minimum in the center. The voltage distribution on the patch effects fringing E-fields at the edges of the patch. Thus, the patch radiates due to the fringing fields. Assuming the patch edges of width W as radiating slots, separated by the distance L, the electrical

length of the patch is wider than its physical length due to fringing. The extension of the length is approximately given by [1, p. 790]

$$\Delta L = 0,412h \frac{(\varepsilon_e + 0,3)\left(\frac{W}{h} + 0,264\right)}{(\varepsilon_e - 0,258)\left(\frac{W}{h} + 0,8\right)}. \tag{2.18}$$

Both slots radiate a field normal to the microstrip antenna, which add in phase. Therefore, maximum radiation in this direction is obtained. For TM_{10} mode the resonant frequency of the microstrip antenna is approximately given by [1, p. 790]

$$f_0 = \frac{c_0}{2L_e\sqrt{\varepsilon_e}}, \tag{2.19}$$

where the effective length L_e equals $L + 2\Delta L$. From equation 2.19 one can see that the length equals approximately one-half wavelength in the substrate to excite the TM_{10} mode.

2.3.1 Antenna feed

An essential aspect in microstrip antenna design is the antenna feed, which can be classified into contacting or noncontacting. Microstrip feed lines on the same substrate as the patch, referred to as coplanar, and feed probes belong to the contacting methods. A feed probe is a coaxial feed line through the bottom of the ground plane and substrate, which is attached to the bottom side of the patch. On the other hand proximity coupling and aperture coupling belong to the noncontacting methods. A noncontacting feed eliminates the need of connectors. Proximity coupled antennas consist of a two-layer substrate, where two substrates are bonded. The patch is placed on the top substrate, whereas an open stub microstrip line below the patch is on the bottom substrate coupling the patch. Aperture coupled antennas consist of two-layer substrate as well. Both layers are separated by a ground plane, which has a small aperture. Through the aperture a microstrip line couples to the patch [13, p. 81-83].

In figure 2.5 the geometry of contacting feeds is shown. Typically, the feed is placed in the center of one radiating edge W to excite the TM_{10} mode [16, p. 1180].

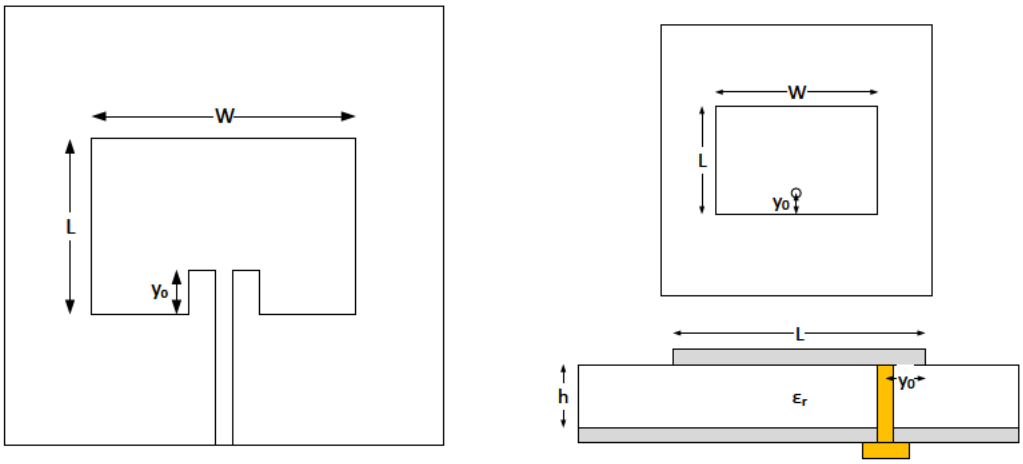

(a) Microstrip antenna with microstrip line feed (b) Microstrip antenna with feed probe

Figure 2.5: Geometry of contacting feeds, following [1, p. 786]

The geometry of noncontacting feeds is shown in figure 2.6. Proximity-coupled microstrip antennas may be append with an open-circuit stub to enhance the bandwidth. Substrates of different thickness and dielectric constant may be used for the radiating element and the feed.

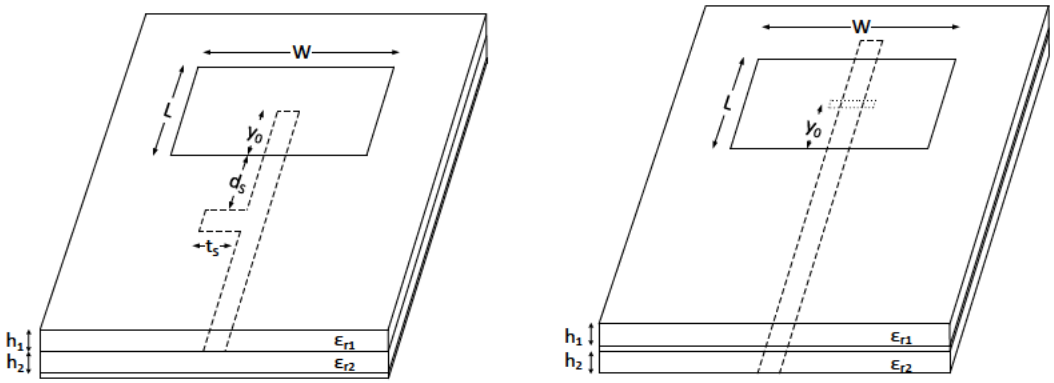

(a) Proximity-coupled microstrip antenna, following [15, p. 368] (b) Aperture-coupled microstrip antenna, following [1, p. 786]

Figure 2.6: Geometry of noncontacting feeds

As one can see from figure 2.5 and 2.6 the methods provide different design parameters, which comprise especially the offset in the feed position. These parameters are used to match the microstrip antenna to 50 Ω and are briefly explained in the next section.

2.3.2 Input impedance

It is crucial to match the antenna for good performance. Matching the antenna can be realized by the feeding technique or further by a matching network, which can be placed coplanar or below the microstrip antenna. Every feeding technique possesses its own methods to match the antenna. Especially the input impedance and, therefore, the bandwidth limits the performance of microstrip antennas. Regarding the Smith chart, narrow matched input impedance loci shall be achieved in the design.

To match the antenna the coplanar feed can be notched. In this manner an inset feed point of length y_0 is realized. At resonance the inset feed point causes a decrease of the input impedance. The coaxial feed can be shifted toward the center of the patch to match the antenna as well [2, p. 12-13]. The decrease of the input impedance in both cases can be explained with the voltage and current distribution according with the open-circuited transmission line model mentioned in section 2.3. The input impedance is maximum when the feed point is located at a radiating edge ($y_0 = 0$ or $y_0 = L$) as the voltage is maximum and the current is minimum. By insetting the feed point the input impedance can be reduced. A feed point in the center of the patch ($y_0 = L/2$) causes an input impedance of zero as the voltage is zero and the current is maximum [13, p. 81]. The resonant frequency is independent of the inset y_0.

Proximity-coupled microstrip antennas can be matched by appropriate insetting the feeding microstrip line and appending a short open-circuit stub of length t_s in a distance d_s to the patch edge. To prevent radiation from the tuning stub it should be devised short [15]. The microstrip line coupling through an aperture can be inset as well to match the antenna. Furthermore, the size of the aperture is chosen small [12].

The gain of the antenna, which is closely related to the directivity, is a figure of merit, that takes into account the efficiency of the antenna. The gain describes the ratio of the radiated intensity to the isotropically radiated intensity with same power input. Following definitions are taken from [1, p. 60-63]. The maximum realized gain can be expressed

by

$$G_{re0} = e_o \cdot D_0, \tag{2.20}$$

where D_0 is the directivity (see section 2.3.4) and e_0 is the overall antenna efficiency. The antenna efficiency depends on the reflection efficiency e_r, the conduction efficiency e_c and the dielectric efficiency e_d. The total efficiency is given by

$$e_0 = e_r e_c e_d, \tag{2.21}$$

where e_r equals $(1 - |\Gamma|^2)$. The reflection coefficient of the antenna is termed Γ. Thus, the input impedance inter alia affects the realized gain of the antenna.

2.3.3 Radiation pattern

Typically, the microstrip antennas radiation characteristic is described with the E- and H-plane. The geometry of a microstrip antenna for far-field observation is shown in figure 2.7. The E-plane cuts the far-field radiation pattern at $\phi = 0°$ and the H-plane at $\phi = 90°$.

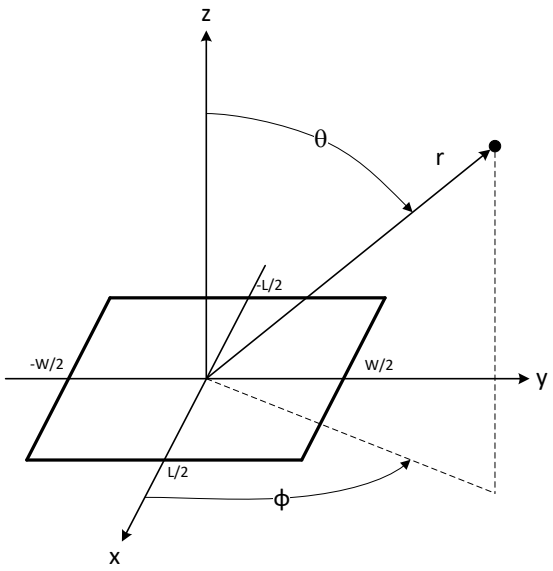

Figure 2.7: Geometry of the rectangular microstrip antenna for E- and H-plane, following [2, p. 10]

Assuming the radiating slots as equivalent electric current sources, the radiation pattern in the E-plane can be described by

$$E_E = -j\,\frac{V_0\,k_0\,W\,e^{-jk_0r}}{\pi r}\cdot cos\left(\frac{k_0 L_e}{2}sin(\theta)\right) \tag{2.22}$$

and the H-plane can be expressed as

$$E_H = -j\,\frac{V_0\,k_0\,W\,e^{-jk_0r}}{\pi r}\cdot cos(\theta)\frac{sin\left(\frac{k_0 W}{2}sin(\phi)\right)}{\frac{k_0 W}{2}sin(\phi)}, \tag{2.23}$$

where V_0 is the slot voltage across either radiating edge and k_0 is the propagation constant in free-space. The equations are taken from [2, p. 9]. The normalized patterns of a rectangular microstrip antenna are displayed in figure 2.8.

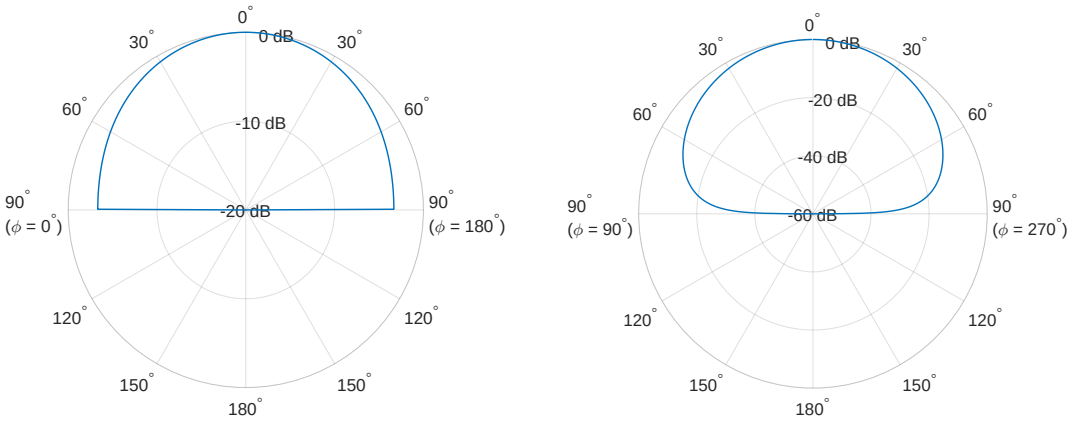

(a) E-plane (b) H-plane

Figure 2.8: Normalized patterns of a rectangular microstrip antenna ($L = \lambda_d/2$, $W = \lambda_0/2$, $\varepsilon_r = 3.66$)

Only the upper hemisphere is shown to account for the ground plane. Indeed, there is marginal radiation for $\theta > 90°$ and the patterns are not symmetrical. Antennas with maximum radiation toward $\theta_0 = 0°$ are termed broadside antennas.

2.3.4 Directivity

The directivity of an antenna is a measure for the concentration of its radiation intensity compared to that of an isotropic source. The ratio of its radiation intensity over that of an isotropic source is referred to as directivity. It is specified for the direction of the main beam [1, p. 41]. The directivity of a microstrip antenna excited in TM_{10} mode can be approximately written as [3, p. 848]

$$D_0 = \frac{2}{15\,G_{rad}} \left(\frac{W}{\lambda_0}\right)^2 \cdot \left(\frac{sin(k_d\,h)}{k_d\,h}\right)^2, \tag{2.24}$$

where G_{rad} is the radiation conductance and k_d is the propagation constant in the substrate. The radiation conductance describes the power dissipated by the antenna. It is dependent on the substrate and the length L of the antenna. Equation 2.24 states that the width W is the most contributing factor for high directivity in microstrip antenna design. However, to excite the TM_{10} the width must not be greater than one-half wavelength.

2.3.5 Bandwidth

The bandwidth is classified into impedance bandwidth and bandwidth regarding the radiation pattern. Microstrip antennas usually have a narrow impedance bandwidth of 2 % to 5 %. The pattern bandwidth indicates the radiation including directivity and gain. Usually it is about 10 % to 20 % [13, p. 83-84]. Thus, the impedance bandwidth limits the application of microstrip antennas. The impedance bandwidth is defined for $VSWR \leq 2$, $|\Gamma| \leq 1/3$ [1, p. 825].

The input impedance of a microstrip antenna behaves as a resonant circuit. Assuming the antenna is perfectly matched at its resonant frequency and $VSWR$ at the lower band edge frequency equals $VSWR$ at the upper band edge frequency, the impedance bandwidth can by expressed by [17, p. 1346]

$$B = \frac{1}{Q}\frac{VSWR - 1}{\sqrt{VSWR}}, \tag{2.25}$$

where Q is the antennas quality factor. The increase of the impedance bandwidth is an essential requirement in antenna design and is discussed in a plethora of papers [12], [15]

and [17].

The impedance bandwidth is limited by the thickness and dielectric constant of the substrate as well as radiation from the feed network and matching. Thin substrates have a high quality factor. Therefore, the bandwidth can be theoretically increased by increasing the substrates thickness. However, a thicker substrate causes disturbance in the radiation pattern due to increased excitation of surface waves [13, p. 83], [17, p. 1345-1346].

Best results are obtained by designing broad-band impedance matching networks or by proximity and aperture coupled antennas. A further method to increase the bandwidth is to use stacked patches, which consist of a parasitic and a fed patch on a multi-layer substrate. Hence, the increase of impedance bandwidth is achieved with complex fabrication. Impedance bandwidths up to 20 % can be achieved with these methods [13, p. 83].

2.3.6 Sidelobe level

Sidelobe levels are classified into relative and absolute. The highest sidelobe level relative to the main beam is referred to as relative sidelobe level, whereas the absolute sidelobe level is referred to as relative to isotropic.

The sidelobe level of a microstrip antenna is affected by surface waves and especially by narrow bandwidth and radiation from the feed network. As square patches may excite higher order modes due to a misplaced feed position, cross polarization can be caused. The radiation pattern of some higher order modes have a null at broadside and maxima off broadside and, therefore, would degrade the desired radiation. To avoid cross polarization a rectangular patch should be designed for lower sidelobe levels [16, p. 1180].

2.4 Linear array

The assembly of N antennas in one direction is called linear array. As the fields of the individual elements interfere, the linear array can scan the main beam along its orientation. The directivity of the array can be increased due to the constructively interference in the desired direction. In the following the individual elements are identical. The spacing between the center of the elements is referred to as distance d. In figure 2.9 a three-element array of isotropic sources with spacing d is shown.

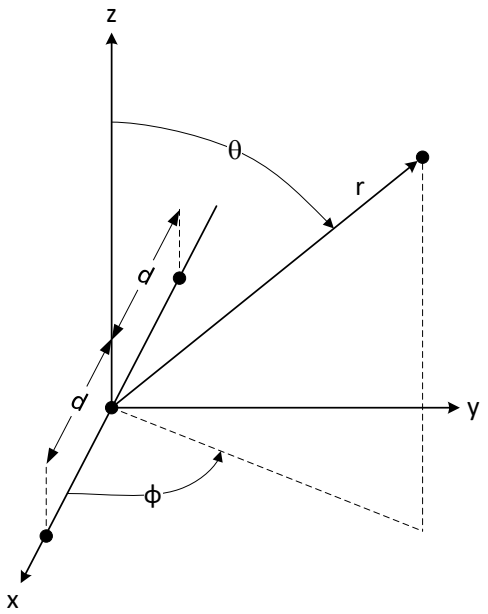

Figure 2.9: Linear three-element array of isotropic sources along the x-axis, following [1, p. 320]

Assuming far-field observation, the elevation angles θ_n as well as the azimuth angles ϕ_n between the individual elements and a point in the far-field are identical. The same applies for the distance r_n of each single element to the point in the far-field.

To determine the impedance bandwidth as well as the input impedance of the linear array a single element is considered. The pattern bandwidth is considered by the overall array. The same applies for the planar array.

2.4.1 Array factor

To determine the characteristic of a linear array, the array factor, which is a function of the geometry and excitation, is introduced in the following. Assuming no coupling between elements, the array factor of a linear array of N isotropic elements is given by [1, p. 319]

$$AF = \sum_{n=1}^{N} a_n e^{j(n-1)\Psi}, \tag{2.26}$$

where Ψ equals

$$\Psi = k_0\, d\, sin(\theta) cos(\phi) + \beta. \tag{2.27}$$

The factor Ψ takes account of the different distances of the elements to the point in the far-field. The difference in phase excitation between adjacent elements is indicated by β and the factor a_n is the magnitude excitation of each element. Assuming a uniform array, which consists of identical elements, all elements have an identical magnitude with a progressive phase shift. The following relations are taken from [1, p. 294]. With Euler´s formula the expression of 2.26 can be written as

$$AF = e^{j((N-1)/2)\Psi} \cdot \left[\frac{sin\left(\frac{N\Psi}{2}\right)}{sin\left(\frac{\Psi}{2}\right)} \right]. \tag{2.28}$$

For a normalized array factor with a reference point in the physical center of the array the expression of 2.28 reduces to

$$(AF)_n = \frac{1}{N} \cdot \left[\frac{sin\left(\frac{N\Psi}{2}\right)}{sin\left(\frac{\Psi}{2}\right)} \right]. \tag{2.29}$$

Equation 2.29 has its maximum when the expression in brackets reduces to the form $sin(0)/0$. Therefore, the formula

$$\frac{\Psi}{2} = \frac{1}{2}(k_0\, d\, sin(\theta)cos(\phi) + \beta) = m\pi \tag{2.30}$$

with $m \in \mathbb{Z}$ must be fulfilled. Referring to figure 2.9 the linear array can scan along the x-axis. Hence, the beam can be directed to $\phi = 0°$ or $\phi = 180°$, while θ can be directed between $0°$ and $90°$ from broadside. The major lobe of an array occurs at the maximum of the array factor. Equation 2.29 attains its first maximum when $\Psi = 0$ as it reduces to a $\sin(0)/0$ form. Therefore, equation 2.30 can be written as

$$\Psi = k_0\, d\, sin(\theta)cos(\phi) + \beta = 0. \tag{2.31}$$

For a broadside array with $\theta_0 = 0°$ equation 2.31 yields

$$\Psi = k_0\, d\, sin(\theta)cos(\phi) + \beta|_{\theta_0=0°} = \beta = 0. \tag{2.32}$$

Hence, to design a broadside array the spacing d between the elements can consequently be of any value. Moreover, the angle θ can be adjusted using

$$\beta = \pm k_0\, d\, sin(\theta). \tag{2.33}$$

The sign in equation 2.33 results from the $cos(\phi)$ expression and indicates the beam direction relative to the x-axis.

In figure 2.10 the normalized array factor in accordance with equation 2.29 is displayed for a linear three-element array with spacing $\lambda_0/2$. The figure shows the array factor pattern for $\theta_0 = 0°$ and $\theta_0 = 30°$.

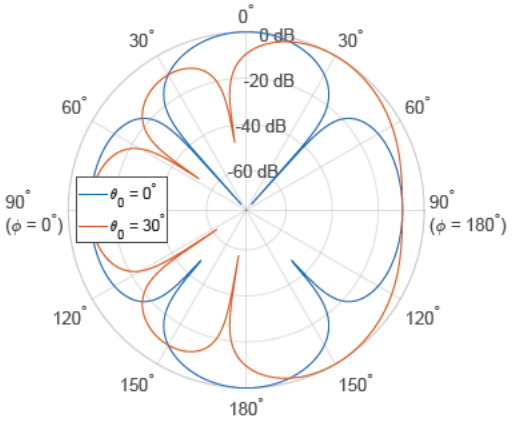

Figure 2.10: Pattern of the normalized array factor for $\theta_0 = 0°$ and $\theta_0 = 30°$ ($N = 3$, $d = \lambda_0/2$, $\beta_{0°} = 0°$, $\beta_{30°} = 90°$)

The total far-field of a linear N-element array can be calculated by the pattern multiplication rule. This rule states, that the total far-field equals the product of the array factor of isotropic sources and the radiation pattern of an individual antenna element [1, p. 287]. The pattern of a uniform linear array with $\beta = 0°$ is similar to the pattern of the individual antenna. By applying a phase shift the pattern can be scanned in θ. Figure 2.10 is an example for a scan toward $\theta = 30°$. In array design the appearance of sidelobes has to be taken into consideration.

2.4.2 Directivity

The directivity of a linear array equals the product of the directivity of a single element and the directivity of the array factor and is approximately given by [1, p. 813]

$$D_A = D_0 \cdot D_{AF}. \tag{2.34}$$

For large arrays, where the overall length is significantly greater than the spacing, the directivity of a broadside array factor can be approximately expressed as [1, p. 315]

$$D_{AF} = 2N\frac{d}{\lambda_0}. \tag{2.35}$$

For this thesis equation 2.34 is inaccurate as the linear array is small in size. More precise calculations ca be taken from [1]. Nevertheless, an elementary conclusion from equation 2.35 is that the directivity increases with the number of elements N and the spacing. Thus, the limiting factor concerning directivity is the overall array size. Regarding the spacing between adjacent elements antenna design is inter alia a trade-off between directivity and sidelobe level.

2.4.3 Sidelobe level

Especially in array applications the sidelobe level of antennas becomes highly important. The sidelobe level is dependent on the spacing between the elements and, hence, in design one can influence the sidelobe level. For a spacing $d \geq m\lambda_0$ with $m \in \mathbb{N}^*$ there occur more than one principle maxima.

Typical error sources causing higher sidelobe levels are phase and amplitude errors. The feed network and especially the phase shifter cause deviations in amplitude and phase. Therefore, the antenna elements are excited with variation in amplitude and phase. Assuming Gaussian distributed excitation errors an increase in the standard deviation effects an increase of the sidelobe levels [16, p. 1177].

Another effect, that causes amplitude and phase errors, are variations in the elements due to fabricational tolerances. Assuming there are variations in length, width and the feed point the single antenna elements exhibit variations in resonant frequency and input impedance. Therefore, the magnitudes and phases of the fields radiated by the elements will be in error. In [16, p. 1178] it is shown that a 1 % shift in resonant frequency causes a 12,5 ° change in the radiated field. After equation 2.19 the resonant frequency is proportional to the length of the patch. Inaccuracies in the length effect a change in resonant frequency, which is given by

$$\Delta f_0 = \frac{-\Delta L}{L} f_0. \tag{2.36}$$

Furthermore, the resonant frequency varies as $1/\sqrt{\varepsilon_r}$. This effects a change in resonant frequency by

$$\Delta f_0 = \frac{-\Delta \varepsilon_r}{2\varepsilon_r} f_0. \tag{2.37}$$

When microstrip antennas are closely spaced next to each other mutual coupling is caused by surface waves. Therefore, the amplitude and phase of the excitation on an antenna element is not proportional to the amplitude and phase of the radiated field. In this way the radiation pattern of the array is perturbed and sidelobe levels increase. However, the effect of mutual coupling can be neglected for uniform arrays with spacing of $\lambda_0/2$. Considerable errors occur when arrays with greater spacing are scanned off broadside [16, p. 1179].

The important aspect from this section is that the spacing in the array and fabricational errors influence the sidelobe level. The elementary errors limiting the sidelobe levels are described, more details can be obtained from [18]. The described relations apply for the planar array as well.

2.5 Planar array

A planar antenna is formed by placing microstrip antennas along a grid. The planar antenna enables to scan the main beam to any point in the hemisphere. In figure 2.11 a planar array of isotropic sources is displayed.

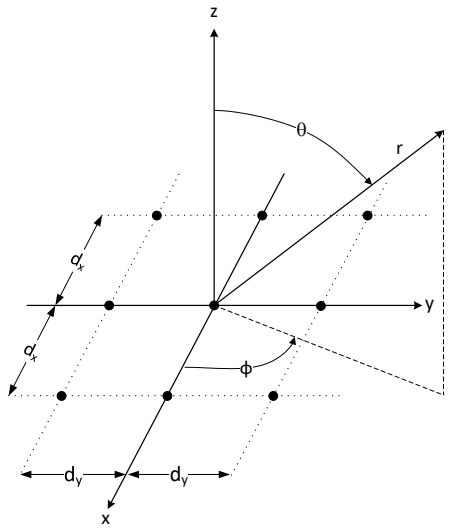

Figure 2.11: Planar 3x3 element array of isotropic sources in the x-y plane, following [1, p. 350]

The planar array consists of N M-element linear arrays placed next to each other. The dots in the figure represent an antenna element, respectively. The distance between two adjacent elements in x-direction is referred to as d_x and in y-direction as d_y. The phase shift between two adjacent elements in x-direction is represented by β_x and in y-direction by β_y [1, p. 348-354].

2.5.1 Array factor

Referring to section 2.4.1 and to [1, p. 348], the array factor of a M-element linear array along the x-direction is given by

$$S_{xm} = \sum_{m=1}^{M} a_m e^{j(m-1)(k_0\, d_x\, sin(\theta)cos(\phi)+\beta_x)}, \tag{2.38}$$

where adjacent elements are separated by the distance d_x and excited with a progressive phase shift β_x. The array factor of a N-element linear array along the y-direction is given by

$$S_{yn} = \sum_{n=1}^{N} a_n e^{j(n-1)(k_0\, d_y\, sin(\theta)sin(\phi)+\beta_y)}, \tag{2.39}$$

where adjacent elements are separated by the distance d_y and excited with a progressive phase shift β_y, respectively. The array factor of the planar array is the product of the linear array factors and can be expressed as

$$AF = S_{yn}\, S_{xm} = \sum_{n=1}^{N} \left[\sum_{m=1}^{M} a_m e^{j(m-1)(k\, d_x\, sin(\theta)cos(\phi)+\beta_x)} \right] a_n e^{j(n-1)(k_0\, d_y\, sin(\theta)sin(\phi)+\beta_y)}. \tag{2.40}$$

Assuming the planar array is uniform and all elements are excited by the amplitude a, equation 2.40 can be written as

$$AF = S_{yn} S_{xm} = a \sum_{m=1}^{M} e^{j(m-1)(k_0\, d_x\, sin(\theta)cos(\phi)+\beta_x)} \sum_{n=1}^{N} e^{j(n-1)(k_0\, d_y\, sin(\theta)sin(\phi)+\beta_y)}. \tag{2.41}$$

The normalized array factor of the form in 2.41 is given by

$$(AF)_n(\theta,\phi) = \left[\frac{1}{M}\cdot\frac{sin\left(\frac{M\Psi_x}{2}\right)}{sin\left(\frac{\Psi_x}{2}\right)}\right]\left[\frac{1}{N}\cdot\frac{sin\left(\frac{N\Psi_y}{2}\right)}{sin\left(\frac{\Psi_y}{2}\right)}\right], \tag{2.42}$$

where Ψ_x equals

$$\Psi_x = k_0\, d_x\, sin(\theta)cos(\phi) + \beta_x \tag{2.43}$$

and Ψ_y equals

$$\Psi_y = k_0\, d_y\, sin(\theta)cos(\phi) + \beta_y. \tag{2.44}$$

Assuming the main beams of both linear arrays are directed toward the same direction along $\theta = \theta_0$ and $\phi = \phi_0$ the progressive phase shift β_x is given by

$$\beta_x = -k_0\, d_x\, sin(\theta_0)cos(\phi_0) \tag{2.45}$$

and the progressive phase shift β_y can be expressed by

$$\beta_y = -k_0\, d_y\, sin(\theta_0)sin(\phi_0). \tag{2.46}$$

Applying the pattern multiplication rule the total far-field equals the product of the individual element and the array factor of the planar array. By applying a phase shift in x-direction and in y-direction the beam can be scanned in the hemisphere.

2.5.2 Directivity

The directivity of a large planar array can approximately be calculated by [1, p. 359]

$$D_A = \pi cos(\theta_0) D_x D_y. \tag{2.47}$$

Referring to section 2.4.2 D_x and D_y are the directivities of large broadside linear arrays in x-direction and y-direction. As the projected area of the planar array decreases the directivity slightly decreases as well. This is taken into account by the factor $cos(\theta_0)$.

3 Requirements analysis

For the performance of the demonstrator it is necessary to develop components with good performance. In this section it is explained which parameters are important for the performance of the components and specific requirements are defined. The design in section 4 as well as the evaluation in section 5 are compared to the defined requirements. Firstly, elementary considerations regarding the choice of components are described. Afterwards, specific requirements are defined, which are oriented towards common datasheets. However, to take account of systematic and random errors individual requirements are specified for this thesis.

The fabrication tolerance regarding microstrip circuits is about $\pm 0{,}2\,\mathrm{mm}$ (R. Herrmann: personal communication, 03.06.2021) and the dielectric constant of the substrate has a tolerance of $\pm 0{,}05$ [8, p. 3]. These deviations must be taken into account in the definition of the requirements.

3.1 Phase shifter

The phase shifter is required to enable beam steering. As digital phase shifters are expensive and require very small microstrip lines, it is decided to develop an analog phase shifter in microstrip form. Most common types in microstrip form are switched-line, loaded-line and reflection phase shifters. For the beam steering a wide relative phase shift is required. As loaded line phase shifters solely enable small phase shifts in the order of $45\,^\circ$, this design does not satisfy the fundamental requirements. On the other hand, switched-line phase shifters enable discrete binary phase shifts. Using multiple stages of the switched-line phase shifter, phase shifts of $\Delta\beta = 180\,^\circ$, $90\,^\circ$, $45\,^\circ$ etc. can be realized. However, this design involves phase errors due to a finite number of switches. Details regarding the design of these types can be taken from [14, p. 534-537].

As described in section 2.1 reflection phase shifters enable a continuous phase shift. For this reason this design is used for the thesis. Usually varactor diodes or PIN diodes are used as load in the design. Here it is decided to use varactor diodes based on earlier experience (R. Wendel: personal communication, 14.04.2021).

Ideally, a phase shifter with a relative phase shift range of 360 ° is required. However, it is possible to enable a range of 360 ° by utilizing coaxial cables of different length and a phase shifter with a relative phase shift of 180 °. Due to the different lengths, the coaxial cable cause different phase shifts. By connecting the appropriate cable to the appropriate phase shifter a range of 360 ° is covered. In this way the requirement is facilitated.

An overview regarding all requirements is listed in table 3.1. The typical values are taken from [5] and solely shall indicate what is possible to achieve.

Parameter	**Frequency**	**Typ.**	**Required**
Bandwidth	-	$> 10\,\%$	$> 5\,\%$
Relative phase shift	5,32 GHz-5,88 GHz	$> 230\,°$	$> 180\,°$
Insertion loss	5,32 GHz-5,88 GHz	$> -4{,}5\,\mathrm{dB}$	$> -5\,\mathrm{dB}$
Return loss (In.)	5,32 GHz-5,88 GHz	$< -20\,\mathrm{dB}$	$< -10\,\mathrm{dB}$
Insertion loss variation	5,32 GHz-5,88 GHz	$< 0{,}6\,\mathrm{dB}$	$< 3\,\mathrm{dB}$

Table 3.1: Required parameters of the phase shifter

The required bandwidth of the phase shifter is set to 5 %. In principle, the bandwidth is limited by the insertion loss variation. In section 4.1.3 it is shown that the variation increases for greater bandwidths. The required insertion loss variation is set to 3 dB. Designs in microstrip form from experienced developers exhibit variations about 0,6 dB. These designs are highly optimized due to different enhancements, that eliminate negative impacts from the diode's parasitic elements [5, p. 1867]. However, there was not enough time to implement such enhancements.

To account for losses of the microstrip lines and attenuation by the varactor diodes, the required maximal insertion loss is set to $-5\,\mathrm{dB}$. The required return loss is set to $-10\,\mathrm{dB}$, which is a realistic value in practical designs.

3.2 Wilkinson power divider

A junction circuit is required to feed the antenna elements. For the antenna application it is crucial to provide balanced phases and magnitudes. Common divider networks in microstrip form are the Wilkinson power divider and a lossy power divider with resistors. As the Wilkinson power divider ideally has no losses, a nine-way equally splitting Wilkinson power divider would satisfy the requirements for the network. However, this divider requires crossover resistors for more than two outputs. Hence, it is difficult to design in planar form [14, p. 332]. The lossy divider, which has internal losses due to resistors, has to be designed symmetrical with identical microstrip line lengths to provide balanced phases and magnitudes. This would require a complex design as the geometry became circular. For this reason a two-way Wilkinson power divider is used in this thesis. To provide a nine-way split, the dividers have to be cascaded. The disadvantage of this circuit is that it cannot be realized with exact nine output ports. The typical values in the tables can be obtained from common vendors of RF components.

3.2.1 Two-way Wilkinson power divider

The two-way Wilkinson power divider is the elementary component of the junction circuit. Therefore, such a divider has to be fabricated for analysis purposes. The requirements of the two-way divider are shown in table 3.2.

Parameter	**Frequency**	**Typ.**	**Required**
Insertion loss	5 GHz-6 GHz	$> -3{,}7\,\mathrm{dB}$	$> -4\,\mathrm{dB}$
Isolation	5 GHz-6 GHz	$< -20\,\mathrm{dB}$	$< -15\,\mathrm{dB}$
Return loss (In.)	5 GHz-6 GHz	$< -15\,\mathrm{dB}$	$< -10\,\mathrm{dB}$
Return loss (Out.)	5 GHz-6 GHz	$< -20\,\mathrm{dB}$	$< -10\,\mathrm{dB}$
Magnitude Balance	5 GHz-6 GHz	$< 0{,}1\,\mathrm{dB}$	$< 0{,}5\,\mathrm{dB}$
Phase Balance	5 GHz-6 GHz	$< 1\,^\circ$	$< 15\,^\circ$

Table 3.2: Required parameters of the two-way Wilkinson power divider

The required insertion loss is set to minimum $-4\,\mathrm{dB}$, which is $1\,\mathrm{dB}$ below the ideal insertion loss. The lossy microstrip line as well as losses effected by the connector and the soldering joint herewith are considered.

As a rule of thumb in practical microwave designs there is satisfaction with $-10\,\mathrm{dB}$

to −15 dB isolation and return loss. Practical experiences during the thesis have shown, that it is easier to obtain isolation below −15 dB than return loss. The return loss is more dependent on the center frequency. As the difficulty in design is to meet quarter-wavelength for the junction circuit, the required return loss is 5 dB above the required isolation.

The symmetry of the circuit is evaluated regarding the magnitude and phase balance of the insertion loss. In worst case the output lines deviate 0,4 mm in length due to fabrication. Such a difference in length causes a phase shift of approximately

$$\beta = -2\, k_d\, l = -2\, \frac{360^\circ}{\lambda_d}\, 0,4\,\text{mm} = -10,29^\circ. \tag{3.1}$$

Furthermore, the required phase balance is set to 15 ° to account for non identical SMA connectors and soldering joints. The same applies for the magnitude balance, which is set to 0,5 dB.

3.2.2 16-way Wilkinson power divider

The 16-way divider consists of 15 two-way dividers in total, which are placed in four stages. Hence, the ideal insertion loss of each output port equals −12 dB. Regarding the overall performance of the divider, there occur difficulties due to the size of the circuit board, which equals approximately 20 cm x 15 cm. Connecting cables to the SMA connectors causes the board, which is rigid, to bend. In this way a surface tension works destructively on the soldering joints and may affect the measurements. This circumstance has to be considered in the definition of the requirements. The requirements to be met are listed in table 3.3.

Parameter	**Frequency**	**Typ.**	**Required**
Insertion loss	5 GHz-6 GHz	> -13 dB	> -15 dB
Isolation	5 GHz-6 GHz	< -20 dB	< -20 dB
Return loss (In.)	5 GHz-6 GHz	< -15 dB	< -10 dB
Return loss (Out.)	5 GHz-6 GHz	< -15 dB	< -10 dB
Magnitude Balance	5 GHz-6 GHz	$< 0,5$ dB	$< 1,5$ dB
Phase Balance	5 GHz-6 GHz	$< 8^\circ$	$< 25^\circ$

Table 3.3: Required parameters of the 16-way Wilkinson power divider

The required maximum insertion loss is set to −15 dB, especially to take account of long microstrip lines caused by the geometry of the divider. Accounting the gained experience with the two-way divider, which is a preview to section 5.2.1, the required isolation is set to −20 dB. It is observed that it is realistic to achieve an isolation below −20 dB. Furthermore, non-adjacent outputs should provide significantly better isolation than −20 dB due to the geometry of the divider.

To consider the described problems above, the required return loss is set to −10 dB again. Furthermore, considerations must be made in respect to meet quarter-wavelength. With the increased number of two-way dividers, the absolute probability that dividers suffer in length increases.

The increased length of microstrip lines connecting two dividers causes greater attenuation in relation to the two-way divider. Moreover, the potential damaged soldering joints and the increased number of output ports are respected and the required magnitude and phase balance is slightly increased in relation to the two-way divider. The magnitude balance is set to 1,5 dB and the required phase balance is set to 25 °.

3.3 Feed network module

The merge of phase shifter and power divider here is termed as feed network module. The module must be placed between network analyzer and antenna. Therefore, in the measuring chamber the module has to be attached to the rotating table, where the antenna is placed. Hence, the module must be small in size and lightweight.

As there is no place for a function generator next to the rotating table, the module must be equipped with an internal DC supply. To tune the phases, the phase shifters must be easily accessible to adjust the appropriate control voltage. Furthermore, radiation from the module is undesired and must be minimized to a minimum of −20 dB in relation to the maximum of a reference antenna.

The electrical characteristic of the module is given by the power divider and the single phase shifter. Therefore, no further requirements for the functionality are defined. The requirements of the feed network module are listed in table 3.4.

Parameter	**Required**
Weight	$< 1\,\text{kg}$
Size	$< 30\,\text{cm}$ x $20\,\text{cm}$
DC supply	internal
Radiation	$< -20\,\text{dB}$

Table 3.4: Required parameters of the feed network module

The maximum size of the module is limited by fabrication to approximately 30 cm x 20 cm. The required minimum radiation has to be measured relative to a known horn antenna. The horn antenna is then used to determine the realized gain of the fabricated antennas.

3.4 Microstrip antenna

Firstly, general considerations regarding the feed of the microstrip antenna are explained. Then, functional requirements for the antenna are defined.

3.4.1 Antenna feed

The overall objective of this thesis is to develop a planar antenna array and to steer its beam. Referring to section 2.4 the spacing between the antenna elements is important for good array performance. Furthermore, every antenna element must be excited with an individual phase shift appropriate to the desired scan angle.

Therefore, antennas fed by coplanar microstrip lines cannot be used in this thesis. On the one hand, there is not enough space at the circuit board and, on the other hand, the feed by microstrip lines would cause the phase tuning of the antenna elements to become cumbersome. A single patch antenna fed by a microstrip line is certainly possible. However, the aim of the development of the microstrip antenna is to investigate the feasibility of the feed in regard to the array.

Aperture and proximity coupled antennas provide good bandwidths. Furthermore, radiation from the feed is minimized due to the noncontacting feed. At *HAW Hamburg* the substrate *RO4350B* is available, which consists of one layer substrate surrounded by copper from the top and bottom side. As aperture and proximity coupling are complicate and need a multilayer substrate, these methods are not used in this thesis.

Thus, a microstrip antenna with feed probe must be designed. This feed method can be manufactured at *HAW Hamburg* and has the advantage that it does not affect the spacing between elements.

3.4.2 Patch

The requirements of the microstrip antenna are listed in table 3.5.

Parameter	**Required**
Resonant frequency	5,6 GHz ± 56 MHz
Input impedance @ 5,6 GHz	50 Ω ± (10 + 10i) Ω
Bandwidth	> 2 %
Directivity	> 7 dBi
Realized gain	> 5,5 dBi

Table 3.5: Required parameters of the microstrip antenna

To define the required accuracy in resonant frequency, the fabrication tolerance at *HAW Hamburg* and variations in the substrate have to be considered. Hence, in accordance with equation 2.36 the resonant frequency can change with 8,4 MHz due to the fabrication tolerance. According to equation 2.37, variations in the dielectric constant can cause a change in resonant frequency of about 38,25 MHz. For these reasons and, furthermore, to take inaccuracies in the feed into account the required accuracy in resonant frequency is set to 56 MHz.

Regarding the input impedance, a maximum deviation of ± (10 + 10i) Ω from 50 Ω shall be achieved. The maximum acceptable deviation takes inaccuracies of the geometry and substrate into account. Moreover, the input impedance significantly depends on the inset of the feed as described in section 2.3.2.

Referring to [13, p. 80] one can estimate a bandwidth of about 2 % for a substrate with $\varepsilon_r = 3{,}66$ and $h/\lambda_0 \approx 0{,}014$. In this thesis, the bandwidth is strongly limited by the thin substrate.

In accordance with [1, p. 814] the required directivity of the antenna is set to 7 dBi. Simulations have revealed that the realized gain is approximately 1 dB less than the directivity. However, the realized gain depends on the input impedance. Assuming the input impedance of the fabricated antenna is poorer matched than the simulated antenna, the required realized gain is set to 5,5 dBi.

Due to the limited time of this thesis, no further requirements to figures of merit of the microstrip antenna are defined. A good introduction for further development is provided by [1, p. 783], [13] and [2].

3.5 Linear array

The linear array consists of three microstrip antennas. It is assumed that the array elements behave similar to the previously described antenna. As the design is a trade-off between all figures of merit, the requirements are not defined that strict. The performance of the linear array is in principle limited by the number of elements and the feed network. In this thesis a uniform array is designed. Nonuniform arrays provide better performance regarding sidelobes and pattern. As such arrays require amplifiers, this would complicate the design of the feed network. For this reason, a uniform linear array must be designed.

The required values of the linear three-element array are listed in table 3.6.

Parameter	**Required**
Scan angle θ_0	$> \pm 20\,^\circ$
Relative side lobe level	$< -10\,\mathrm{dB}$
Directivity	$> 11{,}5\,\mathrm{dBi}$
Realized gain	$> 10\,\mathrm{dBi}$
Realized gain variation	$< 1\,\mathrm{dB}$
Mutual coupling	$< -10\,\mathrm{dB}$

Table 3.6: Required parameters of the linear three-element array

The directivity as well as the realized gain of the antenna increase due to the number of elements. Assuming an individual element with a directivity of 7 dBi for this thesis a linear three-element array with at least 11,5 dBi is required. Simulations have revealed that this is a realistic value. The minimum required realized gain is set to 10 dBi to account for losses due to inaccuracies in the fabrication.

Regarding the maximum scan angle one has to consider the low number of elements. The steering of the main beam to wide angles off broadside is not possible as the side lobes significantly increase. For such applications antennas with more elements have to be used. To illustrate the dependence of the array factor on the number of elements, the pattern of the array factor for three and for 16 elements is displayed in figure 3.1 for different scan angles. The elements are spaced with $d = 0,5\lambda_0$.

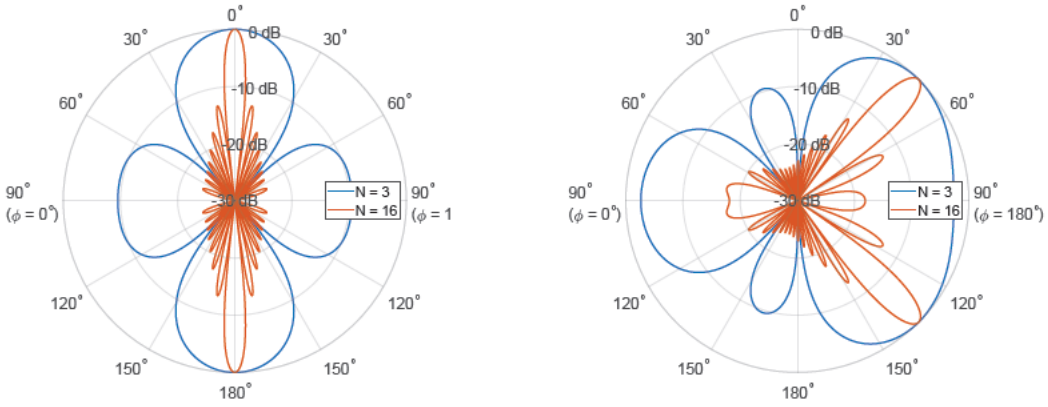

(a) $\theta_0 = 0\,°$ (b) $\theta_0 = 45\,°$

Figure 3.1: Pattern of the normalized array factor for $N = 3$ and $N = 16$ $(d = 0,5\lambda_0)$

From the figures one can see that the main lobes at $\theta_0 = 0\,°$ and $\theta_0 = 45\,°$ are much wider for $N = 3$, respectively. Referring to equation 2.29 the array factor falls faster toward zero for greater N. From figure 3.1b one can see that there is still a great radiation between the desired angle of $\theta_0 = 45\,°$ and broadside for $N = 3$. In detail, the radiation of the three-element array is much greater than the radiation of the 16-element array from $\theta = 20\,°$ to $\theta = 45\,°$. As the pattern of the overall array equals the product of array factor and single antenna pattern, the adjustment of the desired radiation is more precise for greater N.

Furthermore, one can see that the sidelobes of the three-element array factor are greater than those of the 16-element array factor. In figure 3.1b the array factor for $N = 3$ has a relative sidelobe level of $-10\,\mathrm{dB}$ at $\theta = 20\,^\circ$. As the pattern of the single antenna has its maximum close to this direction, high sidelobes occur in the array pattern for this setup.

It is required that the main beam of the linear three-element array can be steered at least $\pm\ 20\,^\circ$ off broadside. The other defined requirements in table 3.6 apply for beam directions from $-20\,^\circ$ to $20\,^\circ$. Furthermore, a maximum variation of $1\,\mathrm{dB}$ in realized gain is accepted. The requirement for the realized gain variation takes account for the decrease of the realized gain for wide angles off broadside. The requirement for the maximum relative sidelobe level applies for E-plane and H-plane.

Due to the assembly of elements, there occurs mutual coupling. The value of the mutual coupling depends on the edge-to-edge spacing of the antenna elements and on the form of the array. By arraying the patches with the long edges W along a line, a E-plane array is formed. In contrast, a H-plane array is formed by arraying the patches with the short edge L along a line. The width W of the patches is about $0,48\lambda_0$ and the length L is about $0,25\lambda_0$. Typically, phased arrays possess a center-to-center spacing between $0,4\lambda_0$ to $0,7\lambda_0$ [6, p. 29]. Thus, the edge-to-edge spacing is shorter in the E-plane than in the H-plane for this thesis. According to [11, p. 1196] one can expect less coupling in the H-plane than in the E-plane due to weaker surface waves and the greater edge-to-edge spacing. To verify that the mutual coupling of the fabricated array is below $-10\,\mathrm{dB}$, a linear E-plane array must be developed. The reason for this decision is that it is more difficult to reach $-10\,\mathrm{dB}$ E-plane coupling than H-plane coupling. Thus, one can use the linear array for verification before the fabrication of the planar array, where mutual coupling inevitably occurs in E-plane and H-plane.

3.6 Planar array

The planar array consists of three arrayed linear arrays from the previous section. Therefore, the antenna beam can be steered in the hemisphere. However, only the steering in E-plane and H-plane can be measured with the measurement setup at *HAW Hamburg*. The steering toward other directions in ϕ_0 can only be verified with *CST* due to adjustable cut angles. Therefore, the defined requirements apply for E-plane and H-plane. The requirements of the planar 3x3 array are listed in table 3.7.

Parameter	**Required**
Scan angle θ_0	$> \pm 20\,^\circ$
Relative side lobe level	$< -10\,\mathrm{dB}$
Directivity	$> 14{,}5\,\mathrm{dBi}$
Realized gain	$> 13\,\mathrm{dBi}$
Realized gain variation	$< 1\,\mathrm{dB}$
Mutual coupling in E-plane	$< -10\,\mathrm{dB}$
Mutual coupling in H-plane	$< -20\,\mathrm{dB}$

Table 3.7: Required parameters of the planar 3x3 array

Assuming the beam of the linear array can be steered $20\,^\circ$ off broadside, the beam of the planar array shall be steered $20\,^\circ$ off broadside in any direction. The described considerations of the array factor in section 3.5 apply for the planar array in x- and y-direction. Thus, the accepted maximum relative sidelobe level is set to $-10\,\mathrm{dB}$ for all scan angles.

Simulations have revealed that a directivity at broadside of at least $14{,}5\,\mathrm{dBi}$ is a realistic value. To account for inaccuracies in the antenna elements and the substrate, the required realized gain is set to $13\,\mathrm{dBi}$. The variation in realize gain is set to $1\,\mathrm{dB}$ again.

The maximum accepted mutual coupling in the E-plane is set to $-10\,\mathrm{dB}$ and in the H-plane to $-20\,\mathrm{dB}$. These values are taken from [11, p. 1196], where mutual coupling is measured for different edge-to-edge spacings in both planes.

4 Conception and design of the phased array antenna demonstrator

This section describes the investigation of the components of the demonstrator in *CST* and *AWR*. The design of the components is accomplished step by step and the measurement results of one component influence the design of another. Thus, there are references to section 5, where deviations between simulation and measurement are explained. All simulation files can be obtained from the electronic appendix. There is a guide in appendix A, that describes the structure of the electronic appendix. Regarding the phase shifter and the power divider the width of all microstrip lines with a characteristic impedance of 50 Ω is set to 1,67 mm according to equation 2.16.

4.1 Phase shifter

Firstly, the quadrature hybrid is designed using *AWR*. Then, it is investigated how the varactor diode can be implemented to cause a phase shift. Based on earlier experiences varactor diodes from *Skyworks SMV123x* series are used in the simulation (R. Wendel: personal communication, 19.04.2021). The *SMV123x* series comprises hyperabrupt junction tuning varactors. This type of varactor diodes possesses a doping profile with a sharp change from N to P junction. Therefore, these varactor diodes enable a great capacitance change for the applied reverse voltage range [9].

4.1.1 Quadrature hybrid

Initially, the quadrature hybrid is simulated without load. Referring to figure 2.1 the impedance of the feed lines is set to 50 Ω. The impedance of the inner vertical arms is set to 50 Ω, whereas the impedance of the inner horizontal arms is set to $Z_0/\sqrt{2} \approx 70{,}71\,\Omega$. After equation 2.17 this causes an effective dielectric constant of approximately 2,853 for

the 50 Ω microstrip line and 2,975 for the 70,71 Ω microstrip line. Moreover, the 50 Ω quarter-wavelength lines have to equal approximately 7,92 mm and the 70,71 Ω lines have to equal 7,76 mm in length. All design values can be obtained from table 4.1.

Element	**Length**	**Width**	**Impedance**
Inner horizontal arms	7,76 mm	2,81 mm	70,71 Ω
Inner vertical arms	7,92 mm	1,67 mm	50 Ω
Feed lines	10 mm	1,67 mm	50 Ω

Table 4.1: Overview of the microstrip lines of the quadrature hybrid

The indicated lengths in the table are estimated. The used lengths can be obtained from the electronic appendix. The magnitudes of the hybrid are displayed in figure 4.1.

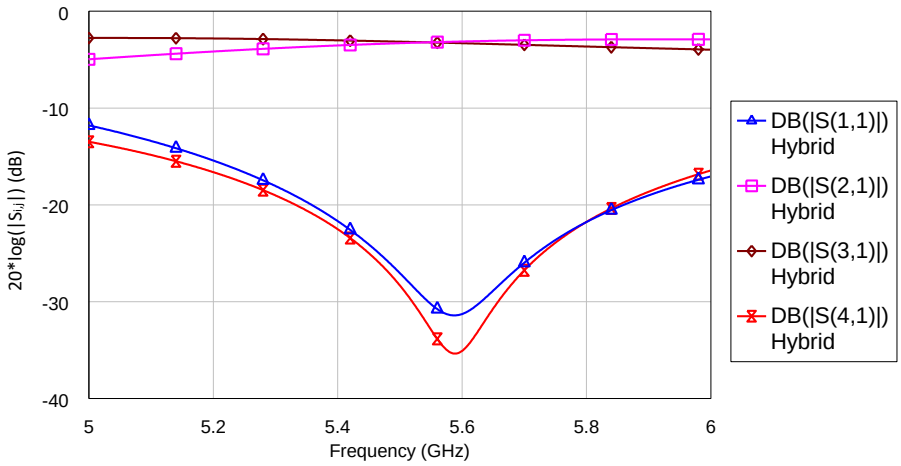

Figure 4.1: Simulated magnitudes of the quadrature hybrid

From the figure one can see that the return loss ($|S_{1,1}|$) is below −10 dB over the frequency. Port 4 is well isolated from port 1 as ($|S_{4,1}|$) is below −10 dB, too. The insertion losses ($|S_{2,1}|$) and ($|S_{3,1}|$) are between −2,8 dB and −5 dB. From 5,4 GHz to 5,75 GHz the magnitude variation is below 0,5 dB. The parameters $|S_{1,1}|$ and $|S_{4,1}|$ have their minimum at 5,6 GHz, which is below −30 dB, respectively.

The phases of the output ports 2 and 3 in relation to port 1 are shown in figure 4.2.

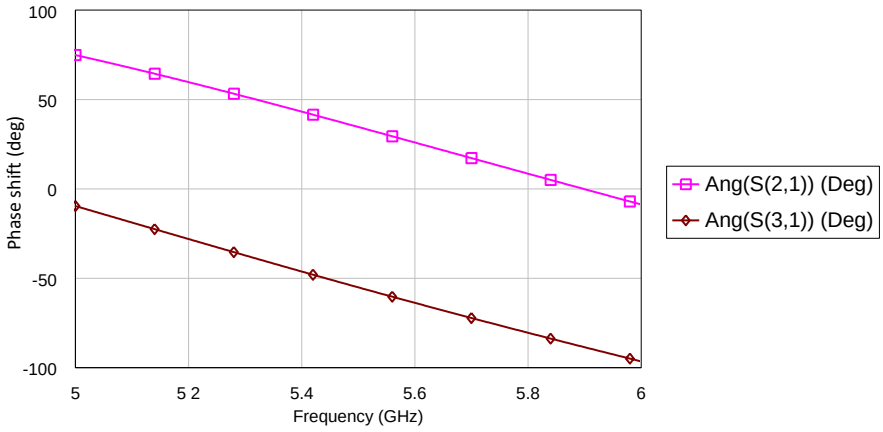

Figure 4.2: Simulated phase shift of port 2 and 3 relative to port 1 of the quadrature hybrid

Ideally, port 2 has a $-90°$ phase shift to port 1 and port 3 has a $-180°$ phase shift to port 1. However, in the simulation microstrip feed lines are shifting the signals phase. Moreover, the important parameter is the difference in the phase shift of $|S_{2,1}|$ to $|S_{3,1}|$, which is ideally $-90°$. In the simulation the phase difference is at least $-84,46°$ over the frequency range. At 5,6 GHz the difference in phase is $-89,73°$.

4.1.2 Varactor diode

In the following the initial investigation of the varactor diode *SMV1231* [9] is described. Other diodes have been studied as well. Here only the *SMV1231* is presented as it provides the greatest relative phase shift.

The varactor diode is used in reverse mode as load of the quadrature hybrid. To reverse bias the diode, a DC voltage has to be applied. Therefore, a DC blocking capacitor, which has a low impedance at 5,6 GHz, has to be implemented between hybrid and diode. To block the RF signal from the DC supply, the DC voltage is applied by a short-circuited quarter-wavelength microstrip line. The short-circuit at the end of the microstrip line is realized by a capacitor to ground.

The corresponding circuit without hybrid is shown in figure 4.3.

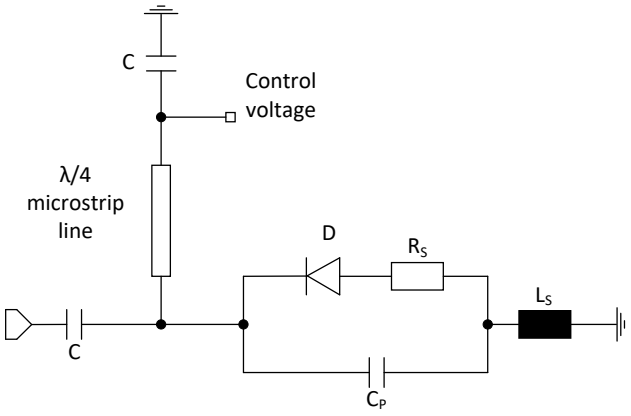

Figure 4.3: Schematic of one series-resonated varactor diode

The capacitors are chosen to *C0G* ceramic capacitors in size *0603* from *EPCOS* with a capacitance of 1 pF. The quarter-wavelength microstrip line has a length of 7,92 mm and an impedance of 50 Ω. Assuming the capacitor at the end of the quarter-wavelength line as RF short-circuit, the quarter-wavelength line can be assumed as RF open-circuit. The components C_p, R_s and L_s are parasitic components of the varactor diode. For simulation these components are modeled as lumped elements. All parameters regarding the varactor diode in this section are taken from [9]. The diode is modeled using the *SPICE* model provided by *Skyworks*, which can be found in the electronic appendix A.17. The values of all used components are listed in table 4.2.

Besides the circuit with one varactor diode in series, a circuit with two varactor diodes in series is simulated as well. The second diode of this circuit is appended to the one of the circuit in figure 4.3. However, a DC blocking capacitor is inserted between both diodes. Furthermore, to direct the DC signal from the first diode to ground a RF choke is set to ground behind the diode. The RF choke is chosen to a *WE-CAIR Air coil* from *Würth Elektronik* with an inductance of 5,45 nH. The second diode is reverse biased in the same manner as the first diode.

The corresponding circuit is displayed in figure 4.4.

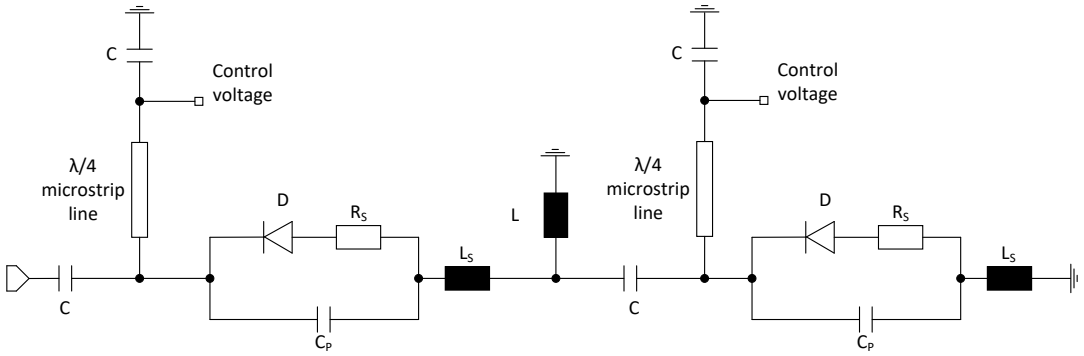

Figure 4.4: Schematic of two series-resonated varactor diodes

Both circuits are used to determine the achievable relative phase shift of one or rather two varactor diodes. In *AWR* the circuits are fed by a port and the reflection coefficient is investigated. Table 4.2 summarizes all used components.

Element	**Value**	**Manufacturer**	**Information**
C_p	0,44 pF	*Skyworks*	[9]
R_s	2,5 Ω	*Skyworks*	[9]
L_s	0,7 nH	*Skyworks*	[9]
D	see *SPICE* model	*Skyworks*	[9]
C	1 pF	*EPCOS*	[7]
L	5,45 nH	*Würth Elektronik*	[10]
$\lambda_d/4$ microstrip line	7,92 mm x 1,67 mm	-	-

Table 4.2: Overview of the components of the phase shifter

According to *Skyworks* the maximum reverse voltage is 15 V. Hence, in the simulation an ideal voltage source is swept from 0 V to 15 V. Referring to equation 2.12 the phase of the reflection coefficient of this circuit is of interest. The relative phase shift of $S_{1,1}$ is displayed in figure 4.5 for control voltages from 0 V to 15 V for the described circuits.

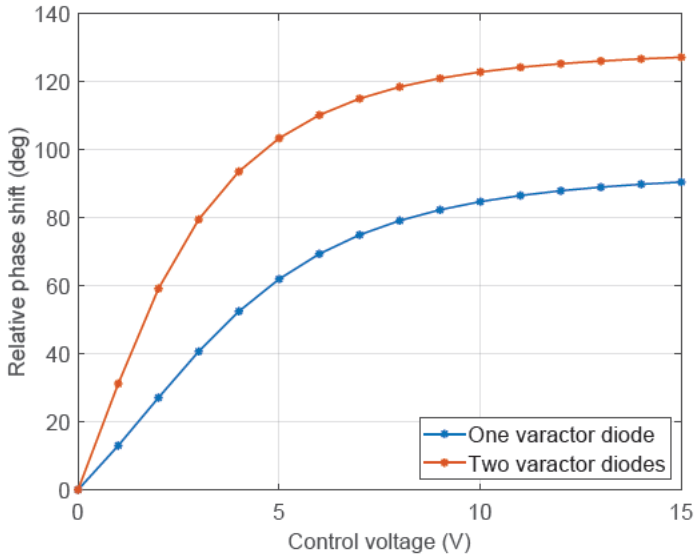

Figure 4.5: Simulated relative phase shift versus control voltage at 5,6 GHz of one and two series-resonated varactor diodes

For control voltages up to 5 V the relative phase shift of both circuits strongly increases. Then the gradient of both curves decreases and the relative phase shift flattens. The maximum phase shift of the circuit with one series-resonated varactor diode is 90,54 °, whereas the maximum of the circuit with two diodes is 127,24 °. Therefore, both circuits do not provide enough phase shift.

In a practical design there need to be microstrip lines between the components to permit space for soldering. Thus, the circuit in figure 4.4 is upgraded with microstrip lines connecting the components. All microstrip lines have an impedance of 50 Ω and are kept short. The connections to ground are realized by a via at the appropriate locations.

The relative phase shift and the return loss of this circuit are displayed in figure 4.6.

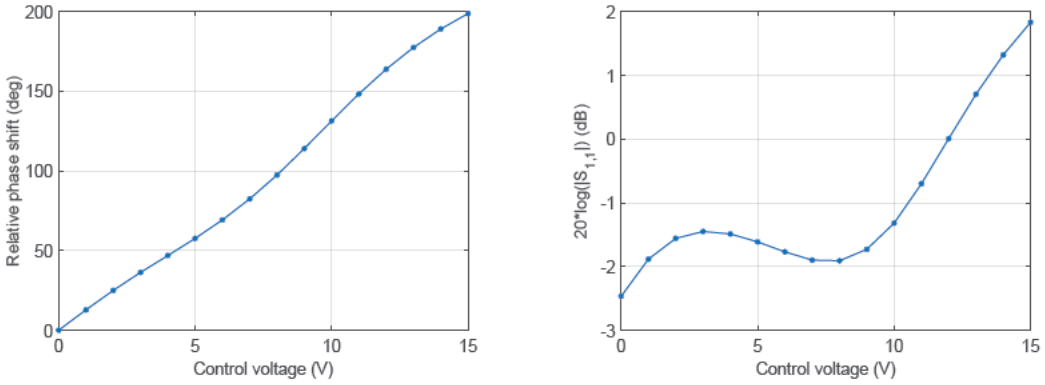

(a) Relative phase shift

(b) Return loss

Figure 4.6: Simulated performance versus control voltage at 5,6 GHz of two series-resonated varactor diodes with microstrip lines

From the figure one can see that the circuit with two varactor diodes in series now enables a phase shift of 198,74 °. The microstrip line between the varactor diodes has a length of 3,67 mm, which is about 0,1 λ_d. A ratio of the incident power wave, that passes the first diode, is reflected by the second one. Due to the microstrip line between the diodes, this ratio undergoes a phase shift.

The increased relative phase shift of this circuit can be explained due to the microstrip lines between the diodes. The reflected power waves of both diodes interfere and may destructively add in phase. By adjusting the length of the microstrip line between the diodes the total relative phase shift can be increased. The circuit exhibits a large return loss variation, which is about 4,3 dB and is caused by the parasitic elements of the varactor diodes. However, this variation is initially accepted as simulation and measurement may differ.

4.1.3 Simulation of the phase shifter

The phase shifter is realized by appending the circuit from figure 4.4, including microstrip lines between the components, to the ports 2 and 3 of the hybrid, respectively. Both branches are controlled with the same DC voltage source. To eliminate the need of cables, a microstrip line of width 0,4 mm connects the points where the DC supply is applied. Consequently, for the measurement of the phase shifter one cable from the circuit to a voltage source is required. The layout of the phase shifter is shown in figure 4.7.

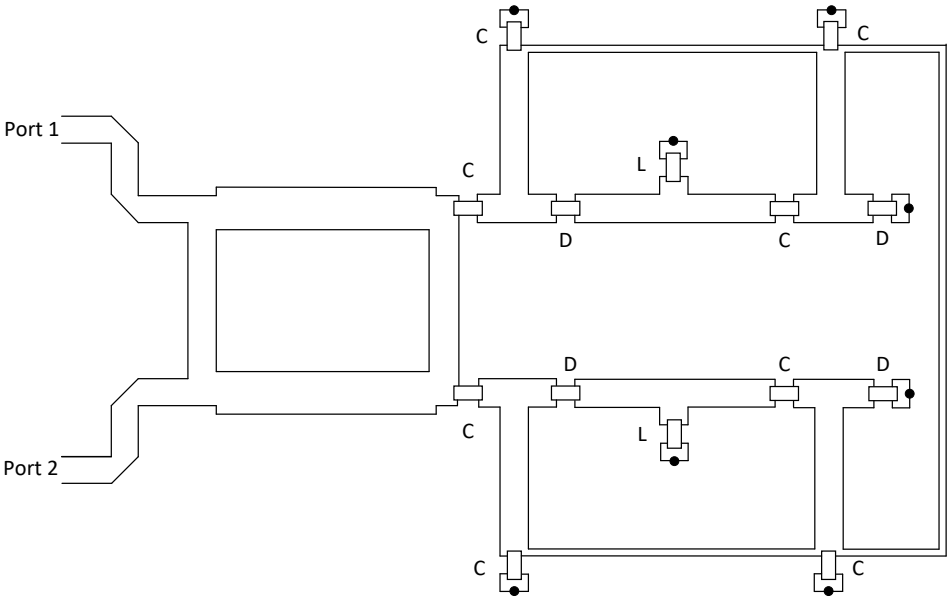

Figure 4.7: Layout of the phase shifter

To provide space for soldering SMA connectors to the board, the feed lines to the ports of the hybrid are bent. The load is directly appended to the end of the horizontal arms and the electronic components are marked with the appropriate indication. Vias to ground are marked by a black dot. In a first design the microstrip line between the diodes is set to 3,67 mm, just like in section 4.1.2. However, measurements have revealed that this design is not sufficient regarding the maximum relative phase shift. The simulation and measurement result of the first design are presented in appendix C.1. To increase the maximum relative phase shift, the length of the microstrip line is set to 10,67 mm.

The return loss and the insertion loss of the enhanced design are displayed in figure 4.8.

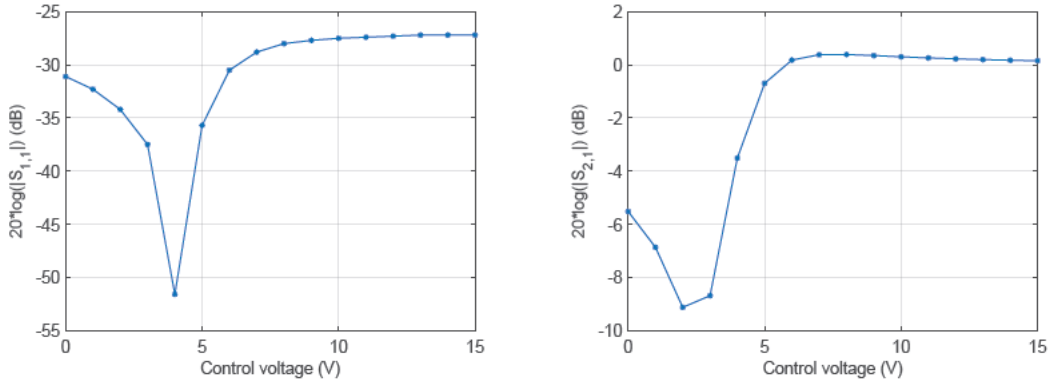

(a) Return loss (b) Insertion loss

Figure 4.8: Simulated performance of the enhanced phase shifter versus control voltage at 5,6 GHz

The relative phase shift for control voltages from 0 V to 15 V is shown in figure 4.9.

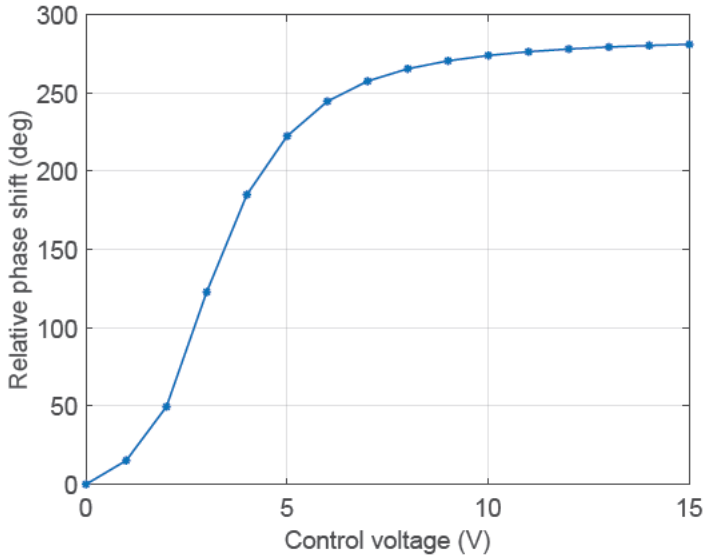

Figure 4.9: Simulated relative phase shift of the enhanced phase shifter versus control voltage at 5,6 GHz

In figure 4.9 one can see that the maximum relative phase shift is about 280 °. For control voltages greater than 7 V the change in relative phase shift significantly decreases. The return loss is below −25 dB for all control voltages. However, the variation in the insertion loss is about 9,51 dB, which is an unacceptable result. The simulation results are listed in table 4.3 and compared to the requirements.

Parameter	**Required**	**Min.**	**@ 5,6 GHz**	**Max.**	**Satisfied**
Bandwidth	$> 5\,\%$	-	-	-	✓
Relative phase shift	$> 180\,°$	-	280 °	-	✓
Insertion loss	> -5 dB	−9,6 dB	-	0,703 dB	×
Return loss (In.)	< -10 dB	−51,6 dB	-	−15,44 dB	✓
Insertion loss variation	< 3 dB	-	9,51 dB	-	×

Table 4.3: Comparison of the simulated and required parameters of the phase shifter for frequencies from 5,32 GHz to 5,88 GHz for control voltages from 0 V to 15 V

The simulation results of the phase shifter for the frequencies 5,32 GHz and 5,88 GHz are shown in appendix C.2. At 5,32 GHz the relative phase shift is about 228 ° and at 5,88 GHz about 293 °. The return loss is below −10 dB and the insertion loss is similar to that of 5,6 GHz over the frequency range. Therefore, the requirement for the bandwidth is fulfilled.

Although the insertion loss variation is not acceptable, the design is fabricated. During the measurements of several components it is observed that *AWR* suffers from calculating the attenuation of circuits. Furthermore, the simulation of the varactor diode is inaccurate as lumped elements are used to model the parasitic elements. For these reasons the design is fabricated for further investigation and evaluated in section 5.1.

4.2 Wilkinson power divider

The design of the Wilkinson power divider is described in this section. Firstly, a two-way divider is designed. Then, a 16-way divider is designed with the two-way divider as main component. Seven ports are terminated with a 50 Ω impedance and nine ports can be used for the antenna application.

4.2.1 Two-way Wilkinson power divider

The challenge in the design is to meet quarter-wavelength for the microstrip lines in the center of the circuit. To save space the quarter-wavelength lines are bent. As the ends of the quarter-wavelength lines are connected through the shunt resistor Z_R they have to be closely placed. The space for Z_R equals 1,04 mm. To permit space for soldering of each SMA connector, the 50 Ω output lines are bent as well. The two-way Wilkinson power divider in microstrip line form is shown in figure 4.10.

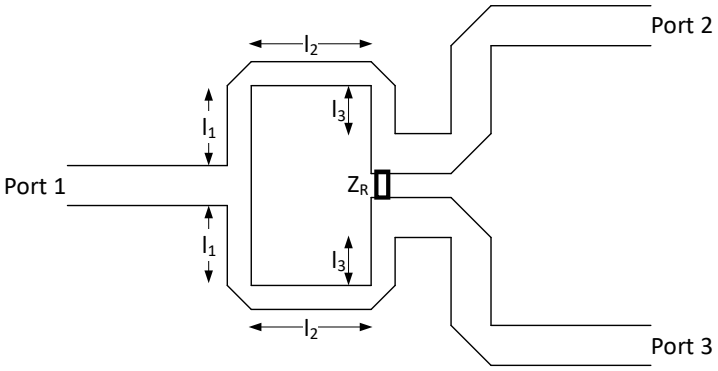

Figure 4.10: Layout of the two-way Wilkinson power divider, following [14, p. 328]

According to equation 2.13 the shunt resistor Z_R is set to 100 Ω. According to equations 2.14 and 2.15 the characteristic impedance of the quarter-wavelength lines has to be 70,7 Ω to enable an equal power split. Thus, in accordance to equation 2.16 the width is set to 0,9 mm. The total length of both lines has to equal approximately 8,1 mm. To save space and minimize attenuation, the lengths of the 50 Ω lines are kept short.

The characteristic values of each line can be obtained from table 4.4.

Parameter	Width	Length
l_1	0,9 mm	2,5 mm
l_2	0,9 mm	3,45 mm
l_3	0,9 mm	1,05 mm

Table 4.4: Designed lengths and widths of the quarter-wavelength line of the two-way Wilkinson power divider

In *AWR* the length of the center component of the quarter-wavelength line, referred to as line l_2 in figure 4.10, is set as a variable. The optimal value is obtained by sweeping the variable, whereas the other components of the quarter-wavelength line are set to $l_1 = 2{,}5\,\text{mm}$ and $l_3 = 1{,}05\,\text{mm}$. Taking the bend and a part of the transitions from the $70{,}7\,\Omega$ line to the $50\,\Omega$ line into account the value of the line l_2 should be in the range of 3 mm to 4 mm. In accordance with section 3 good results are obtained when l_2 equals 3,45 mm. The frequency response of the designed divider is displayed in figure 4.11.

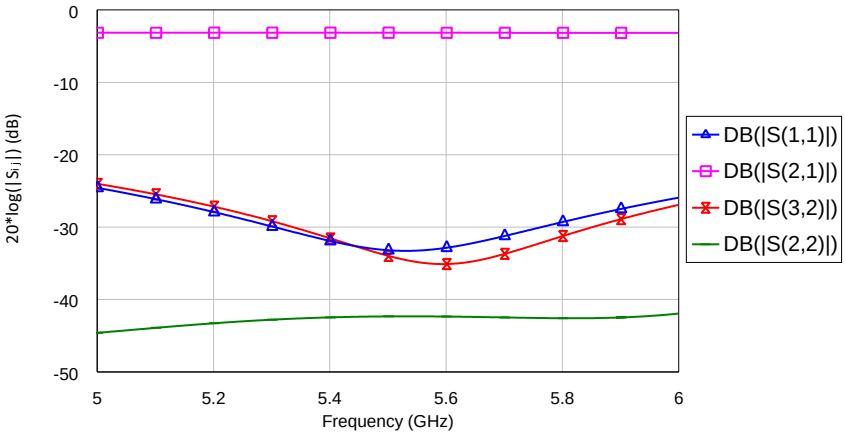

Figure 4.11: Simulated performance of the two-way Wilkinson power divider

As one can see from figure 4.11 the divider has a constant insertion loss of approximately $-3{,}15\,\text{dB}$ over the range of 5 GHz to 6 GHz. $|S_{3,1}|$ equals $|S_{2,1}|$ due to symmetry. The same also applies for $|S_{2,2}|$ and $|S_{3,3}|$ as well as $|S_{3,2}|$ and $|S_{2,3}|$. For this reason only one value is displayed, respectively. For the range of 5 GHz to 6 GHz the return loss at all ports is below $-20\,\text{dB}$ and isolation between port 2 and port 3 is below $-40\,\text{dB}$. Thus,

the Wilkinson power divider is well matched at all ports and offers equal power split. The electrical specifications are summarized in table 4.5.

Parameter	**Required**	**Min.**	**@ 5,6 GHz**	**Max.**	**Satisfied**
Insertion loss	$> -4\,\text{dB}$	$-3{,}171\,\text{dB}$	$-3{,}154\,\text{dB}$	$-3{,}15\,\text{dB}$	✓
Isolation	$< -15\,\text{dB}$	$-44{,}6\,\text{dB}$	$-42{,}35\,\text{dB}$	$-41{,}94\,\text{dB}$	✓
Return loss (In.)	$< -10\,\text{dB}$	$-33{,}28\,\text{dB}$	$-32{,}86\,\text{dB}$	$-24{,}57\,\text{dB}$	✓
Return loss (Out.)	$< -10\,\text{dB}$	$-35{,}1\,\text{dB}$	$-35{,}1\,\text{dB}$	$-24{,}01\,\text{dB}$	✓

Table 4.5: Comparison of the simulated and required parameters of the two-way Wilkinson power divider for frequencies from 5 GHz to 6 GHz

The magnitude and phase balance are not listed in the table as the simulation results are not meaningful for these parameters. Due to the symmetry, the output ports are in balance in the simulation. The designed two-way divider is fabricated to verify the performance and to use it as main component of the 16-way divider.

4.2.2 16-way Wilkinson power divider

The 16-way divider is realized by a four stage cascade of two-way dividers. Every junction equals the divider from the previous section. All two-way dividers are connected using 50 Ω microstrip lines. These lines are kept short to save space and minimize attenuation. Seven of the outputs are terminated with a 50 Ω resistor on the circuit board. The other nine outputs are used as ports for the antenna application. A draft of the 16-way divider is shown in figure 4.12.

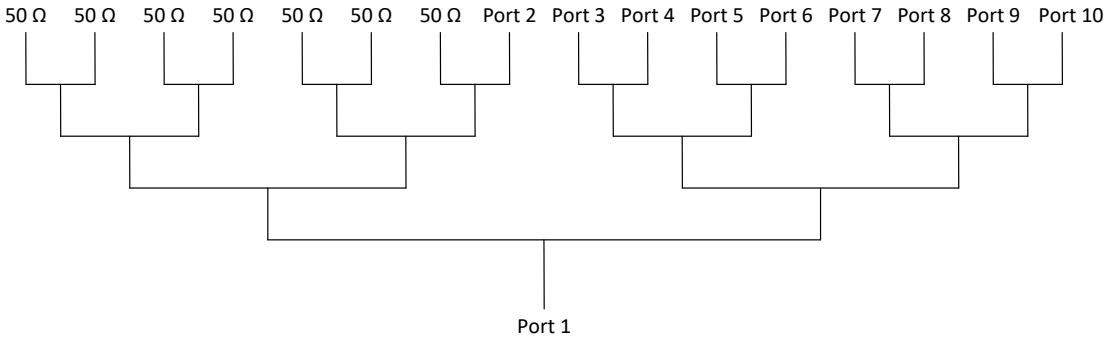

Figure 4.12: Draft of the 16-way Wilkinson power divider

The lengths of the connecting 50 Ω lines can be obtained from the simulation files. Referring to figure 4.10 the microstrip line l_2 is changed to a length of 3,15 mm. This is a conclusion of the measure of the two-way divider and is explained in section 5.2.1.

In figure 4.13 the insertion loss of the designed divider is displayed. Referring to figure 4.12 port 2 is separated from the other ports by the first junction. This is the reason why $S_{2,1}$ does not equal $S_{3,1}$. As the insertion loss of port 4 to 10 equals $S_{3,1}$, these are not displayed in the figure.

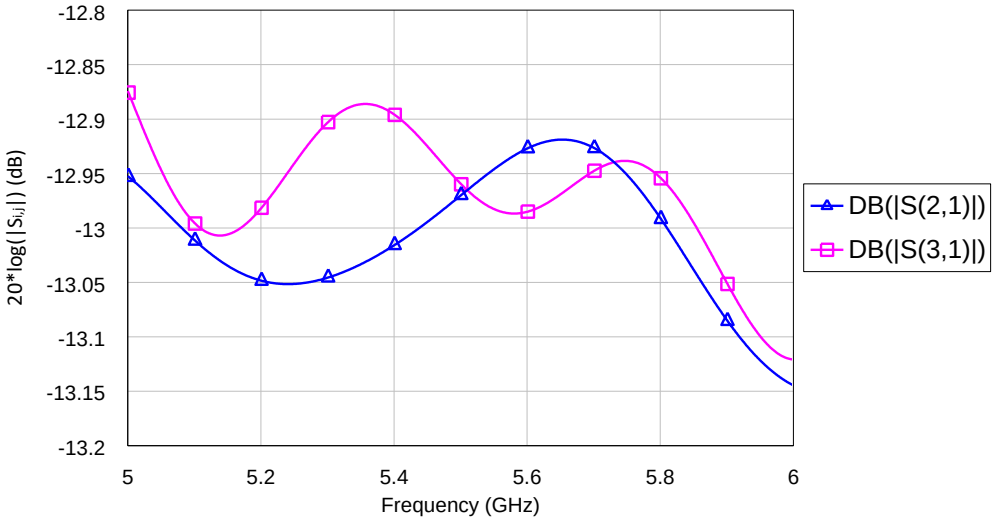

Figure 4.13: Simulated insertion loss of the 16-way Wilkinson power divider

From the figure one can see that the insertion loss is approximately −13 dB in the frequency range from 5 GHz to 6 GHz. The lossy microstrip lines cause the loss of 1 dB in comparison with an ideal divider. The maximum magnitude deviation is at 5,31 GHz and is approximately 0,15 dB. The outputs phases in reference to port 1 are almost identical and are, therefore, not displayed. The phase deviation is approximately 0,3 ° and is constant over the frequency.

In figure 4.14 the return loss of the designed divider is shown. As the return loss of ports 3 to 10 is identical due to symmetry, only the return loss of port 3 is displayed.

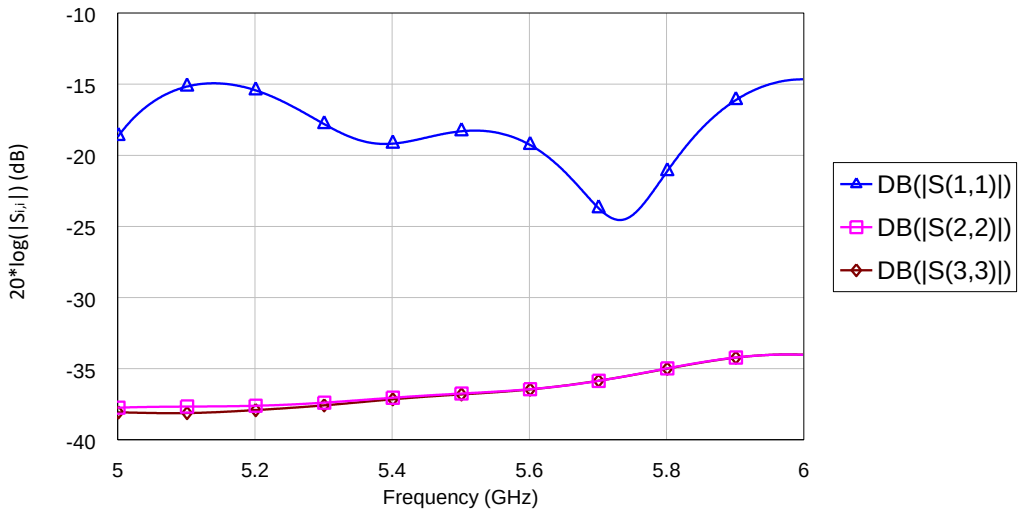

Figure 4.14: Simulated return loss of the 16-way Wilkinson power divider

The return loss of ports 2 to 10 is below −30 dB over the frequency range from 5 GHz to 6 GHz and satisfies the defined requirements. The return loss at port 1 is almost below −15 dB over the frequency range. At 5,14 GHz and 5,95 GHz the return loss is slightly above −15 dB. At 5,73 GHz there is a minimum of −24,55 dB. It would be possible to shift the minimum toward 5,6 GHz in the simulation. However, this is not expedient as the manufactured circuit is the component of interest. Overall, the simulated return loss satisfies the defined requirements.

The isolation of the simulated divider is displayed in figure 4.15. Referring to figure 4.12 the outputs are separated by a different number of junctions. For this reason the isolation from port 3 to one port of every final junction is shown exemplary.

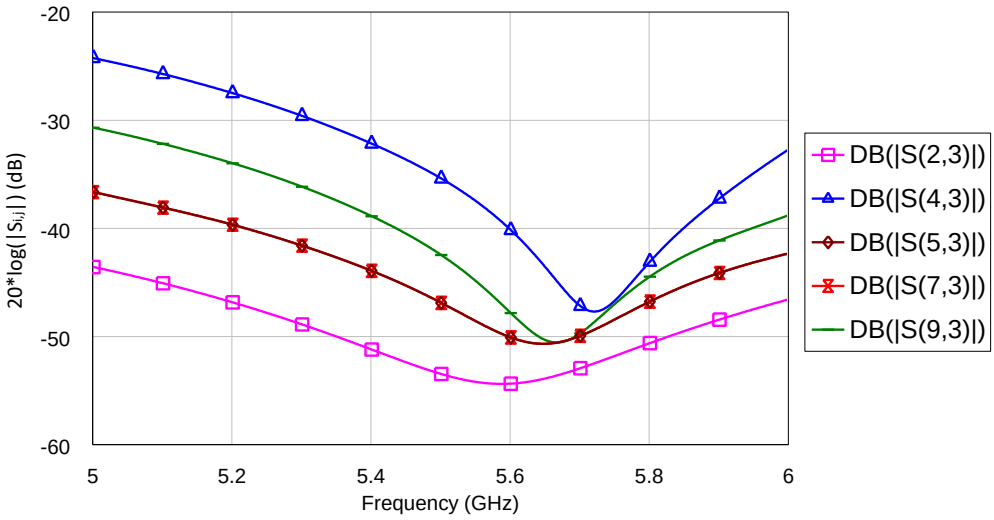

Figure 4.15: Simulated isolation of the 16-way Wilkinson power divider

Due to the geometry, $S_{9,3}$ equals $S_{10,3}$, and $S_{5,3}$, $S_{6,3}$, $S_{7,3}$ and $S_{8,3}$ are identical. From the figure it is apparent that the isolation between the outputs is below $-20\,\mathrm{dB}$ over the frequency range from $5\,\mathrm{GHz}$ to $6\,\mathrm{GHz}$. Differences in the isolation can be explained with the different number of junctions between two outputs.

The characteristic parameters of the divider are summarized and compared with the required values in table 4.6.

Parameter	**Required**	**Min.**	**@ 5,6 GHz**	**Max.**	**Satisfied**
Insertion loss	$> -15\,\mathrm{dB}$	$-13{,}14\,\mathrm{dB}$	$-12{,}99\,\mathrm{dB}$	$-12{,}87\,\mathrm{dB}$	✓
Isolation	$< -15\,\mathrm{dB}$	$-24{,}24\,\mathrm{dB}$	$-54{,}37\,\mathrm{dB}$	$-54{,}39\,\mathrm{dB}$	✓
Return loss (In.)	$< -10\,\mathrm{dB}$	$-24{,}55\,\mathrm{dB}$	$-19{,}24\,\mathrm{dB}$	$-14{,}66\,\mathrm{dB}$	✓
Return loss (Out.)	$< -10\,\mathrm{dB}$	$-38{,}08\,\mathrm{dB}$	$-36{,}45\,\mathrm{dB}$	$-34{,}01\,\mathrm{dB}$	✓

Table 4.6: Comparison of the simulated and required parameters of the 16-way Wilkinson power divider for frequencies from 5 GHz to 6 GHz

As the simulated divider satisfies the defined requirement for the given frequency range, it is fabricated and measured. The measurements are analyzed in section 5.2.2.

4.3 Feed network module

For the array application, where the 3x3 planar array is investigated, the 16-way Wilkinson power divider and nine phase shifters have to be merged. The input port of each phase shifter has to be connected with one output port of the divider, respectively. This is accomplished by putting the divider and the phase shifters on the same circuit board. To enable enough space for the phase shifters, the main junction of the divider directs the branches to opposite sides. A draft of the module is displayed in figure 4.16.

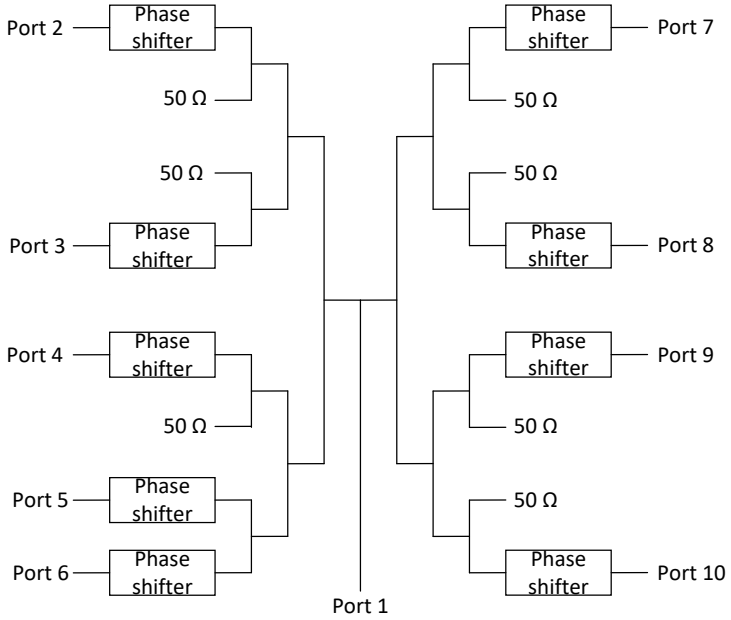

Figure 4.16: Draft of the feed network module

The circuit can be fed by a network analyzer from port 1 in the lower middle. The module has five output ports on the left and four output ports on the right side, that are used for the antenna application. Except for port 6 and 5, all ports are adjacent to a 50 Ω termination of the divider. To enable enough space for the SMA connectors the microstrip lines of port 5 and 6 are bent.

In the simulation an ideal voltage source is used to control the phase shifter. However, for the fabricated feed network module a DC supply circuit has to be developed. Therefore, two 9 V batteries in series are used as voltage source. A 1,2 kΩ wire resistor

in series with the batteries limits the current of the circuit. To supply each phase shifter, nine 100 kΩ potentiometers are placed in parallel behind the wire resistor. The sliding contact of each potentiometer is connected to one phase shifter, respectively. Thus, each phase shifter can be manually adjusted. A draft of the DC circuit is shown in figure 4.17.

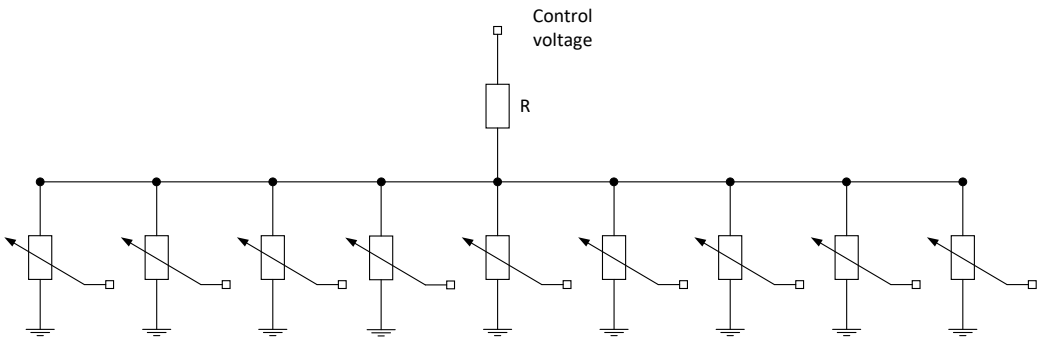

Figure 4.17: Schematic of the DC supply circuit

Assuming the reverse biased varactor diodes as high-resistance, the control voltage solely depends on the adjusted potentiometer. To compare the design to the requirements in section 3.3, the characteristic parameters of the module are listed in table 4.7.

Parameter	**Required**	**Satisfied**
Weight	$< 2\,\mathrm{kg}$	-
Size	$< 30\,\mathrm{cm}$ x $20\,\mathrm{cm}$	✓
DC supply	internal	✓
Radiation	$< -20\,\mathrm{dB}$	-

Table 4.7: Comparison of the designed and required parameters of the feed network module

The internal DC supply and the maximum size of the circuit board are realized by the design and satisfy the defined requirements. The weight and the radiation of the module have to be measured after fabrication.

4.4 Microstrip antenna

The characteristic of a single microstrip antenna is in principle determined by its length L, its width W and the feeding method. In reference to table 1.1 all other parameters are predetermined for this thesis. The first step in the design is to develop an antenna feed for simulation purpose. The feed should be similar to that one used for the measurement. Afterwards, the length and the width of the microstrip antenna are investigated.

4.4.1 Antenna feed

As explained in section 3.4.1 an antenna with feed probe must be designed for this thesis. In fabrication, this is accomplished by drilling a narrow hole through the patch and soldering a SMA connector from the bottom side to the ground plane. The inner pin is then soldered to the patch.

A draft of a microstrip antenna with feed probe is shown in figure 2.5b. As the SMA connector must have a characteristic impedance of $50\,\Omega$, the radius of the inner pin is set to 0,4 mm and the radius of the substrate is set to 1,34 mm according to equation B.1. The square interface has an edge length of 12 mm. The substrate is set to Teflon with a dielectric constant of $\varepsilon_r = 2{,}1$.

4.4.2 Simulation of the microstrip antenna

In the following the analysis of the figures of merit of the microstrip antenna is described. The simulation files can be obtained from the electronic appendix A.9.

Resonant frequency

Firstly, the length of the patch has to be determined. Referring to equation 2.19 the length should be set to slightly less than one-half wavelength in the substrate to account for fringing and to excite the TM_{10} mode at 5,6 GHz. The footprint of the antenna is set to 40 mm x 40 mm, the width of the patch is set to $W = 0,5\lambda_0$ and the feed probe is placed in the center of one radiating edge at $y_0 = 0$ mm.

The resonant frequency dependence on the length L for this setup is displayed in figure 4.18.

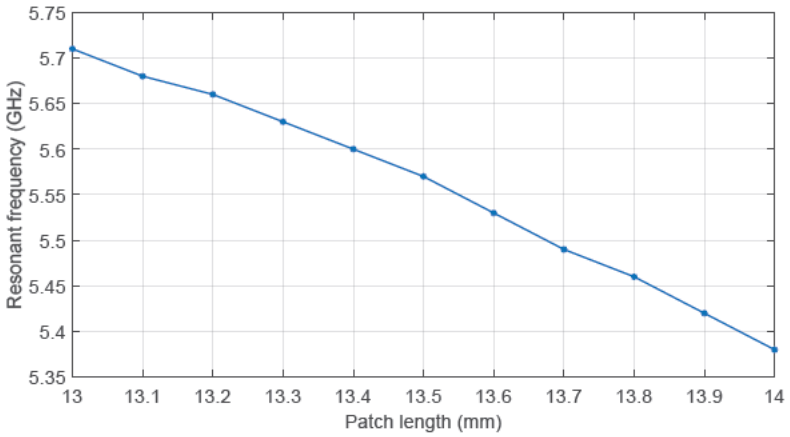

Figure 4.18: Dependence of the resonant frequency on the patch length ($W = 0,5\lambda_0$, y_0= 0 mm, $\varepsilon_r = 3{,}66$)

From the figure one can see that good agreements to 5,6 GHz are obtained with lengths close to 13,4 mm, which is less than one-half wavelength in the substrate. The resonant frequency decreases for greater lengths.

Input impedance

The antenna has to be matched to 50 Ω. Therefore, the input impedance of the antenna is considered in the Smith Chart. From figure 4.18 it is apparent that lengths from 13,2 mm to 13,5 mm cause a resonant frequency close to 5,6 GHz. The input impedance loci for these lengths are shown in figure 4.19.

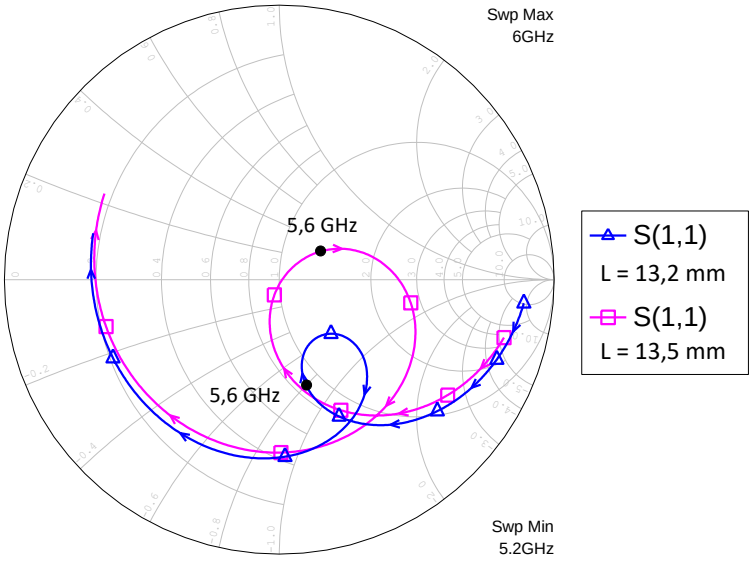

Figure 4.19: Input impedance of the microstrip antenna for $L = 13{,}2\,\text{mm}$ and $L = 13{,}5\,\text{mm}$ ($W = 0,5\lambda_0$, $y_0 = 0\,\text{mm}$, $\varepsilon_r = 3{,}66$)

The desired resonant frequency of 5,6 GHz is highlighted by the black dots for both loci. One can see that the increase of the length causes the locus to shift upwards. In contrast, the decrease of the length causes the locus to become narrow.

Based on further analyses the length of the antenna is set to 13,3 mm and the width is set to 25,7 mm. This is a trade-off between all figures of merit. This geometry provides high directivity, broadside radiation, an acceptable bandwidth of about 2,3 % and a resonant frequency of 5,6 GHz. The input impedance of this geometry is matched by insetting the feed probe by $y_0 = 2{,}42\,\text{mm}$.

The input impedance loci of the designed antenna are displayed in figure 4.20 for $y_0 = 0\,\text{mm}$ and $y_0 = 2{,}42\,\text{mm}$.

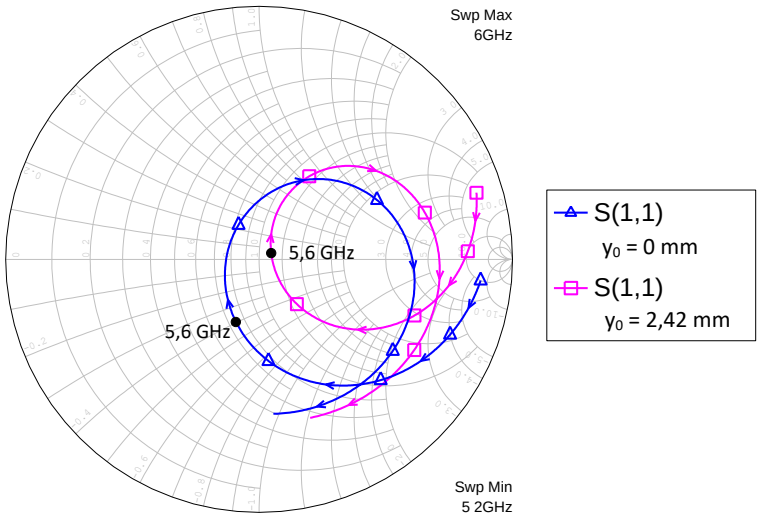

Figure 4.20: Input impedance of the designed microstrip antenna for $y_0 = 0\,\text{mm}$ and $y_0 = 2{,}42\,\text{mm}$ ($L = 13{,}3\,\text{mm}$, $W = 25{,}7\,\text{mm}$, $\varepsilon_r = 3{,}66$)

The input impedance of the antenna at 5,6 GHz for $y_0 = 0\,\text{mm}$ is $Z_{in} = (37{,}17 - 19{,}38\text{i})\,\Omega$. The inset increases the real and the imaginary part. Therefore, an input impedance of $Z_{in} = (55{,}21 + 1{,}26\text{i})\,\Omega$ is obtained. In the design it is almost achieved to eliminate the imaginary part. As it is cumbersome to achieve a perfect match and the fabricated antenna is of interest, no more effort is spend to enhance the match.

In section 2.3.2 it is described that the input impedance of the antenna decreases due to insetting the feed. However, the inset in the simulation causes an increase of the input impedance. This circumstance has to be investigated in the future.

Bandwidth

The bandwidth is defined for $VSWR \leq 2, |\Gamma| \leq 1/3$. Regarding the return loss this equals $S_{1,1} \leq -9{,}54\,\text{dB}$. The return loss of the microstrip antenna is displayed in figure 4.21.

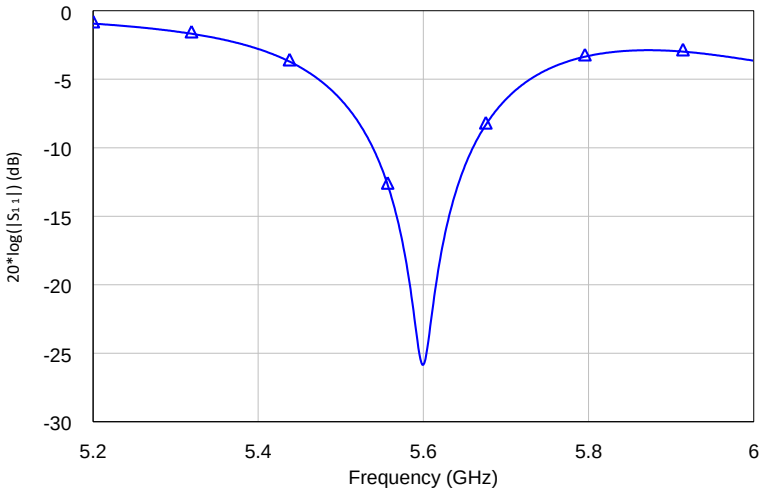

Figure 4.21: Return loss of the microstrip antenna ($L = 13{,}3\,\text{mm}$, $W = 25{,}7\,\text{mm}$, $y_0 = 2{,}42\,\text{mm}$, $\varepsilon_r = 3{,}66$)

The lower band edge is at 5,535 GHz and the upper band edge is at 5,664 GHz. Hence, the resonant frequency is well centered and the bandwidth is about 2,3 %.

Directivity

As the antenna width is the most contributing factor to obtain a high directivity, the dependence of the directivity on the width for different lengths is investigated. In accordance with figure 4.18 the following simulation is performed for the lengths 13,2 mm, 13,3 mm, 13,4 mm and 13,5 mm to obtain a resonant frequency close to 5,6 GHz. The dependence of the directivity on length and width is shown in figure 4.22.

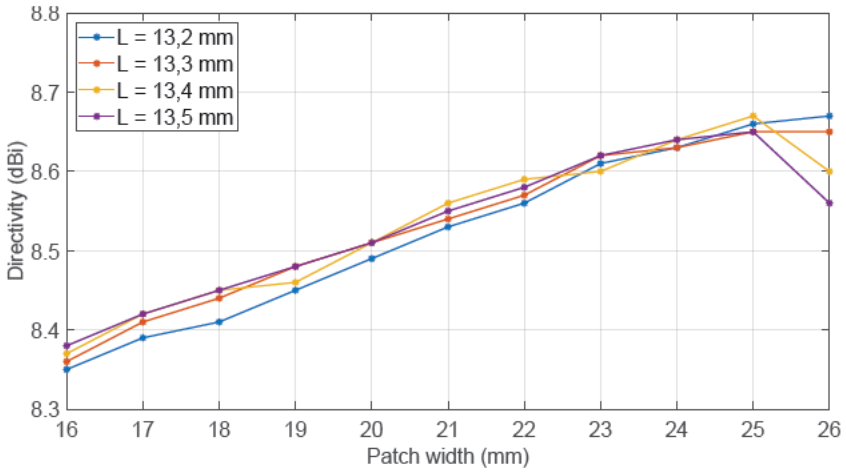

Figure 4.22: Dependence of the directivity on the patch length and width (y_0= 0 mm, ε_r = 3,66)

One can see that the directivity is between 8,3 dBi and 8,7 dBi for the antenna geometries. Thus, all combinations of length and width satisfy the required directivity of 7 dBi. The directivity of the designed patch is 8,62 dBi. It is observed that the inset of the feed does not affect the directivity. The realized gain is 7,74 dBi.

Radiation pattern

The patterns of the designed antenna are displayed in figure 4.23. The patterns indicate the directivity.

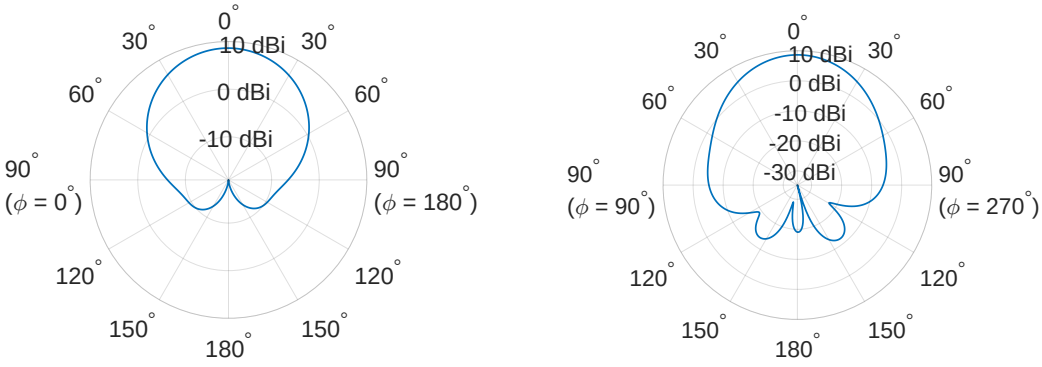

(a) E-plane (b) H-plane

Figure 4.23: Radiation patterns of the designed microstrip antenna

The slightly unsymmetrical radiation in the H-plane to the bottom side is due to the feed. Both planes have their maximum at $\theta_0 = 0\,°$. The far-field of the antenna is shown in figure 4.24.

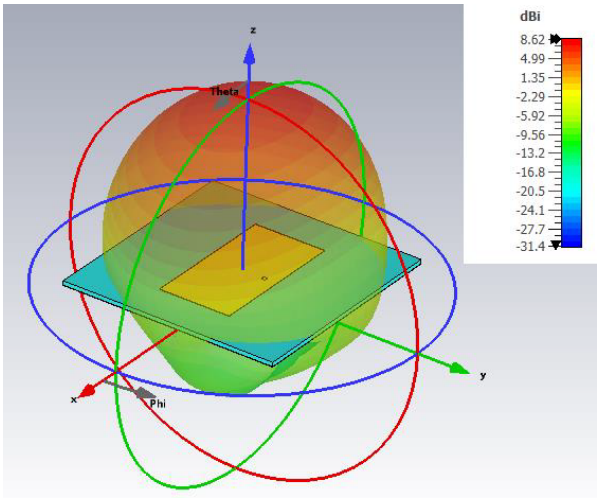

Figure 4.24: Far-field of the designed microstrip antenna

In the design procedure it is observed that slightly misplaced feeds and edge lengths cause the antenna to radiate a few degrees from broadside. Emphasis is placed on a design with broadside radiation.

Sidelobe level

From figure 4.23 one can see that the microstrip antenna has no sidelobes in the E-plane. In the H-Plane there are sidelobes at $\theta \approx 140\,^\circ$. The relative sidelobe level is $-20{,}5\,\mathrm{dB}$.

The characteristic values of the microstrip antenna are displayed in table 4.8 and are compared to the defined requirements.

Parameter	**Required**	**Simulated**	**Satisfied**
Resonant frequency	5,6 GHz ± 56 MHz	5,6 GHz	✓
Input impedance @ 5,6 GHz	$50\,\Omega \pm (10 + 10\mathrm{i})\,\Omega$	$(55{,}21 + 1{,}26\mathrm{i})\,\Omega$	✓
Bandwidth	$> 2\,\%$	2,3 %	✓
Directivity	$> 7\,\mathrm{dBi}$	8,62 dBi	✓
Realized gain	$> 5{,}5\,\mathrm{dBi}$	7,74 dBi	✓

Table 4.8: Comparison of the designed and required parameters of the microstrip antenna

The designed antenna fulfills the requirements and is fabricated and evaluated in section 5.5.

4.5 Linear array

To form a linear array, three patches from the previous section 4.4 are placed next to each other. The spacing d between the center of the components is the elementary aspect in the design of the linear array. Firstly, the array factor is briefly investigated. Then several spacings are simulated in *CST* and the performance of the arrays are compared.

4.5.1 Array factor

As already mentioned in section 3.5, phased arrays typically possess a spacing between $0,4\lambda_0$ to $0,7\lambda_0$. For spacings greater or equal than λ_0 there occur secondary maxima due to the array factor. According to equation 2.29 the expression of the array factor exhibits several maxima for $d \geq \lambda_0$ as the sine expressions take the value of zero. As secondary maxima are undesired, the spacing d is usually smaller than λ_0.

The normalized array factor of a linear three-element array for $d = 0,4\lambda_0$ and $d = 0,7\lambda_0$ is shown in figure 4.25.

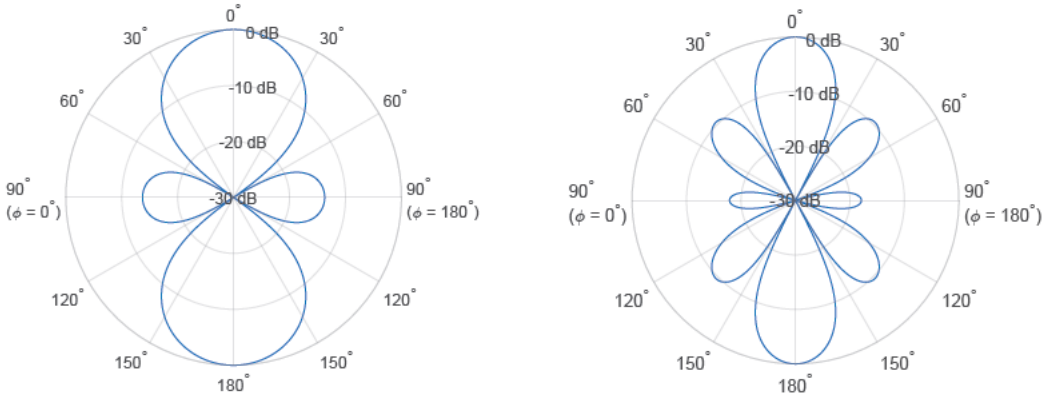

(a) d = $0,4\lambda_0$ (b) d = $0,7\lambda_0$

Figure 4.25: Pattern of the normalized array factor for $d = 0,4\lambda_0$ and $d = 0,7\lambda_0$ ($N = 3$, $\theta_0 = 0\,°$)

From the figure it is apparent that the maximum relative sidelobe level of the array factor increases for greater spacings. This has to be considered in the array design.

4.5.2 Simulation of the linear array

As defined in section 3.5 an E-plane array must be designed. The layout of the array is shown in figure 4.26.

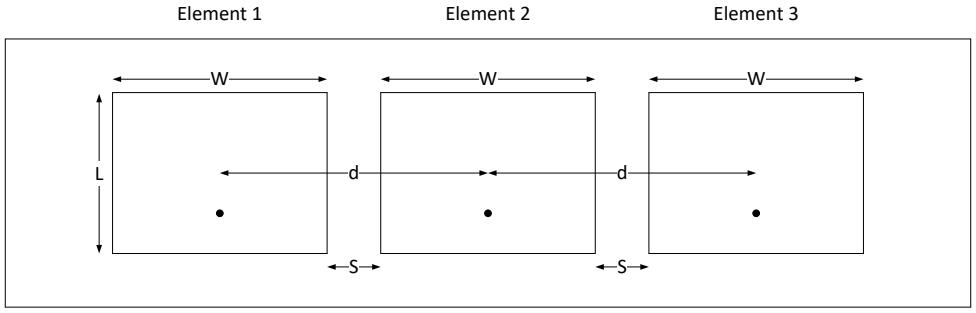

Figure 4.26: Layout of the linear three-element array

The footprint of the linear array is set to 130 mm x 40 mm and the position of the inset feed probe is marked with a black dot. Several spacings are simulated in *CST* to study the overall performance of the array. As the width W of the microstrip antenna equals $0,48\lambda_0$, a spacing of $d = 0,4\lambda_0$ cannot be realized. Therefore, the array is simulated for $d = 0,5\lambda_0$, $d = 0,6\lambda_0$ and $d = 0,7\lambda_0$.

The required progressive phase shift β is calculated for each spacing according to equation 2.33 and is listed in table 4.9.

Desired scan angle θ_0	**Progressive phase shift β**		
	$d = 0,5\lambda_0$	$d = 0,6\lambda_0$	$d = 0,7\lambda_0$
0 °	0 °	0 °	0 °
5 °	15,69 °	18,83 °	21,96 °
10 °	31,26 °	37,51 °	43,76 °
15 °	46,59 °	55,9 °	65,22 °
20 °	61,56 °	73,88 °	86,19 °
25 °	76,07 °	91,29 °	106,5 °
30 °	90 °	108 °	126 °
35 °	103,24 °	123,89 °	144,54 °

Table 4.9: Required progressive phase shift β and radiation direction θ_0 for the linear three-element array with the spacings $d = 0,5\lambda_0$, $d = 0,6\lambda_0$ and $d = 0,7\lambda_0$

For this setup, the beam of the linear array can be steered in the E-plane. As an example for the array in figure 4.26, the beam of the linear array with $d = 0,5\lambda_0$ can be steered toward $\theta_0 = 30\,°$ off broadside to the left side ($\phi_0 = 0\,°$) by exciting element 1 with a phase of 0 °, element 2 with a phase of 90 ° and element 3 with a phase of 180 °. Thus, from element to element the progressive phase shift equals 90 °. To steer the beam toward $\theta_0 = 30\,°$ off broadside to the right side ($\phi_0 = 180\,°$) one can change the phases of element 1 and element 3. In this way element 1 is excited with a phase of 180 °, element 2 is excited with a phase of 90 ° and element 3 is excited with a phase of 0 °. Thus, from element to element the progressive phase shift equals $-90\,°$.

The progressive phase shift enables to direct the maximum of the beam to any direction. In this thesis, this direction is termed as desired scan angle. As described in section 3.5 the real scan angle of an antenna, which is termed achieved scan angle in this thesis and indicates maximum radiation, can vary from the desired scan angle.

The following figures of merit are shown for the desired scan angles from 0 ° to 35 ° off broadside. As the simulation results are almost identical for $\phi_0 = 0\,°$ and $\phi_0 = 180\,°$ due to symmetry, only the steering toward $\phi_0 = 0\,°$ is shown.

The directivity and the realized gain of the linear arrays over the desired scan angle are displayed in figure 4.27.

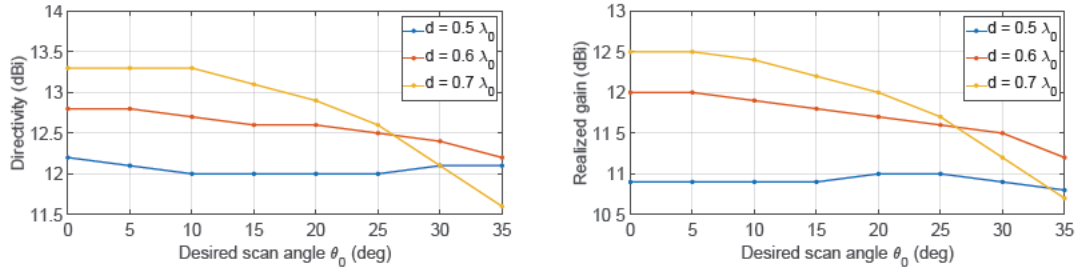

(a) Directivity (b) Realized gain

Figure 4.27: Directivity and realized gain of the simulated linear three-element array for $d = 0,5\lambda_0$, $d = 0,6\lambda_0$ and $d = 0,7\lambda_0$

The figure shows the decrease of the directivity and realized gain for wider scan angles off broadside. The curves of directivity and realized gain are similar for each spacing, respectively. As explained in section 2.4.2 the directivity increases with the array size. The array with d $= 0,7\lambda_0$ is larger than the others due to the greater spacing. Therefore, the directivity of this array is greater, too. Furthermore, one can see that the directivity and the realized gain of the array with $d = 0,5\lambda_0$ are almost constant over angles from $0\,°$ to $30\,°$ off broadside.

The relative sidelobe levels of the linear arrays are shown in figure 4.28 for each scan angle.

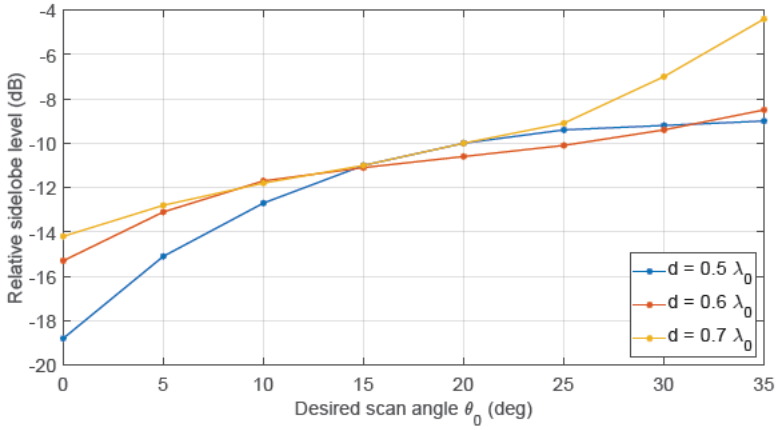

Figure 4.28: Relative sidelobe level of the simulated linear three-element array for $d = 0,5\lambda_0$, $d = 0,6\lambda_0$ and $d = 0,7\lambda_0$

From the figure it is apparent that the relative sidelobe level of the arrays is below $-10\,\mathrm{dB}$ for scan angles up to $20\,°$. Especially, for $\theta_0 = 0\,°$ and $\theta_0 = 5\,°$ the relative sidelobe level of the array with $\mathrm{d} = 0,5\lambda_0$ is less than the sidelobe level of the other spacings. This can be explained with the pattern of the array factor, which solely exhibits sidelobes at $\theta = 90\,°$ (see figure 3.1). On the contrary, the array factor of $d = 0,7\lambda_0$ has sidelobes at $\theta \approx 45\,°$, which causes sidelobes of the array in this direction. This is shown in figure 4.29, where the broadside patterns of the linear array for $0,5\lambda_0$ and $d = 0,7\lambda_0$ are displayed.

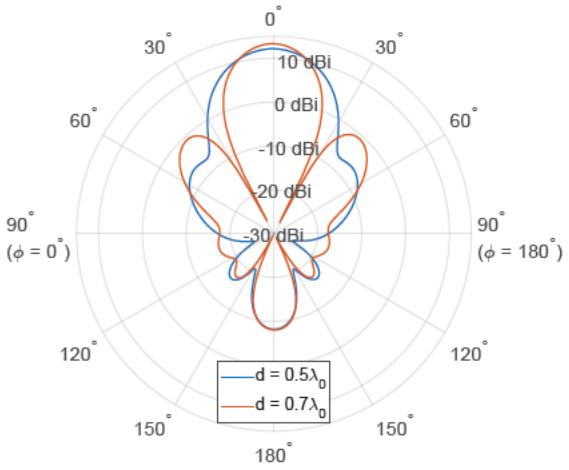

Figure 4.29: E-plane pattern with $\theta_0 = 0\,°$ of the simulated linear three-element array for $d = 0,5\lambda_0$ and $d = 0,7\lambda_0$

To minimize the sidelobes, the spacing d is chosen to $0,5\lambda_0$. However, one can still improve the array by slightly reducing the width of the patches. In this way the edge-to-edge distance S can be increased.

The mutual coupling of two adjacent patches is shown in figure 4.30 for elements with $W = 25{,}7\,\text{mm}$, $W = 24{,}7\,\text{mm}$, $W = 24\,\text{mm}$ and $W = 23{,}5\,\text{mm}$.

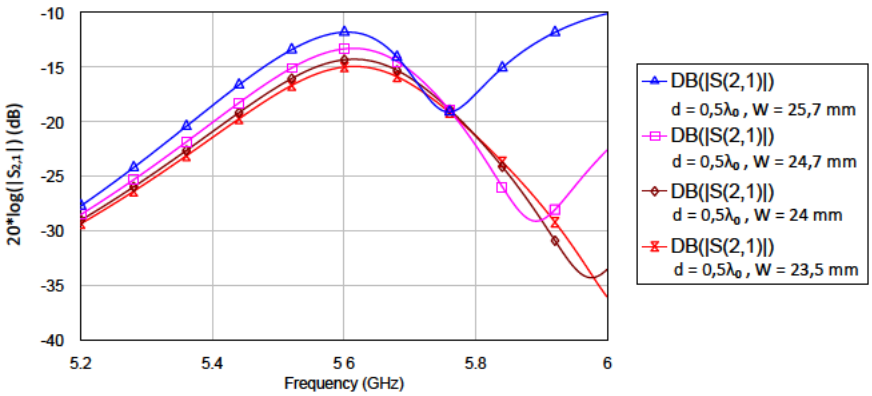

Figure 4.30: Mutual coupling $|S_{2,1}|$ of the simulated linear three-element array for $W = 25{,}7\,\text{mm}$, $W = 24{,}7\,\text{mm}$, $W = 24\,\text{mm}$ and $W = 23{,}5\,\text{mm}$ ($d = 0{,}5\lambda_0$)

Figure 4.30 shows that the mutual coupling slightly decreases with smaller widths, which means that the edge-to-edge distance S increases. The mutual coupling is $-11{,}86\,\text{dB}$ for $W = 25{,}7\,\text{mm}$ and $-15\,\text{dB}$ for $W = 23{,}5\,\text{mm}$ at $5{,}6\,\text{GHz}$. The decrease of the mutual coupling slightly reduces the sidelobe level. The corresponding relative sidelobe levels over the desired scan angle are displayed in figure 4.31 for the different widths.

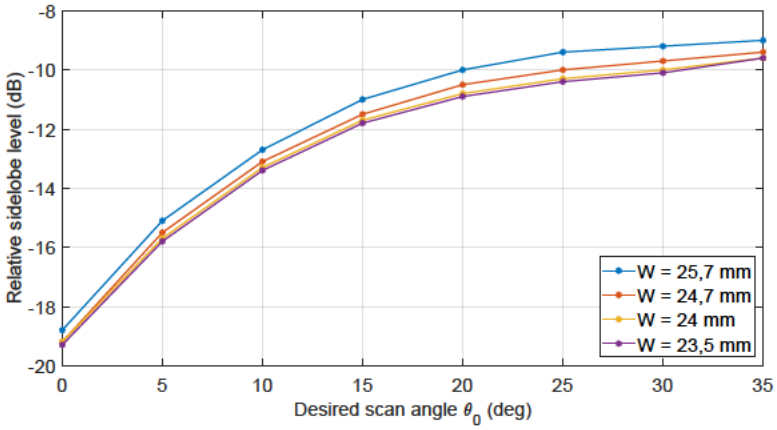

Figure 4.31: Relative sidelobe level of the simulated linear three-element array for $W = 25{,}7\,\text{mm}$, $W = 24{,}7\,\text{mm}$, $W = 24\,\text{mm}$ and $W = 23{,}5\,\text{mm}$ ($d = 0{,}5\lambda_0$)

The shortening of the width by 1 mm slightly improves the sidelobe performance. For greater changes the effects on the sidelobe level are marginal. For this reason, the width of the patches is set to 24,7 mm. In order not to change the resonant frequency, greater shortenings might become self-defeating. Furthermore, the realized gain of the antenna is increased due to the reduced mutual coupling. The realized gain is at least 11 dBi for scan angles up to 35 ° off broadside.

The presented considerations of the edge-to-edge spacing S and especially the center-to-center spacing d are marginal for the low number of elements and the uniform excitation. For nonuniform arrays with more elements the impact of the spacing significantly increases. As an example, there is a nonuniform linear six-element array in the electronic appendix A.16.

To conclude, the simulation results for the chosen design with $W = 24{,}7\,\text{mm}$ and $d = 0,5\lambda_0$ are shown in the following. For reasons of clarity, only the radiation patterns toward the desired directions $\theta_0 = 0\,°$, $\theta_0 = 10\,°$ and $\theta_0 = 20\,°$ are presented. More patterns can be obtained from section 5.6 and appendix F, where the measured and simulated patterns are compared, and the electronic appendix A.11. The H-plane pattern is solely shown for broadside radiation, as the beam is steered in the E-plane. The patterns are shown in polar and Cartesian form. To illustrate the sidelobe levels, the patterns in Cartesian form are normalized. The minimum of the polar patterns is set to $-30\,\text{dBi}$ for comparison reasons.

The polar and Cartesian form of the E-plane pattern for desired radiation toward $\theta_0 = 0\,°$ are shown in figure 4.32.

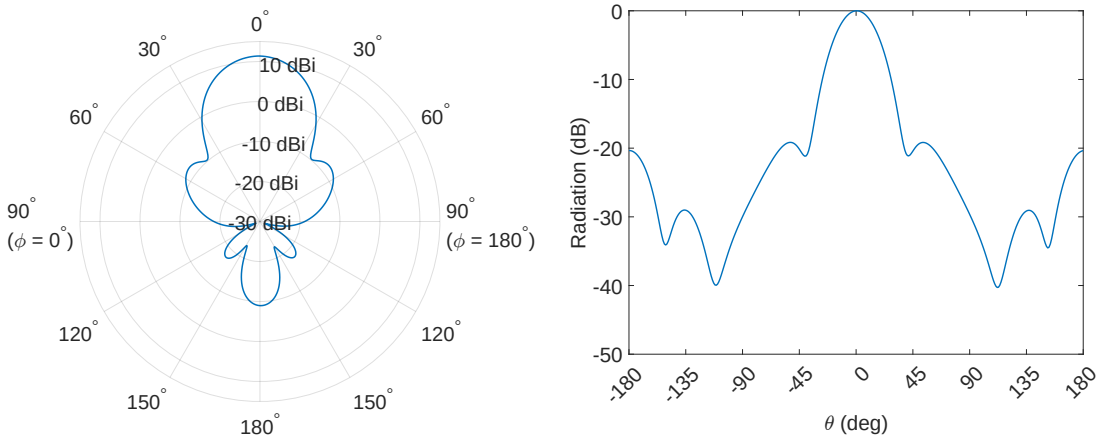

(a) Polar (b) Cartesian

Figure 4.32: E-plane patterns of the simulated linear three-element array for desired radiation toward $\theta_0 = 0\,°$ ($L = 13{,}3\,\text{mm}$, $W = 24{,}7\,\text{mm}$ and $d = 0{,}5\lambda_0$)

The polar and Cartesian form of the H-plane pattern for desired radiation toward $\theta_0 = 0\,°$ are shown in figure 4.33.

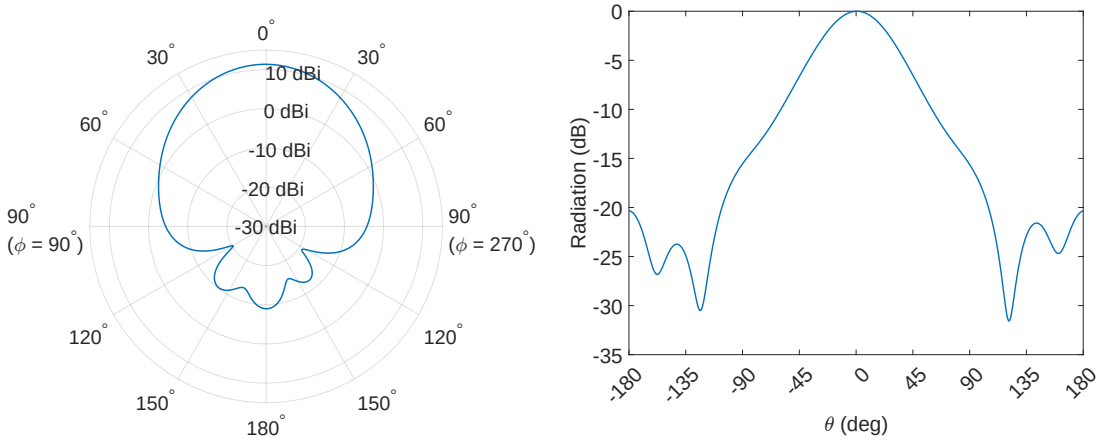

(a) Polar (b) Cartesian

Figure 4.33: H-plane patterns of the simulated linear three-element array for desired radiation toward $\theta_0 = 0\,°$ ($L = 13{,}3\,\text{mm}$, $W = 24{,}7\,\text{mm}$ and $d = 0{,}5\lambda_0$)

The polar and Cartesian form of the E-plane pattern for desired radiation toward $\theta_0 = 10\,°$ is shown in figure 4.34.

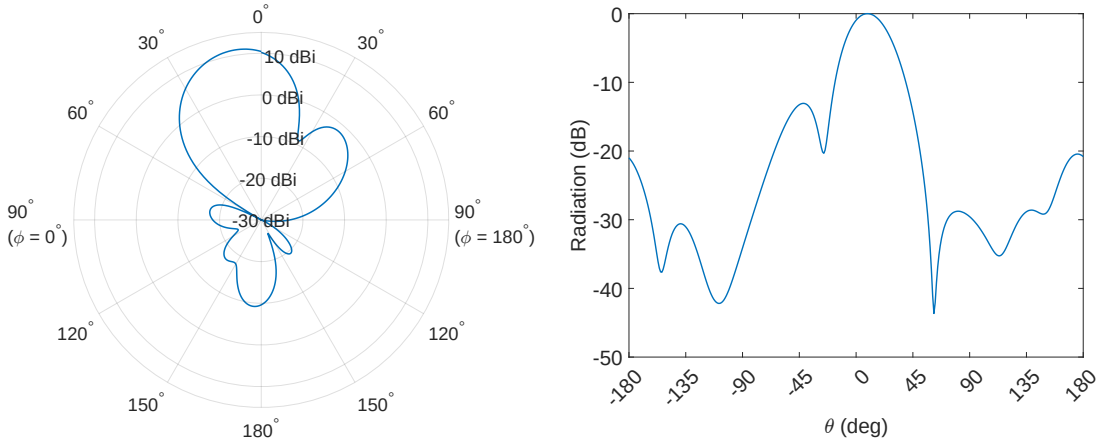

(a) Polar (b) Cartesian

Figure 4.34: E-plane patterns of the simulated linear three-element array for desired radiation toward $\theta_0 = 10\,°$ ($L = 13{,}3\,\text{mm}$, $W = 24{,}7\,\text{mm}$ and $d = 0,5\lambda_0$)

The polar and Cartesian form of the E-plane pattern for desired radiation toward $\theta_0 = 20\,°$ is shown in figure 4.35.

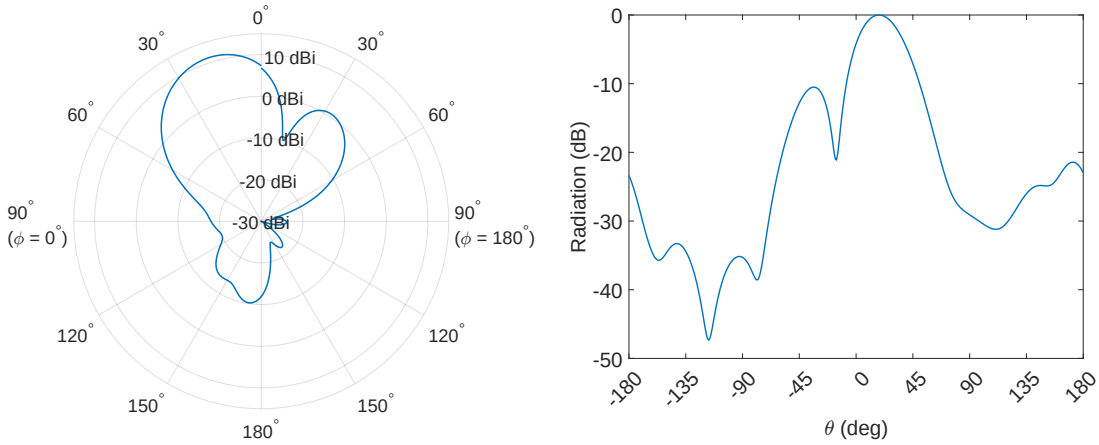

(a) Polar (b) Cartesian

Figure 4.35: E-plane patterns of the simulated linear three-element array for desired radiation toward $\theta_0 = 20\,°$ ($L = 13{,}3\,\text{mm}$, $W = 24{,}7\,\text{mm}$ and $d = 0,5\lambda_0$)

The figures show the patterns for the desired radiation, which is adjusted by the progressive phase shift. As explained in section 3.5 the adjustment of the desired radiation is not precise for the three-element antenna. Therefore, the desired and the achieved scan angle are compared in table 4.10. From the patterns above one can see that the sidelobe level increases for wider scan angles. As defined in section 3.5 the required relative sidelobe level is minimum $-10\,\mathrm{dB}$. This level is achieved at $\theta_0 = 22\,^\circ$. Thus, according to the requirements the maximum scan angle off broadside is $\theta_0 = 22\,^\circ$. Additionally, the directivity and realized gain for each achieved scan angle in the E-plane are listed in table 4.10. The desired scan angles in this table correspond to those listed in table 4.9.

Desired scan angle θ_0	**Achieved scan angle θ_0**	**Directivity**	**Realized gain**	**Relative sidelobe level**
$0\,^\circ$	$0\,^\circ$	12,2 dBi	11,37 dBi	−19,16 dB
$5\,^\circ$	$4\,^\circ$	12,2 dBi	11,34 dBi	−15,5 dB
$10\,^\circ$	$9\,^\circ$	12,1 dBi	11,27 dBi	−13,06 dB
$15\,^\circ$	$13\,^\circ$	12 dBi	11,23 dBi	−11,47 dB
$20\,^\circ$	$18\,^\circ$	12 dBi	11,22 dBi	−10,5 dB
$25\,^\circ$	$22\,^\circ$	12,1 dBi	11,22 dBi	−10,1 dB
$30\,^\circ$	$25\,^\circ$	12,1 dBi	11,16 dBi	−9,74 dB
$35\,^\circ$	$28\,^\circ$	12,2 dBi	11,01 dBi	−9,4 dB

Table 4.10: Comparison of the desired and achieved scan angle of the simulated linear three-element array

From the table one can see that the performance of the array is limited by the sidelobe level. The sidelobe level significantly increases for wider angles off broadside. The variation in directivity and realized gain is maximum 0,36 dB. Methods to improve the performance of the array are briefly described in section 6.2.

Due to the steering in the E-plane, the major lobe in the H-plane decreases. For broadside radiation the relative sidelobe level in the H-plane is about −20,3 dB. For scan angles off broadside, the sidelobe level relative to isotropic decreases in the H-plane.

The far-field of the linear array for broadside radiation is shown in figure 4.36.

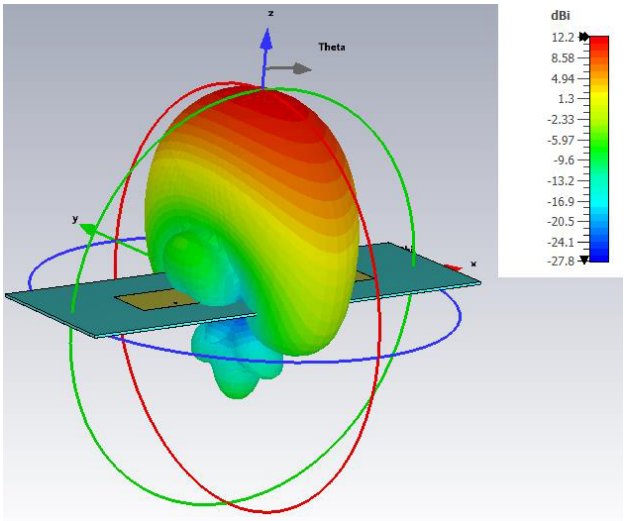

Figure 4.36: Far-field of the linear three-element array for broadside radiation

From the figure one can see the sidelobes in the E-plane at approximately 45 °. The H-plane solely exhibits sidelobes to the bottom side of the array. The angular width is wider in the H-plane than in the E-plane due to the the assembly in the E-plane.

The overall antenna performance is compared to the requirements in table 4.11.

Parameter	**Required**	**Simulated**	**Satisfied**
Scan angle θ_0	$> \pm 20\,°$	$\pm 22\,°$	✓
Relative side lobe level (E-plane)	$< -10\,\text{dB}$	$-10{,}1\,\text{dB}$	✓
Relative side lobe level (H-plane)	$< -10\,\text{dB}$	$-20{,}3\,\text{dB}$	✓
Directivity	$> 11{,}5\,\text{dBi}$	$12\,\text{dBi}$	✓
Realized gain	$> 10\,\text{dBi}$	$11{,}01\,\text{dBi}$	✓
Realized gain variation	$< 1\,\text{dB}$	$0{,}36\,\text{dB}$	✓
Mutual coupling	$< -10\,\text{dB}$	$-13{,}38\,\text{dB}$	✓

Table 4.11: Comparison of the simulated and required parameters of the linear three-element array for scan angles up to 22 °

The information given in the table relate to the maximum scan range of ± 22 °. The simulated linear three-element array fulfills the requirements and is fabricated.

4.6 Planar array

Three linear arrays are placed next to each other, to form the planar 3x3 array. Each linear array equals that of the previous section. The layout of the planar array is displayed in figure 4.37.

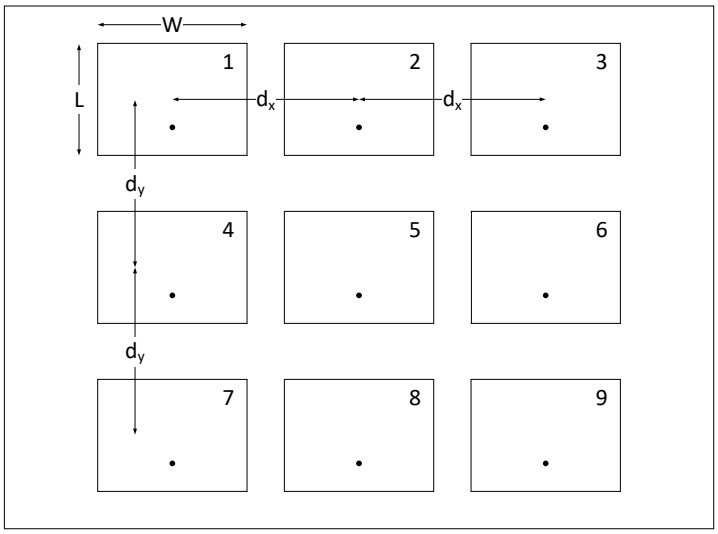

Figure 4.37: Layout of the planar 3x3 array

The spacing d_x is taken from section 4.5 and is set to $0,5\lambda_0$, whereas the spacing d_y has to be examined. As the length of one patch is 13,5 mm, which is about $0,25\lambda_0$, a spacing of $d_y = 0,4\lambda_0$ is possible in this direction. For the planar array, d_y spacings between $0,4\lambda_0$ to $0,6\lambda_0$ are simulated in *CST*.

The required progressive phase shifts β_x and β_y are calculated according to equations 2.45 and 2.46 for each spacing. The angle ϕ_0 equals $0\,^\circ$ or rather $180\,^\circ$ for scanning in E-plane and $90\,^\circ$ or rather $270\,^\circ$ for scanning in H-plane. An example for the beam steering is described in section 4.5.2. The given example applies for the planar array as well. Referring to figure 4.37 a progressive phase shift is applied in the x-direction of elements to scan the beam in the E-plane. To scan the beam in the H-plane a progressive phase shift is applied in the y-direction of elements. Moreover, for any other angle ϕ_0 a progressive phase shift in both directions is applied. For demonstration purpose there is an example for steering toward $\phi_0 = 135\,^\circ$ in the electronic appendix A.13.

The following figures of merit are shown for scan angles from 0 ° to 35 ° off broadside for the E-plane and for the H-plane. As the simulation results are almost identical for $\phi_0 = 0\,°$ and $\phi_0 = 180\,°$ due to symmetry, only the steering toward $\phi_0 = 0\,°$ is shown. The directivity and the realized gain of the planar arrays over the desired scan angle are displayed in figure 4.38 for the E-plane.

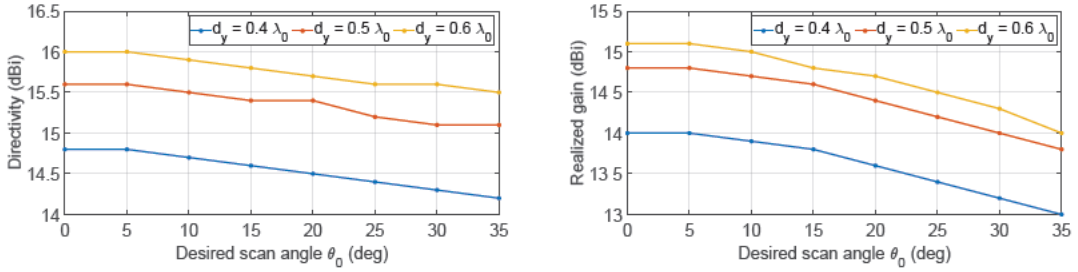

(a) Directivity (b) Realized gain

Figure 4.38: Directivity and realized gain of the simulated planar 3x3 array for $d_y = 0,4\lambda_0$, $d_y = 0,5\lambda_0$ and $d_y = 0,6\lambda_0$ in the E-plane ($d_x = 0,5\lambda_0$)

The directivity and the realized gain of the planar arrays over the desired scan angle are displayed in figure 4.39 for the H-plane.

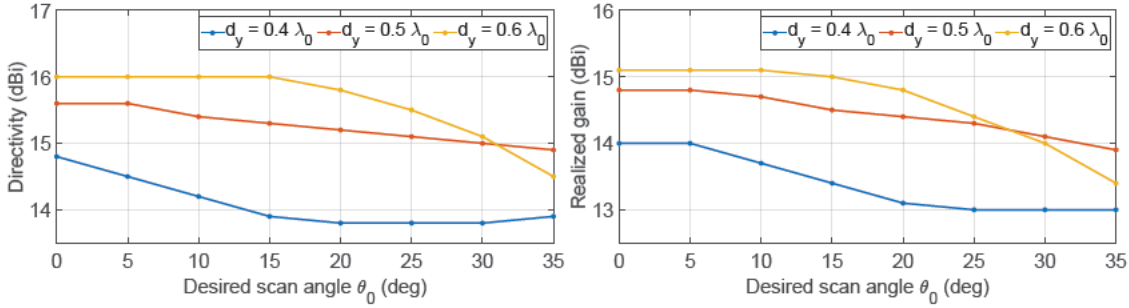

(a) Directivity (b) Realized gain

Figure 4.39: Directivity and realized gain of the simulated planar 3x3 array for $d_y = 0,4\lambda_0$, $d_y = 0,5\lambda_0$ and $d_y = 0,6\lambda_0$ in the H-plane ($d_x = 0,5\lambda_0$)

From the figures 4.38 and 4.39 it is apparent that the directivity and the realized gain of the planar array are greater than those of the linear array. In the E-plane the directivity and the realized gain fall faster for wider angles off broadside than in the E-plane. Variations from E-plane to H-plane can be explained with differences in the corresponding shape of the individual element. The variation of the parameters for $d = 0,5\lambda_0$ is smaller than for $d = 0,4\lambda_0$ and $d = 0,6\lambda_0$. For scan angles greater than $\theta_0 = 10\,°$ the directivity of the array with $d = 0,4\lambda_0$ falls below 14,5 dBi, which is the required value for the design.

The relative sidelobe levels over the desired scan angle of the arrays are shown in figure 4.40 for the E-plane and H-plane.

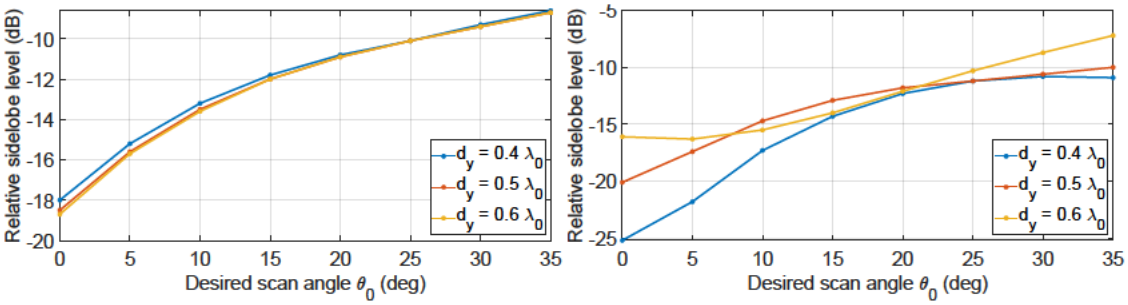

(a) E-plane (b) H-plane

Figure 4.40: Relative sidelobe level of the simulated 3x3 array for for $d_y = 0,4\lambda_0$, $d_y = 0,5\lambda_0$ and $d_y = 0,6\lambda_0$ ($d_x = 0,5\lambda_0$)

Comparing the relative sidelobe level from the planar array in the E-plane (see figure 4.40a) with those of the linear array (see figure 4.31) reveals not much difference for different d_y. In the H-plane the relative sidelobe levels for $\theta_0 < 10\,°$ are significantly better. For wider angles the curves are similar. Overall, the relative sidelobe level is below $-10\,\mathrm{dB}$ for desired scan angles up to $25\,°$ in E- and H-plane.

The mutual coupling is displayed in figure 4.41 for two adjacent elements of the planar array in the E-plane and in figure 4.42 for two adjacent elements in the H-plane.

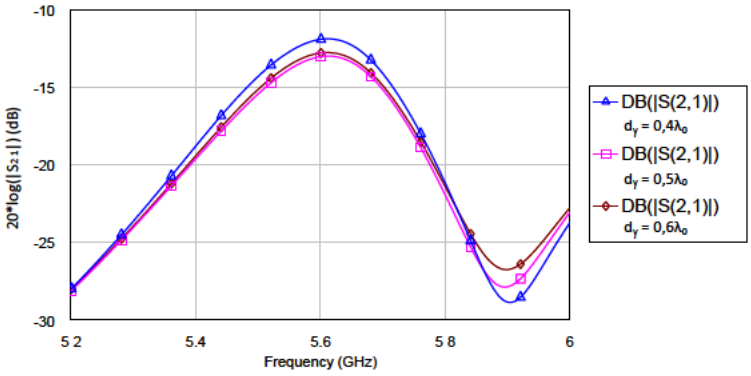

Figure 4.41: Mutual coupling for adjacent elements of the planar 3x3 array in the E-plane

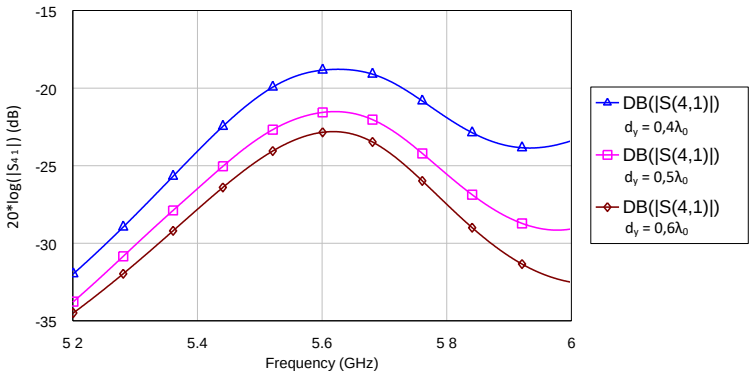

Figure 4.42: Mutual coupling for adjacent elements of the planar 3x3 array in the H-plane

From figure 4.41 one can see that the spacing d_y affects the E-plane coupling minimal. For all d_y the coupling is below $-10\,\mathrm{dB}$. In contrast, d_y affects the coupling in the H-plane. Figure 4.42 shows that the greatest spacing causes the lowest coupling. The coupling is $-18{,}84\,\mathrm{dB}$ for $d_y = 0,4\lambda_0$, which does not satisfy the defined requirement of maximum $-20\,\mathrm{dB}$.

The planar array is designed with $d_y = 0,5\lambda_0$. The realized gain and directivity of this spacing are greater than those of the array with $d_y = 0,4\lambda_0$. Differences in the relative sidelobe level and the coupling of the arrays with $d_y = 0,5\lambda_0$ and $d_y = 0,6\lambda_0$ are marginal. Furthermore, from the evaluation of the linear array in section 5.6 it is apparent that the measurement of the relative sidelobe level suffers from the measurement setup. Thus, for this setup one can assume that the impact of such small spacings on the relative sidelobe level is difficult to measure. The decision for $d_y = 0,5\lambda_0$ extremely minimizes the measurement effort for the planar array. Due to identical spacings in x-direction and y-direction, the corresponding required progressive phase shifts are identical for scanning in E- and H-plane. Thus, the adjustment of the phase shifters is temporally reduced. As the measurement of one radiation characteristic takes about one and a half hour, the handling of the overall demonstrator is facilitated.

To conclude, the simulation results for the chosen design with $d_y = 0,5\lambda_0$ are shown in the following. For reasons of clarity, only a selection of the simulated radiation patterns is shown. More simulated patterns can be obtained from section 5.7 and appendix G, where the simulated and measured patterns of the planar array are compared. Fur-

thermore, the simulated patterns can be viewed in the electronic appendix in section A.13. An overview of the achieved parameters is listed in table 4.12 for scanning in the E-plane and in table 4.13 for scanning in the H-plane.

The E-plane patterns for $\theta_0 = 0\,°$ are displayed in figure 4.43 in polar and Cartesian form.

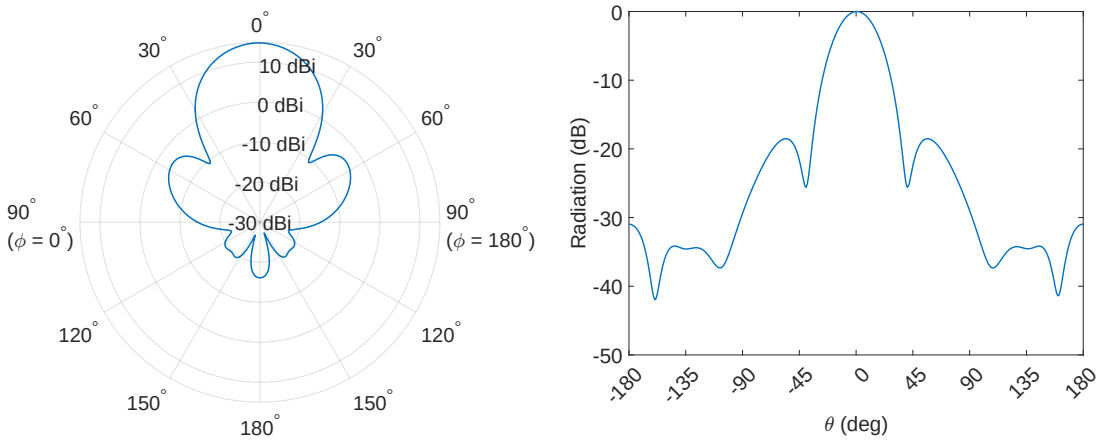

(a) Polar (b) Cartesian

Figure 4.43: E-plane patterns of the simulated planar 3x3 array for desired radiation toward $\theta_0 = 0\,°$ ($L = 13{,}3\,\text{mm}$, $W = 24{,}7\,\text{mm}$, $d_x = d_y = 0,5\lambda_0$)

Figure 4.44 shows the H-plane patterns for $\theta_0 = 0\,°$ in polar and Cartesian form.

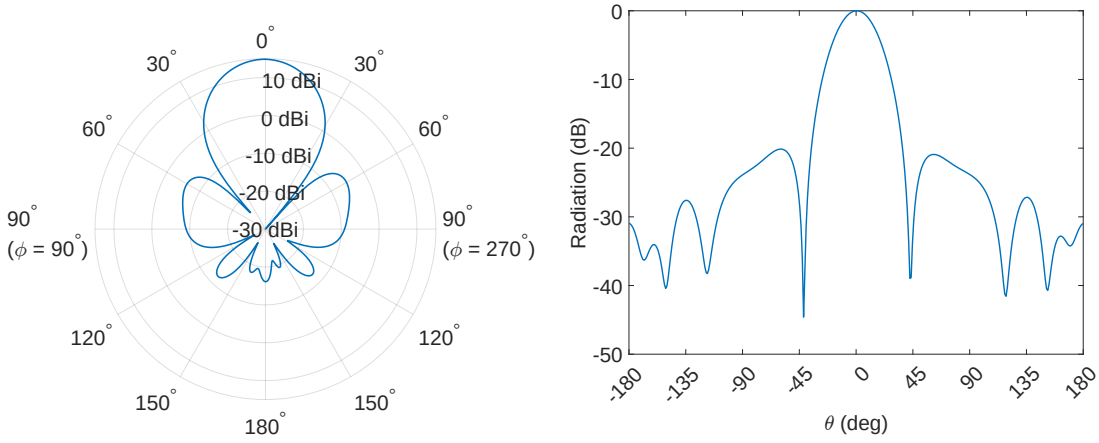

(a) Polar (b) Cartesian

Figure 4.44: H-plane patterns of the simulated planar 3x3 array for desired radiation toward $\theta_0 = 0\,°$ ($L = 13{,}3\,\text{mm}$, $W = 24{,}7\,\text{mm}$, $d_x = d_y = 0,5\lambda_0$)

From the figures one can see that both patterns have their maximum at $\theta_0 = 0\,^\circ$ with a realized gain of 14,83 dBi. The relative sidelobe level in the E-plane is slightly greater than in the H-plane.

Here only one radiation pattern for a scan in the E-plane is displayed, as a scan in the E-plane is already shown for the linear array in section 4.5. The E-plane patterns for $\theta_0 = 25\,^\circ$ are displayed in figure 4.45 in polar and Cartesian form.

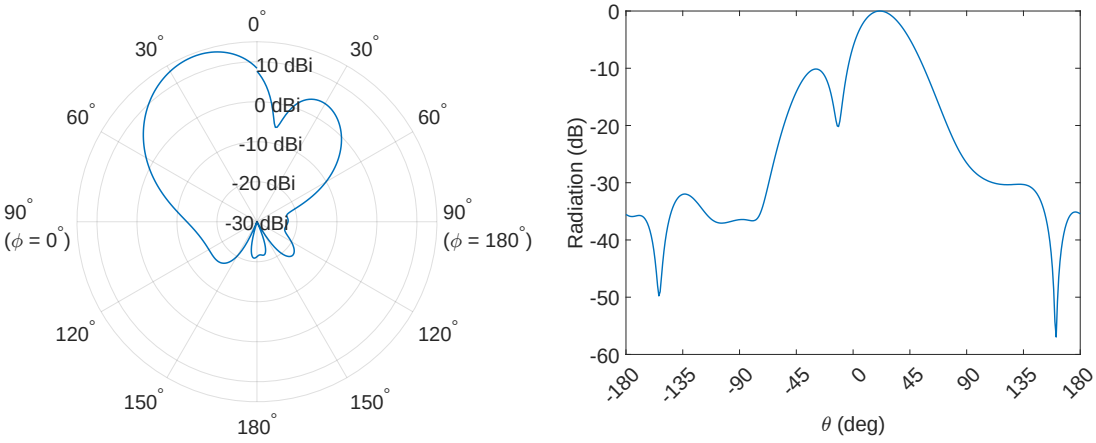

(a) Polar (b) Cartesian

Figure 4.45: E-plane patterns of the simulated planar 3x3 array for desired radiation toward $\theta_0 = 25\,^\circ$ ($L = 13{,}3\,\text{mm}$, $W = 24{,}7\,\text{mm}$, $d_x = d_y = 0,5\lambda_0$)

The achieved scan angle is $\theta_0 = 21\,^\circ$ and equals the maximum scan angle for this setup in the E-plane. As the relative sidelobe level of this measurement is about $-10{,}13\,\text{dB}$, this scan angle fulfills the requirements defined in section 3.6. The relative sidelobe level of wider scan angles is greater than $-10\,\text{dB}$. For this scan angle the realized gain is 14,23 dBi. Thus, the realized gain variation in the E-plane is 0,6 dBi for the achieved scan range.

The H-plane patterns for desired radiation toward $\theta_0 = 15\,°$ are shown in figure 4.46 in polar and Cartesian form.

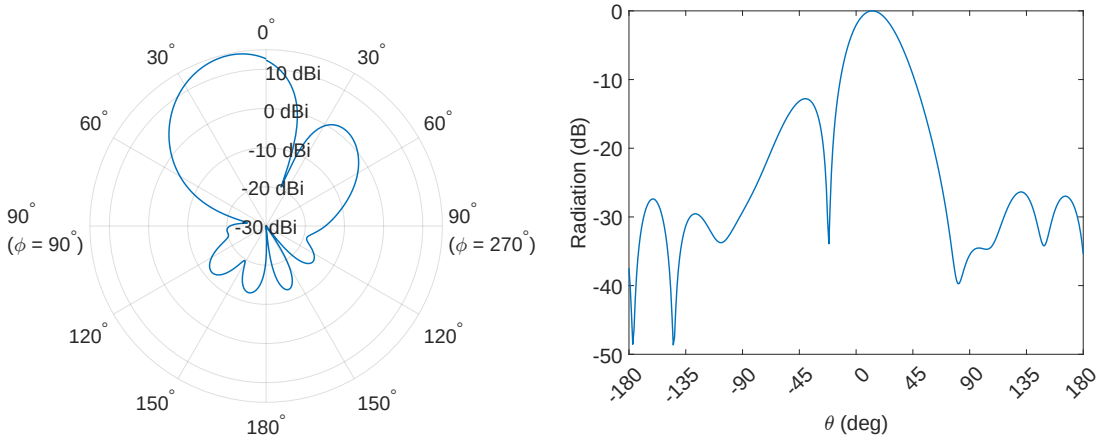

(a) Polar (b) Cartesian

Figure 4.46: H-plane patterns of the simulated planar 3x3 array for desired radiation toward $\theta_0 = 15\,°$ ($L = 13{,}3\,\text{mm}$, $W = 24{,}7\,\text{mm}$, $d_x = d_y = 0,5\lambda_0$)

Figure 4.47 displays the H-plane patterns for desired radiation toward $\theta_0 = 30\,°$ in polar and Cartesian form.

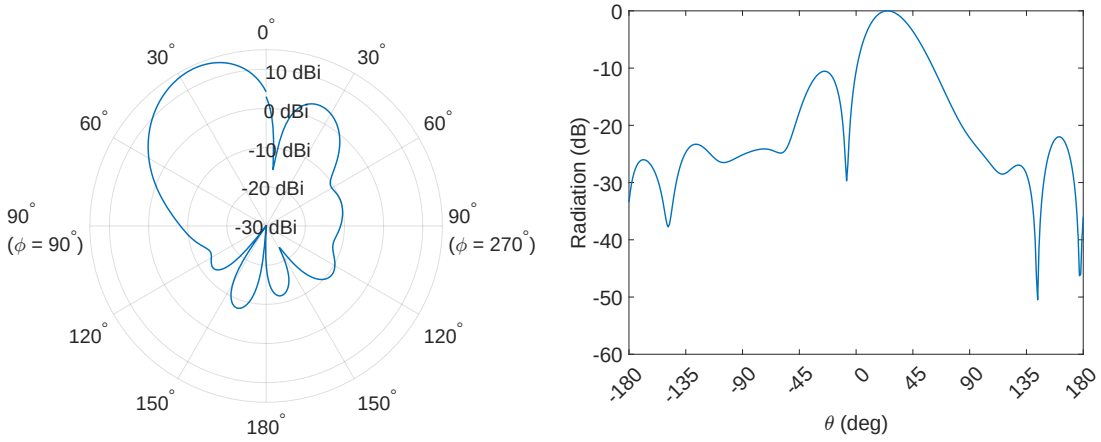

(a) Polar (b) Cartesian

Figure 4.47: H-plane patterns of the simulated planar 3x3 array for desired radiation toward $\theta_0 = 30\,°$ ($L = 13{,}3\,\text{mm}$, $W = 24{,}7\,\text{mm}$, $d_x = d_y = 0,5\lambda_0$)

From the figures 4.46 and 4.47 one can clearly see the increase of the relative sidelobe level for the wider angle. In figure 4.46a a scan angle of $12\,°$ is achieved and in figure 4.47 a scan angle of $25\,°$. For this setup $\theta_0 = 25\,°$ is the maximum scan angle as the relative

sidelobe level becomes greater than −10 dB for wider angles.

The overall performance of the planar array in the E-plane is listed in table 4.12.

Desired scan angle θ_0	**Achieved scan angle θ_0**	**Directivity**	**Realized gain**	**Relative sidelobe level**
0 °	0 °	15,6 dBi	14,83 dBi	−18,51 dB
5 °	4 °	15,6 dBi	14,8 dBi	−15,55 dB
10 °	8 °	15,5 dBi	14,71 dBi	−13,47 dB
15 °	13 °	15,4 dBi	14,57 dBi	−11,99 dB
20 °	17 °	15,3 dBi	14,41 dBi	−10,94 dB
25 °	21 °	15,2 dBi	14,23 dBi	−10,13 dB
30 °	25 °	15,1 dBi	14,02 dBi	−9,41 dB
35 °	28 °	15,1 dBi	13,78 dBi	−8,7 dB

Table 4.12: Comparison of the desired and achieved scan angle of the simulated planar 3x3 array in the E-plane

Table 4.13 shows the performance of the planar array in the H-plane.

Desired scan angle θ_0	**Achieved scan angle θ_0**	**Directivity**	**Realized gain**	**Relative sidelobe level**
0 °	0 °	15,6 dBi	14,83 dBi	−20,14 dB
5 °	4 °	15,6 dBi	14,8 dBi	−16,96 dB
10 °	8 °	15,5 dBi	14,69 dBi	−14,48 dB
15 °	12 °	15,4 dBi	14,57 dBi	−12,79 dB
20 °	17 °	15,3 dBi	14,45 dBi	−11,76 dB
25 °	21 °	15,2 dBi	14,35 dBi	−11,13 dB
30 °	25 °	15,1 dBi	14,21 dBi	−10,55 dB
35 °	28 °	15 dBi	14 dBi	−9,86 dB

Table 4.13: Comparison of the desired and achieved scan angle of the simulated planar 3x3 array in the H-plane

The maximum scan angle in the E-plane is 21 ° and the realized gain variation is 0,6 dB. In the H-plane the maximum scan angle is 25 ° and the realized gain variation is 0,62 dB.

The far-field of the planar 3x3 array for broadside radiation is displayed in figure 4.48.

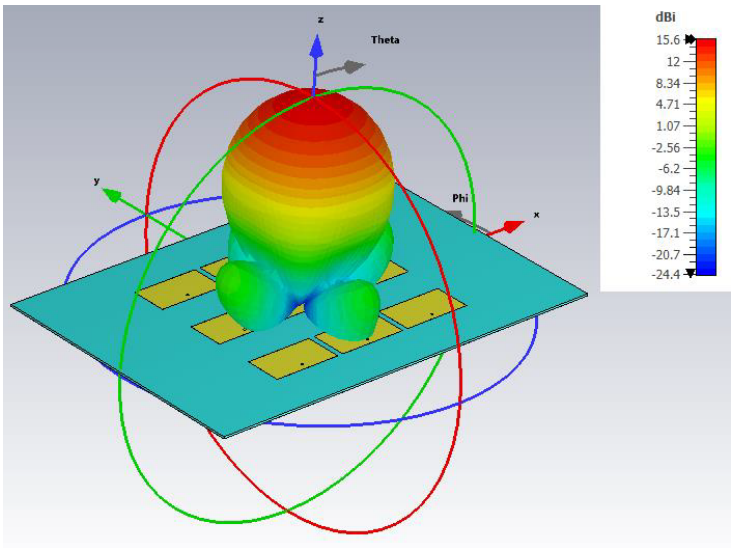

Figure 4.48: Far-field of the planar 3x3 array for broadside radiation

The far-field of the array is symmetrical due to the square assembly of elements. Slightly differences in E-plane and H-plane are due to the different pattern of the individual patch in both planes. The cuts in the figures above illustrate such differences.

The overall performance of the designed planar array is summarized in table 4.14.

Parameter	**Required**	**Simulated**	**Satisfied**
Scan angle θ_0	$> \pm 20\,^\circ$	$\pm 21\,^\circ$	✓
Relative side lobe level (E-plane)	$< -10\,\mathrm{dB}$	$-10{,}55\,\mathrm{dB}$	✓
Relative side lobe level (H-plane)	$< -10\,\mathrm{dB}$	$-10{,}1\,\mathrm{dB}$	✓
Directivity	$> 14{,}5\,\mathrm{dBi}$	$15{,}2\,\mathrm{dBi}$	✓
Realized gain	$> 13\,\mathrm{dBi}$	$14{,}21\,\mathrm{dBi}$	✓
Realized gain variation	$< 1\,\mathrm{dB}$	$0{,}62\,\mathrm{dB}$	✓
Mutual coupling in E-plane	$< -10\,\mathrm{dB}$	$-13{,}31\,\mathrm{dB}$	✓
Mutual coupling in H-plane	$< -20\,\mathrm{dB}$	$-21{,}57\,\mathrm{dB}$	✓

Table 4.14: Comparison of the simulated and required parameters of the planar 3x3 array for scan angles up to $22\,^\circ$

The simulated planar 3x3 array fulfills the requirements and is fabricated.

5 Evaluation of the phased array antenna demonstrator

The measurements and the analysis of the designed components are described in this section. Scattering parameters are measured using the *ZNB 20 Vector Network Analyzer*. The radiation of the antennas is measured using the *AL-4162-2MC*, which is an antenna measurement system from *ORBIT/FR*. To determine the realized gain, the known reference antenna *Quad Ridged Broadband Horn Antenna QRH11* is used for comparison. The procedure to determine the realized gain is described in appendix D. The used procedure is a *Gain-Comparison Measurement*. As the measurement setup is inaccurate, the gain measurement is an estimation.

5.1 Phase shifter

The measurement results of the phase shifter are analysed in the following. The measured values are compared to the defined requirements in section 3.1. In figure 5.1 the insertion loss and the return loss at 5,6 GHz are shown for control voltages from 0 V to 15 V.

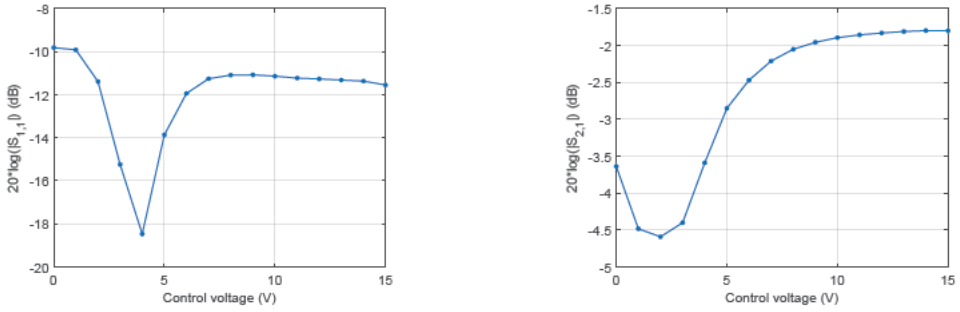

(a) Return loss

(b) Insertion loss

Figure 5.1: Measured performance of the phase shifter versus control voltage at 5,6 GHz

The measured return loss has a similar form to that simulated in figure 4.8a. However, due to losses and the real components the return loss is greater than in the simulation. For control voltages up to 1 V the return loss is slightly greater than −10 dB. Therefore, the requirement to the return loss is not satisfied. The insertion loss has a variation of 2,79 dB. This measurement reveals that the simulation is partially inaccurate as the simulated insertion loss variation is about 9,51 dB. This result confirms that the simulation suffers from the diode model and the parasitic elements.

The relative phase shift for control voltages from 0 V to 15 V is shown in figure 5.2.

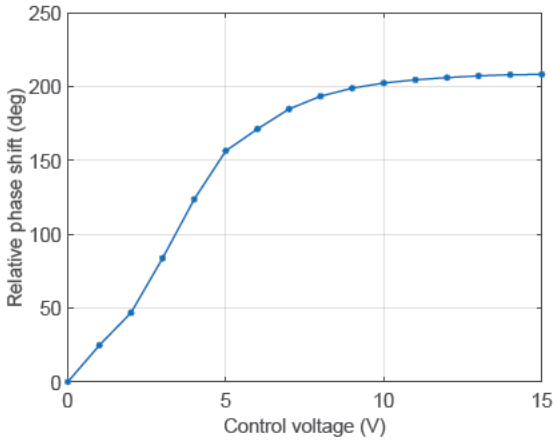

Figure 5.2: Measured relative phase shift of the phase shifter versus control voltage at 5,6 GHz

From the figure it is apparent that the requirement to the maximum relative phase shift is satisfied. The maximum relative phase shift is 212,7 °. Similar to the simulation the curve flattens for greater control voltages. This can be explained with the capacitance versus reverse voltage behaviour of the varactor diodes. As shown by the datasheet, the gradient of the capacitance change significantly decreases for reverse voltages greater than 6 V [9, p. 4].

The comparison of the measured parameters to the required values is shown in table 5.1.

Parameter	**Required**	**Min.**	**@ 5,6 GHz**	**Max.**	**Satisfied**
Bandwidth	$> 5\,\%$	-	-	-	×
Relative phase shift	$> 180\,^\circ$	-	$212{,}7\,^\circ$	-	✓
Insertion loss	$> -5\,\mathrm{dB}$	$-5{,}123\,\mathrm{dB}$	-	$-1{,}494\,\mathrm{dB}$	×
Return loss (In.)	$< -10\,\mathrm{dB}$	$-37{,}28\,\mathrm{dB}$	-	$-9{,}814\,\mathrm{dB}$	×
Insertion loss variation	$< 3\,\mathrm{dB}$	-	$2{,}79\,\mathrm{dB}$	-	✓

Table 5.1: Comparison of the measured and required parameters of the phase shifter for frequencies from 5,32 GHz to 5,88 GHz for control voltages from 0 V to 15 V

Overall, the fabricated phase shifter does not satisfy the defined requirements. However, the most important required parameters are fulfilled. The phase shifter enables a relative phase shift of about $212{,}7\,^\circ$ with an insertion loss variation less than 3 dB at 5,6 GHz. The requirement to the bandwidth is not fulfilled. Extended measurement results of the phase shifter for 5,32 GHz and 5,88 GHz are shown in appendix C.3. The relative phase shift at 5,32 GHz is solely about $170\,^\circ$ and the insertion loss at 5,88 GHz falls below -5 dB. The return loss at 5,6 GHz is slightly above -10 dB for low control voltages.

Nevertheless, this design is taken for the feednetwork module. Regarding the return loss, the deviation from the requirements is solely about 0,2 dB and regarding the insertion loss, the deviation is about 0,12 dB at 5,88 GHz. As enhancements of the phase shifter are challenging and the time of the thesis is limited, the deviations to the requirements are neglected. The performance of the phase shifter can be significantly improved by minimizing the influence of the parasitic elements of the diodes, which is shown in [5].

5.2 Wilkinson power divider

The measurement results of the two-way and the 16-way power divider are shown in the following. The results from the fabricated two-way divider are analysed and used to improve the design of the 16-way divider.

5.2.1 Two-way Wilkinson power divider

The return loss and the isolation over the frequency of the two-way divider are displayed in figure 5.3.

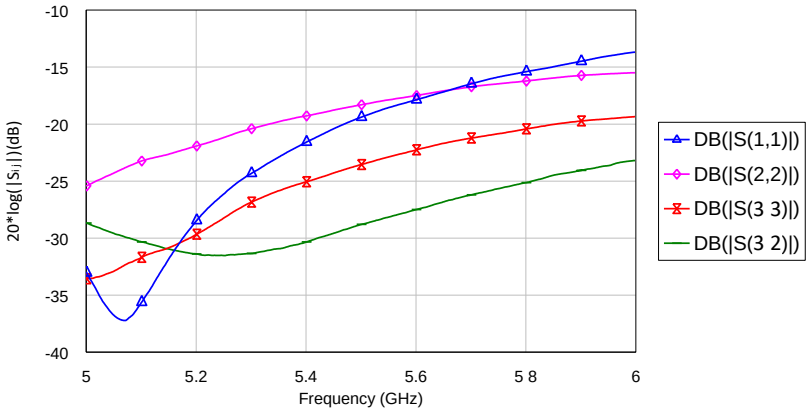

Figure 5.3: Measured return loss and isolation of the two-way Wilkinson power divider

From figure 5.3 it is apparent, that the center frequency is about 5,07 GHz. The return losses are below $-10\,\mathrm{dB}$ over the frequency and the isolation is below $-20\,\mathrm{dB}$. Referring to section 3.2.1 the requirements of the divider are fulfilled. Nevertheless, the performance can be enhanced through slightly reducing the length of the quarter-wavelength arms.

For this reason the length of l_2 (middle microstrip line of the quarter-wavelength arm, see section 4.2.1) can be decreased. Assuming a linear relation between center frequency and length of the microstrip line, the length l_2 should be set to

$$l_2 = 3,45\,\mathrm{mm} \cdot \frac{5,07\,\mathrm{GHz}}{5,6\,\mathrm{GHz}} \approx 3,15\,\mathrm{mm}. \tag{5.1}$$

Thus, to shift the center frequency toward 5,6 GHz the 16-way Wilkinson power divider is designed and fabricated with $l_2 = 3{,}15\,\text{mm}$.

In figure 5.4 the insertion loss and phase shift of the output ports are shown.

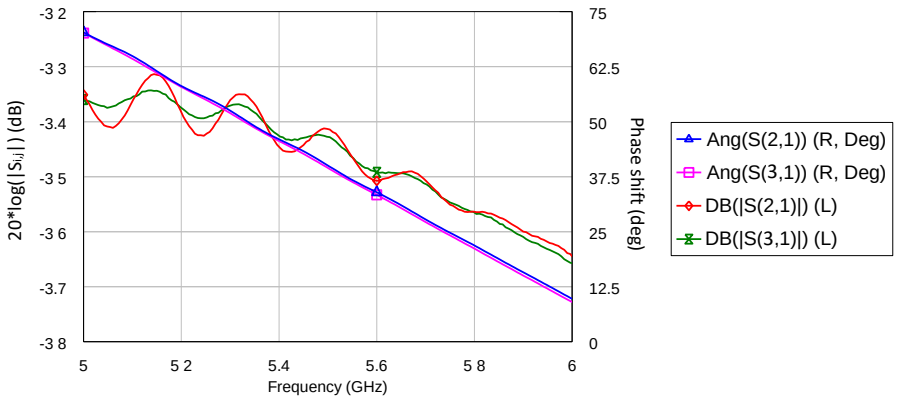

Figure 5.4: Measured magnitude and phase balance of the two-way Wilkinson power divider

Over the frequency range the insertion loss is at least $-3{,}66\,\text{dB}$. The maximum variation in the magnitudes is about $0{,}04\,\text{dB}$ and the maximum variation in the phases is about $0{,}75\,°$. Thus, the circuit is well balanced.

In table 5.2 the measured and required parameters of the divider are compared.

Parameter	**Required**	**Min**	**@ 5,6 GHz**	**Max**	**Satisfied**
Insertion loss	$> -4\,\text{dB}$	$-3{,}66\,\text{dB}$	-	$-3{,}31\,\text{dB}$	✓
Isolation	$< -15\,\text{dB}$	$-31{,}54\,\text{dB}$	$-27{,}5\,\text{dB}$	$-23{,}2\,\text{dB}$	✓
Return loss (Input)	$< -10\,\text{dB}$	$-37{,}23\,\text{dB}$	$-17{,}88\,\text{dB}$	$-13{,}68\,\text{dB}$	✓
Return loss (Output)	$< -10\,\text{dB}$	$-33{,}57\,\text{dB}$	-	$-15{,}49\,\text{dB}$	✓
Magnitude Balance	$< 0{,}5\,\text{dB}$	$0\,\text{dB}$	$0{,}02\,\text{dB}$	$0{,}04\,\text{dB}$	✓
Phase Balance	$< 15\,°$	$0{,}2\,°$	$0{,}57\,°$	$0{,}75\,°$	✓

Table 5.2: Comparison of the measured and required parameters of the two-way Wilkinson power divider

The two-way Wilkinson power divider possesses good performance over the frequency range from 5 GHz to 6 GHz. The significant observation of these measurements is to set

l_2 to 3,15 mm for even better performance. In this way, the 16-way divider is manufactured.

5.2.2 16-way Wilkinson power divider

The results of the measurements of the 16-way divider are evaluated in the following. The insertion loss of the divider is displayed in figure 5.5. To determine the magnitude balance, the insertion loss is shown for all output ports.

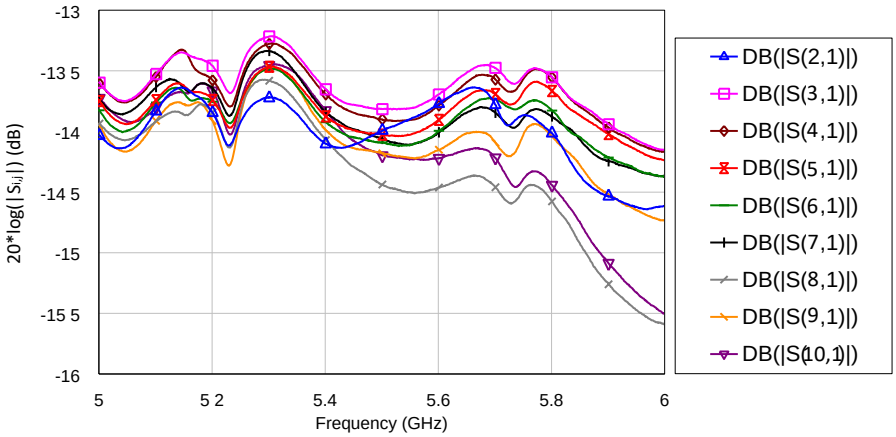

Figure 5.5: Measured insertion loss of the 16-way Wilkinson power divider

The traces have a similar progression up to 5,8 GHz and the insertion loss is in the range from −13,2 dB to −14,6 dB. The maximum magnitude variation in the range of 5 GHz to 5,8 GHz is 1 dB. However, for frequencies greater than 5,8 GHz $|S_{8,1}|$ and $|S_{10,1}|$ considerably decrease. For frequencies greater than 5,86 GHz $|S_{8,1}|$ is below −15 dB. At 6 GHz the maximum magnitude variation is approximately 1,4 dB. Due to the measurement setup, the coaxial cables connected to the outer ports require an angle between network analyzer and circuit board. Therefore, the connected cables cause the board to bend. It is observed that this circumstance degrades the performance of the divider. This is the reason why the performance of port 8 and 10 is worse than the performance of the other output ports.

The return loss at port 1 is displayed in figure 5.6.

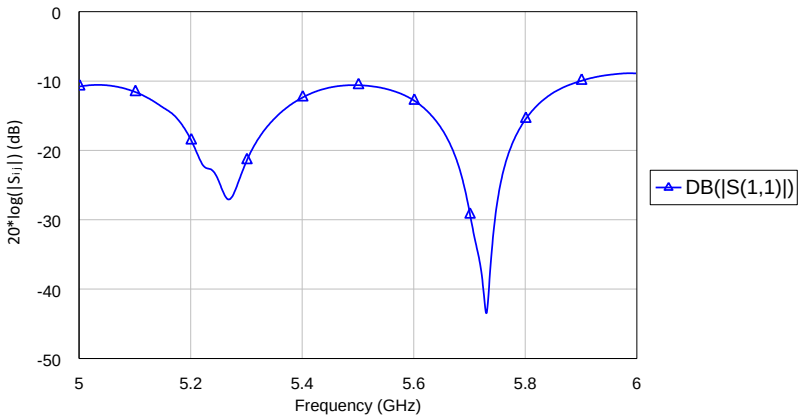

Figure 5.6: Measured return loss (input) of the 16-way Wilkinson power divider

One can see from the figure that $|S_{1,1}|$ is below $-10\,\mathrm{dB}$ for frequencies less than 5,9 GHz. At 5,73 GHz the return loss has its minimum and is $-43{,}49\,\mathrm{dB}$. Hence, the shortening of l_2 to shift the center frequency toward 5,6 GHz (see section 5.2.1) was successful. However, the length of 3,15 mm is slightly too short. At this point the improvement of the 16-way divider becomes filigree. Considering the fabricational tolerance of 0,2 mm no more effort is spent in shifting the center frequency to 5,6 GHz.

The return loss of the output ports is shown in figure 5.7.

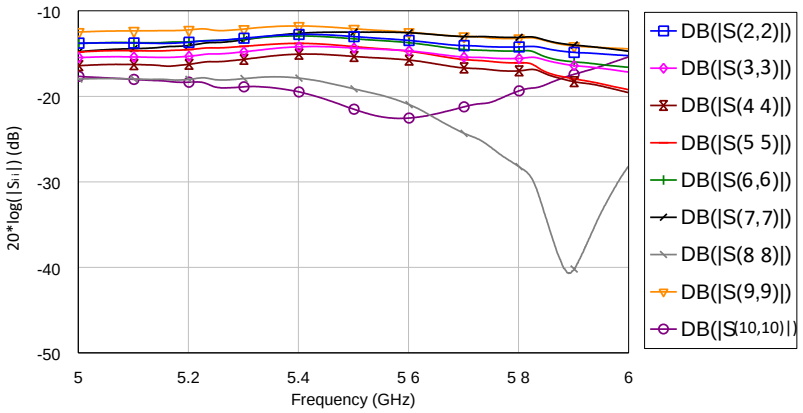

Figure 5.7: Measured return loss (output) of the 16-way Wilkinson power divider

For most output ports the return loss is between −10 dB and −20 dB. The dip of $|S_{8,8}|$ at 5,9 GHz is due to the above described circumstance. The deviation between the return loss of the individual ports can be explained with non identical connectors, solder joints and deviations in the width and length of the microstrip lines. Furthermore, deviations may occur due to a varying degree in tightened union nuts from the connectors. It is observed that angles in the coaxial cables cause the union nuts to loose.

In figure 5.8 the measured isolation of the divider is displayed. To limit the amount of displayed results, only the isolation from port 3 to all other output ports is shown. The isolation between other ports can be obtained from the electronic appendix A.6.

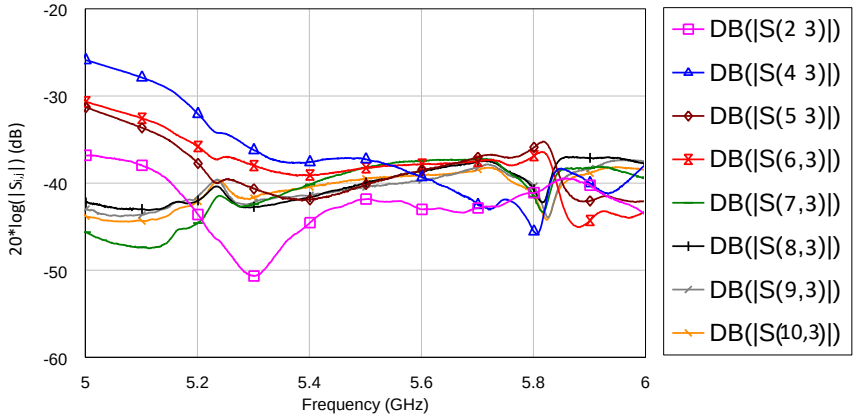

Figure 5.8: Measured isolation of the 16-way Wilkinson power divider from port 3 to all other output ports

From the figure it is apparent that the measured isolation is below −20 dB for frequencies in the range from 5 GHz to 6 GHz. In principle, deviations are caused by a different number of junctions between the ports and measurement inaccuracies. At 5,6 GHz the isolation is below −35 dB between port 3 and all other output ports.

The phase shift of port 3 and 8 in relation to port 1 is shown in figure 5.9. The measured traces of the other output ports are located between the displayed traces of port 3 and 8. For reasons of clarity, only the phase shift of port 3 and 8 are shown.

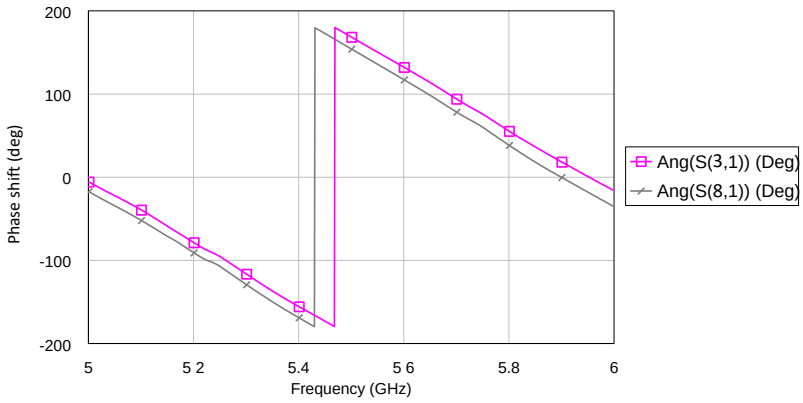

Figure 5.9: Measured phased shift of port 3 and 8 in relation to port 1 of the 16-way Wilkinson power divider

The phase balance between the output ports is maximum about 20 ° in the range from 5 GHz to 6 GHz. The phase deviation slightly increases with the frequency.

All measured values are summarized and compared to the requirements in table 5.3.

Parameter	**Required**	**Min**	**@ 5,6 GHz**	**Max**	**Satisfied**
Insertion loss	> -15 dB	$-15{,}59$ dB	-	$-13{,}22$ dB	×
Isolation	< -20 dB	$-50{,}69$ dB	-	$-25{,}87$ dB	✓
Return loss (Input)	< -10 dB	$-43{,}49$ dB	$-12{,}78$ dB	$-8{,}87$ dB	×
Return loss (Output)	< -10 dB	$-40{,}64$ dB	-	$-11{,}77$ dB	✓
Magnitude Balance	$< 1{,}5$ dB	0,44 dB	0,77 dB	1,44 dB	✓
Phase Balance	< 25 °	11,58 °	14,9 °	19,29 °	✓

Table 5.3: Comparison of the measured and required parameters of the 16-way Wilkinson power divider for frequencies from 5 GHz to 6 GHz

The fabricated divider does not satisfy the defined requirements over the frequency range from 5 GHz to 6 GHz. However, up to frequencies of 5,86 GHz the requirements are fulfilled. For this reason the divider is taken for the design of the feed network module.

5.3 Feed network module

The manufactured feed network module is displayed in figure 5.10. The top side and the bottom side of the module are shown in the figure.

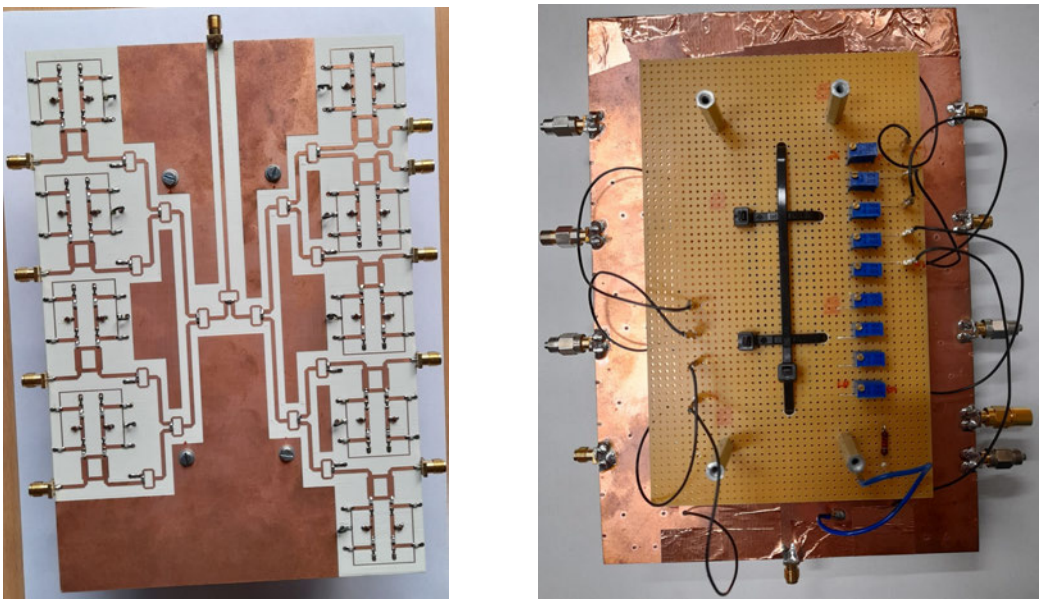

(a) Top side of the feed network module (b) Bottom side of the feed network module

Figure 5.10: Fabricated feed network module

The DC circuit of the module is implemented on a perfboard, which is mounted to the bottom side of the board. To minimize radiation, a ground plane is mounted on the top side of the module and the edges are covered with copper band. The ground plane on the top side is removed for the picture. For the antenna measurements the module can be attached below the antenna. Each junction in figure 5.10a equals a two-way Wilkinson power divider. One can see the phase shifters at the left and right side of the circuit board. Figure 5.10b shows the potentiometers for the phase tuning.

The requirements of the module are evaluated in table 5.4.

Parameter	**Required**	**Measured**	**Satisfied**
Weight	$< 1\,\text{kg}$	$0{,}42\,\text{kg}$	✓
Size	$< 30\,\text{cm}$ x $20\,\text{cm}$	$21\,\text{cm}$ x $15\,\text{cm}$	✓
DC supply	internal	-	✓
Radiation	$< -20\,\text{dB}$	$-20{,}79\,\text{dB}$	✓

Table 5.4: Comparison of the measured and required parameters of the feed network module

The electrical characteristic of the module is similar to that of the phase shifter. Due to the divider, the insertion loss undergoes an additional attenuation. The measurement results can be obtained from the electronic appendix A.8. Exemplary scattering parameters are shown in appendix E.1. The maximum radiation of the feed network module is attenuated by $-20{,}79\,\text{dB}$ relative to the maximum of a reference antenna. The corresponding measurement is shown in appendix E.2. Overall, the feed network module fulfills the defined requirements.

5.4 Measurement setup for the antenna radiation

The setup of the antenna measurement is described in this section. The setup is displayed in figure 5.11.

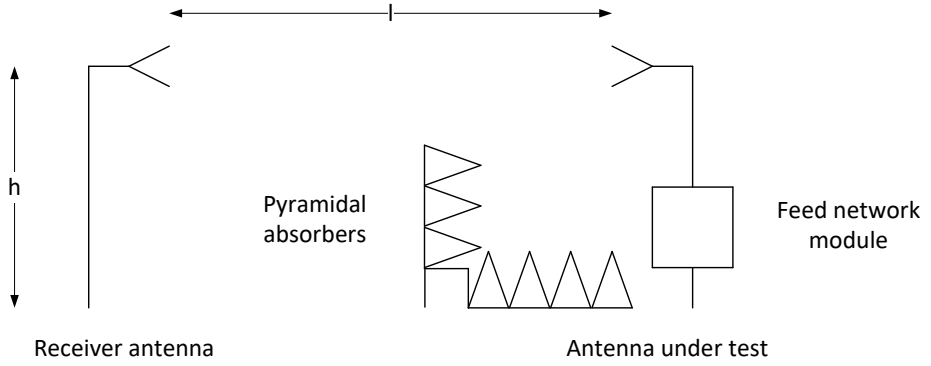

Figure 5.11: Measurement setup for the radiation characteristic

The shown setup is used for all measurements. A receiver antenna and the antenna under test are placed along a line separated by the distance l. The center of each antenna is adjusted to a height h. The antenna under test is placed on a rotating table and the feed network module is mounted on the bottom of the rotating table. To create equal conditions, every antenna is measured by inserting the feed network module between the antenna under test and network analyzer. Pyramidal absorbers are placed close to the rotating table to minimize radiation from the module. In this setup the antenna under test operates as transmitter.

The setup strongly affects the measurements due to several inaccuracies. The entire setup is adjusted by hand. This includes the height h, the distance l and the alignment along a line of the receiving and transmitting antenna. These circumstance especially influence the measurement accuracy of the adjusted scan angle θ_0. The impact on the realized gain has to be investigated in the future. However, it is observed that the identical antenna under test exhibits a high variation in realized gain for several test measurements.

The phase shifters of the feed network module are the elementary components to enable beam steering. Therefore, emphasis is placed on low errors in the adjustment of

the progressive phase shift. After the adjustment of the phase shifters, the module is attached to the rotating table and connected to the antenna under test. It is observed that cable flexing can cause phase errors of about 30 ° and magnitude errors of about 4 dB. It is tried to prevent cable flexing due to cable routing. Nevertheless, phase and magnitude errors due to cable flexing cannot be eliminated. Variations between measured values as well as deviations between simulation and measurement in realized gain and sidelobe levels can be explained with these errors to a certain degree.

Figure 5.12 shows the rotating table in the measuring chamber. The planar array is mounted at the top and the feed network module at the bottom.

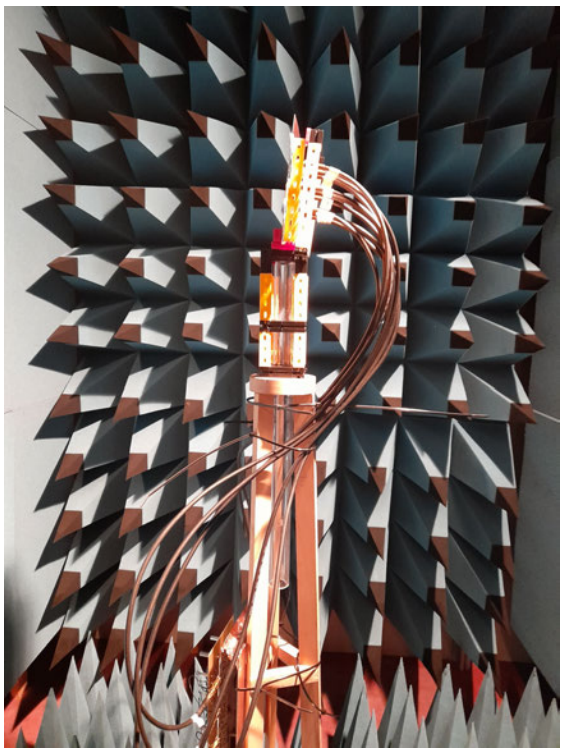

Figure 5.12: Antenna under test at the rotating table

From the figure one can see that the coaxial cables tend to pull the circuit board backwards. Therefore, the radiation is not straight and a flatness error is caused. The impact of this error has to be investigated in the future. Another error that is affected by the cables is the movement of the entire mount. It is observed that the cables slightly cause the mount to rotate, which can cause errors in the achieved scan angle.

5.5 Microstrip antenna

The designed microstrip antenna with a length of $L = 13{,}3\,\text{mm}$ is fabricated. As this antenna suffers from resonant frequency, another one with $L = 13{,}5\,\text{mm}$ is fabricated. The return loss of both antennas is displayed in figure 5.13.

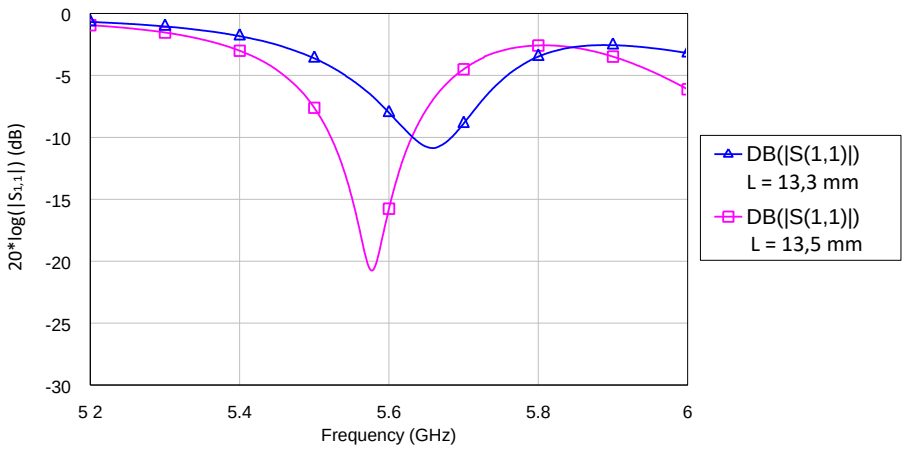

Figure 5.13: Return loss of the fabricated microstrip antennas for $L = 13{,}3\,\text{mm}$ and $L = 13{,}5\,\text{mm}$

The antenna with $L = 13{,}3\,\text{mm}$ has a resonant frequency of 5,66 GHz, which does not satisfy the requirements. From the figure it is apparent that the increase of the length causes the resonant frequency to shift to lower frequencies. The patch with $L = 13{,}5\,\text{mm}$ has a resonant frequency of 5,577 GHz. Furthermore, the matching and the bandwidth are significantly better. The lower band edge of this antenna is at 5,519 GHz and the upper band edge is at 5,634 GHz, the bandwidth is 2,05 %.

The reason for the poor agreement regarding the antenna with $L = 13{,}3\,\text{mm}$ between simulation and measurement is due to the substrate. The substrate modeled in *CST* cannot represent the real one. For further fabrications the lengths of all patch antennas are set to 13,5 mm, whereas the simulations are performed with a length of 13,3 mm.

In the following only the fabricated patch with 13,5 mm is considered. The input impedance loci of the simulated and the measured patch are displayed in the Smith chart in figure 5.14.

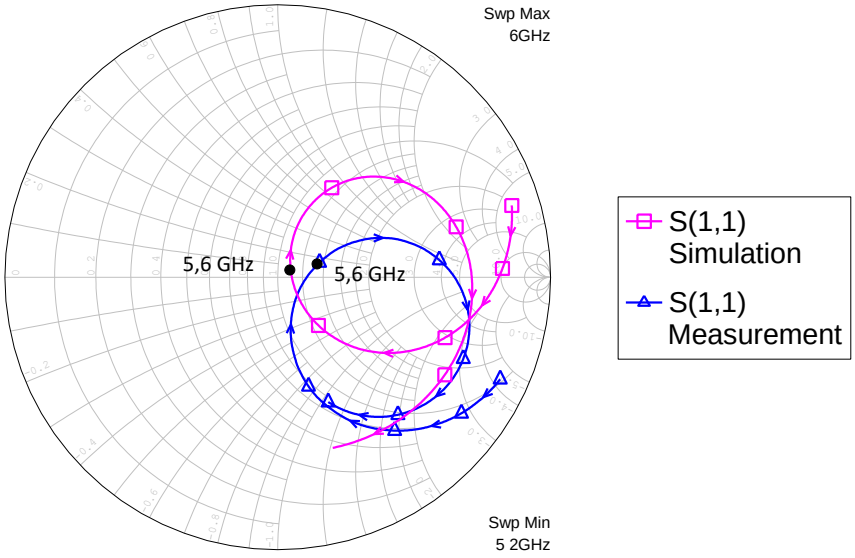

Figure 5.14: Input impedance loci of the simulated and the measured microstrip antenna

The black dots in the figure indicate the frequency of 5,6 GHz. One can see that the locus of the measurement is slightly shifted in relation to that of the simulation. Furthermore, the operating point at 5,6 GHz is shifted to the right side. The measured input impedance is $(67{,}65 + 7{,}55\mathrm{i})\,\Omega$. The deviation between simulation and substrate can be explained with inaccuracies in the geometry of the fabricated antenna. Even small changes in the length of the edges and the offset of the feed can cause the increase of the input impedance. Another aspect is that there is a thin air slot between the interface of the connector and the ground plane of the antenna. As consequence of this measurement, emphasis is placed on filing the interface of the connector to minimize the air slot.

a

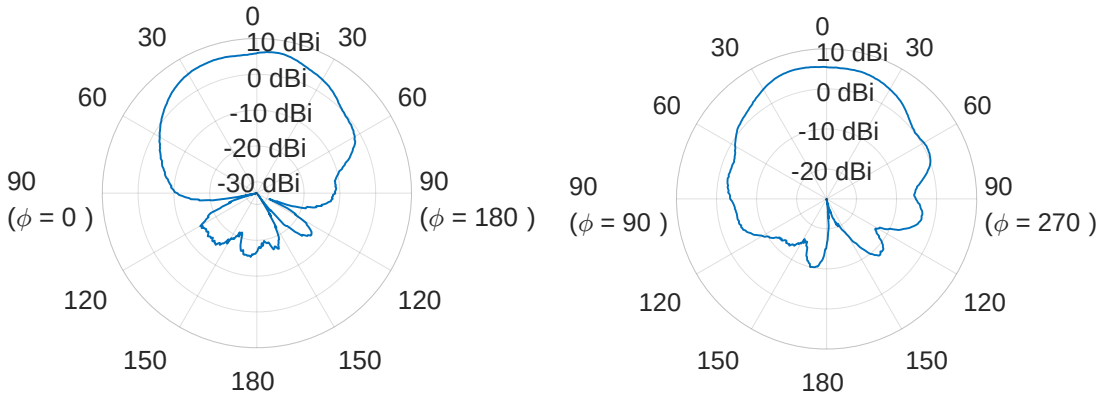

(a) E-plane (b) H-plane

Figure 5.15: Radiation patterns of the fabricated microstrip antenna

One can see that a good agreement with the simulated antenna patterns from figure 4.23 is achieved. Both patterns are almost symmetrical, deviations are due to the feed and the measurement setup.

All measured parameters are listed in table 5.5 and are compared with the requirements.

Parameter	**Required**	**Measured**	**Satisfied**
Resonant frequency	5,6 GHz ± 56 MHz	5,577 GHz	✓
Bandwidth	2 %	2,05 %	✓
Input impedance @ 5,6 GHz	50 Ω ± (10 + 10i) Ω	(67,65 + 7,55i) Ω	×
Realized gain E-plane	5,5 dBi	6,39 dBi	✓
Realized gain H-plane	5,5 dBi	5,73 dBi	✓

Table 5.5: Comparison of the measured and required parameters of the fabricated microstrip antenna

The fabricated antenna does not satisfy the requirement in the input impedance, all other requirements are fulfilled. Measurements have revealed a realized gain of about 6 dBi. The variation of the realized gain in the E-plane and H-plane can be explained with inaccuracies in the measurement setup. The measurement of the realized gain is explained in appendix D. As mentioned above, the connection of the SMA connector to the antenna is improved for further antennas.

5.6 Linear array

Firstly, the scattering parameters of the linear three-element array are measured. Afterwards, the radiation characteristic is measured. The resonant frequency of all elements is measured and listed in table 5.6.

Element	Resonant frequency f_0	Deviation
1	5,611 GHz	0,2 %
2	5,594 GHz	−0,11 %
3	5,6 GHz	0 %

Table 5.6: Measured resonant frequencies of the linear array

From the table it is apparent that good agreements in the resonant frequency are achieved. The maximum deviation is approximately 0,2 %. In comparison to the single microstrip antenna in section 5.5, the better agreements can be explained with the change in the width (see section 4.5) and the enhanced connection from the connector to the antenna. Furthermore, the parameters of the substrate might vary due to different batches.

The mutual coupling of the antenna elements is displayed in figure 5.16.

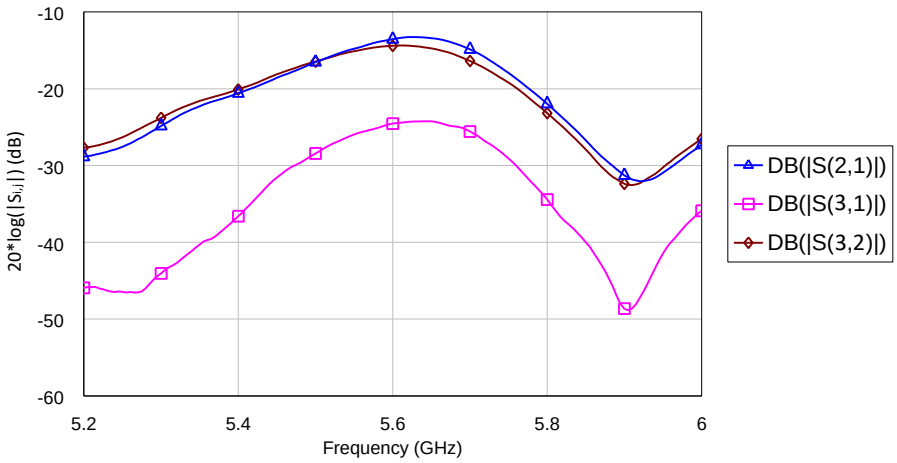

Figure 5.16: Mutual coupling of the fabricated linear three-element array

For the frequency range from 5,2 GHz to 6 GHz the mutual coupling is below −10 dB. The parameter $|S_{3,1}|$ is lower than the other ones due to the greater spacing between the outer elements.

5.6.1 Measurement of the radiation characteristic

In the following the radiation patterns of the linear three-element antenna are presented. To scan the beam, three output ports of the feed network module are used. The integrated phase shifters are aligned before each measurement. The adjusted phases and appropriate magnitudes can be obtained from table 5.7. The table lists the phases and magnitudes, that are used to excite the antenna elements. Each measurement of the radiation characteristic is indicated by the progressive phase shift in the first column. The antenna elements are indicated by the appropriate rows. The first row of a measurement represents the first element, the second row represents the second element and the third row represents the third element. The table does not take errors due to the measurement setup into account. This is described in section 5.4.

Desired progressive phase shift β	**Adjusted phase**	**Phase error**	**Magnitude**	**Magnitude error**
$0\,°(\theta_0 = 0\,°)$	$-170{,}12\,°$	-	$-19{,}54\,\mathrm{dB}$	$0{,}57\,\mathrm{dB}$
	$-170{,}03\,°$	$0{,}09\,°$	$-18{,}17\,\mathrm{dB}$	$0{,}8\,\mathrm{dB}$
	$-170{,}09\,°$	$0{,}03\,°$	$-19{,}19\,\mathrm{dB}$	$0{,}22\,\mathrm{dB}$
$15{,}69\,°(\theta_0 = 5\,°)$	$-170{,}12\,°$	-	$-19{,}54\,\mathrm{dB}$	$0{,}51\,\mathrm{dB}$
	$-154{,}41\,°$	$0{,}02\,°$	$-19{,}33\,\mathrm{dB}$	$0{,}72\,\mathrm{dB}$
	$-138{,}74\,°$	$0{,}02\,°$	$-21{,}28\,\mathrm{dB}$	$0{,}51\,\mathrm{dB}$
$31{,}26\,°(\theta_0 = 10\,°)$	$-170{,}12\,°$	-	$-19{,}54\,\mathrm{dB}$	$0{,}66\,\mathrm{dB}$
	$-138{,}74\,°$	$0{,}12\,°$	$-21{,}28\,\mathrm{dB}$	$1{,}08\,\mathrm{dB}$
	$-107{,}61\,°$	$0{,}13\,°$	$-19{,}78\,\mathrm{dB}$	$0{,}42\,\mathrm{dB}$
$46{,}59\,°(\theta_0 = 15\,°)$	$-170{,}12\,°$	-	$-19{,}54\,\mathrm{dB}$	$0{,}1\,\mathrm{dB}$
	$-123{,}33\,°$	$0{,}2\,°$	$-19{,}81\,\mathrm{dB}$	$0{,}37\,\mathrm{dB}$
	$-76{,}04\,°$	$0{,}7\,°$	$-18{,}98\,\mathrm{dB}$	$0{,}46\,\mathrm{dB}$
$61{,}56\,°(\theta_0 = 20\,°)$	$-170{,}11\,°$	-	$-20{,}22\,\mathrm{dB}$	$0{,}07\,\mathrm{dB}$
	$-108{,}57\,°$	$0{,}02\,°$	$-19{,}87\,\mathrm{dB}$	$0{,}42\,\mathrm{dB}$
	$-46{,}71\,°$	$0{,}3\,°$	$-20{,}77\,\mathrm{dB}$	$0{,}48\,\mathrm{dB}$
$76{,}07\,°(\theta_0 = 25\,°)$	$-170{,}11\,°$	-	$-20{,}22\,\mathrm{dB}$	$0{,}65\,\mathrm{dB}$
	$-93{,}87\,°$	$0{,}14\,°$	$-19{,}56\,\mathrm{dB}$	$1{,}31\,\mathrm{dB}$
	$-17{,}92\,°$	$0{,}12\,°$	$-22{,}83\,\mathrm{dB}$	$1{,}96\,\mathrm{dB}$
$90\,°(\theta_0 = 30\,°)$	$-170{,}48\,°$	-	$-19{,}82\,\mathrm{dB}$	$0{,}77\,\mathrm{dB}$
	$-80{,}28\,°$	$0{,}2\,°$	$-20{,}90\,\mathrm{dB}$	$0{,}31\,\mathrm{dB}$
	$9{,}36\,°$	$0{,}36\,°$	$-21{,}06\,\mathrm{dB}$	$0{,}47\,\mathrm{dB}$
$103{,}24\,°(\theta_0 = 35\,°)$	$-170{,}48\,°$	-	$-19{,}82\,\mathrm{dB}$	$0{,}39\,\mathrm{dB}$
	$-67{,}33\,°$	$0{,}09\,°$	$-19{,}09\,\mathrm{dB}$	$0{,}34\,\mathrm{dB}$
	$36{,}06\,°$	$0{,}15\,°$	$-19{,}38\,\mathrm{dB}$	$0{,}05\,\mathrm{dB}$

Table 5.7: Adjusted phases and magnitudes of the linear three-element array for scanning

The column *phase error* gives the phase error between two elements relative to the desired progressive phase shift. The column *magnitude error* gives the magnitude error of an element relative to the average of the magnitudes for one measurement. The maximum phase error of all measurements is 0,7 ° and the maximum magnitude error is 1,96dB. As special emphasis is placed on accurate phase excitation, the phase error is low for the measurements. The variation in the magnitude errors is due to the phase shifter and cannot be adjusted.

The measured patterns indicate the realized gain of the antenna array. For this reason, the corresponding simulated patterns from *CST* are taken. To create a basis for comparison, the lowest level is set to −30 dBi in the polar illustrations. Otherwise dips in the measurements distort the patterns. In contrary, the Cartesian ones are normalized to a maximum of 0 dB to illustrate the relative sidelobe level. In figure 5.17 the E-plane patterns for a desired radiation toward $\theta_0 = 0\,°$ are displayed.

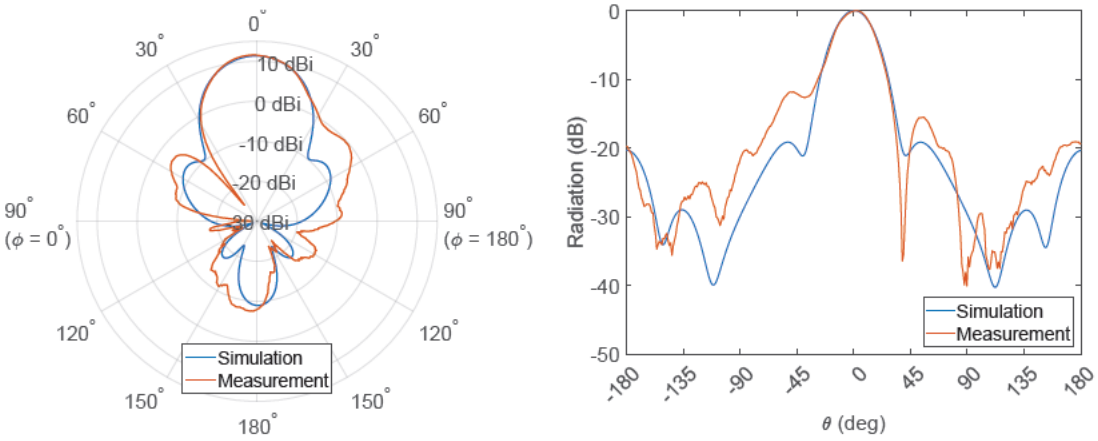

(a) Polar (b) Cartesian

Figure 5.17: E-planes of the measured and simulated linear three-element array in polar and Cartesian form with desired radiation toward $\theta_0 = 0\,°$

Figure 5.18 shows the measured radiation in the H-plane for desired radiation toward $\theta_0 = 0\,°$.

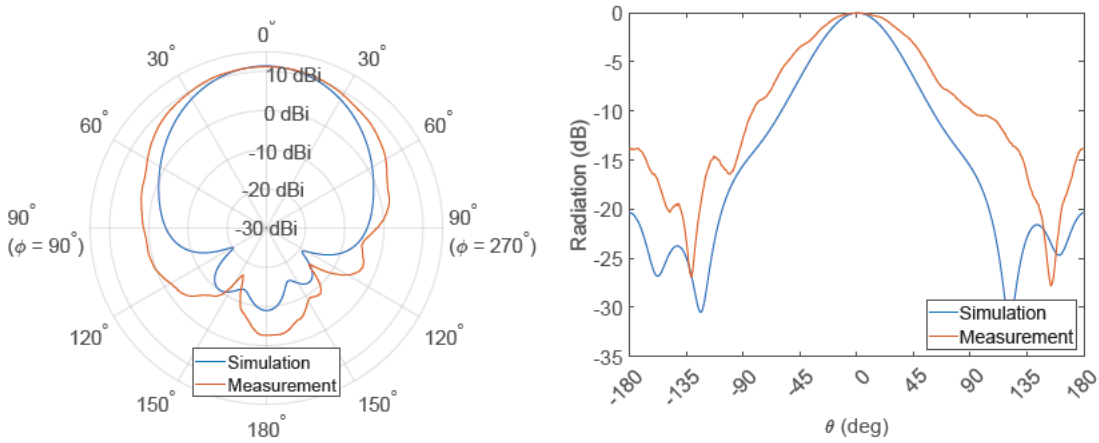

(a) Polar (b) Cartesian

Figure 5.18: H-planes of the measured and simulated linear three-element array in polar and Cartesian form with desired radiation toward $\theta_0 = 0\,°$

Overall, there is a good agreement between the simulated and measured shapes. Especially, the radiation close to broadside is very similar. The measured radiation is greater for wider angles off broadside. The maximum realized gain of the simulated array is 11,37 dBi. In the measurements a realized gain of 11,58 dBi is obtained in the E-plane and of 11,19 dBi in the H-plane. Deviations in the realized gain measurement can be explained with inaccuracies from the measurement setup.

The beam steering toward $\phi_0 = 0\,°$ is shown in the following figures. The patterns for radiation toward $\phi_0 = 180\,°$ are displayed in appendix F.1.

Figure 5.19 shows the measured and simulated patterns for desired radiation toward $\theta_0 = 5\,°$.

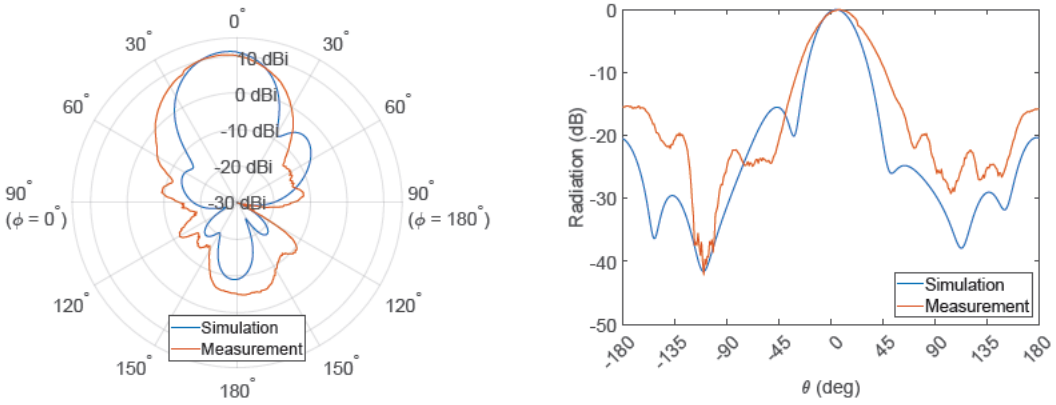

(a) Polar (b) Cartesian

Figure 5.19: E-planes of the measured and simulated linear three-element array in polar and Cartesian form with desired radiation toward $\theta_0 = 5\,°$

The measured and simulated patterns for beam steering toward $\theta_0 = 10\,°$ are shown in figure 5.20.

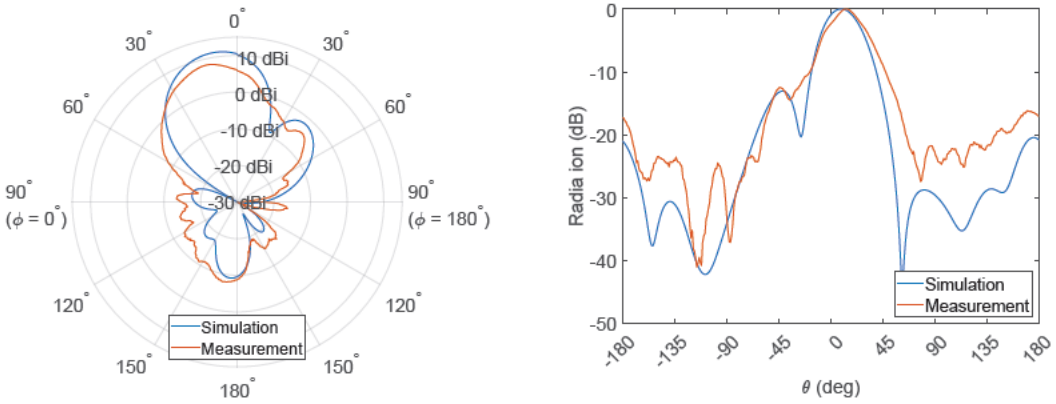

(a) Polar (b) Cartesian

Figure 5.20: E-planes of the measured and simulated linear three-element array in polar and Cartesian form with desired radiation toward $\theta_0 = 10\,°$

From figure 5.19 one can see that the back radiation of the fabricated antenna is significantly greater than that of the simulated antenna. The highest sidelobe is at approximately $\theta = 180\,°$ and is about $-15\,\text{dB}$. Figure 5.20 shows that the realized gain of the fabricated antenna decreases to 8,29 dBi. In contrary, the realized gain of the simulated antenna is 11,27 dBi.

The measured and simulated radiation characteristic for desired radiation toward $\theta_0 = 15\,°$ is displayed in figure 5.21.

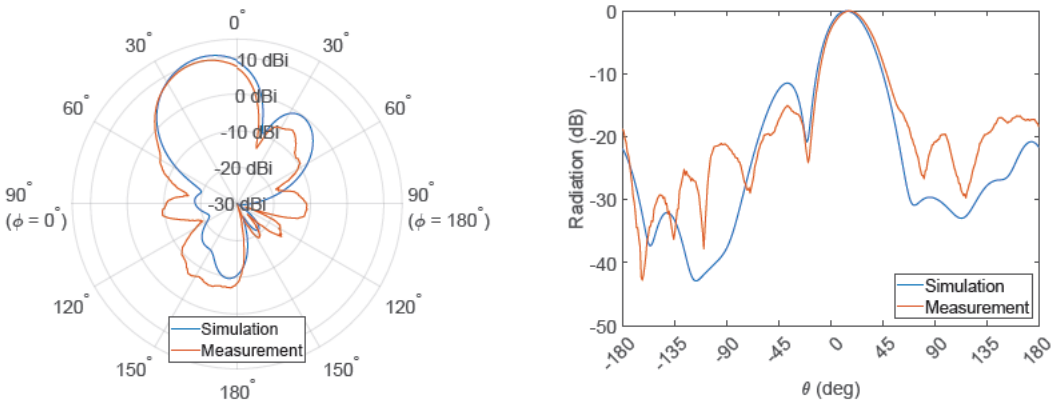

(a) Polar (b) Cartesian

Figure 5.21: E-planes of the measured and simulated linear three-element array in polar and Cartesian form with desired radiation toward $\theta_0 = 15\,°$

Figure 5.22 shows the measured and simulated patterns for desired radiation toward $\theta_0 = 20\,°$.

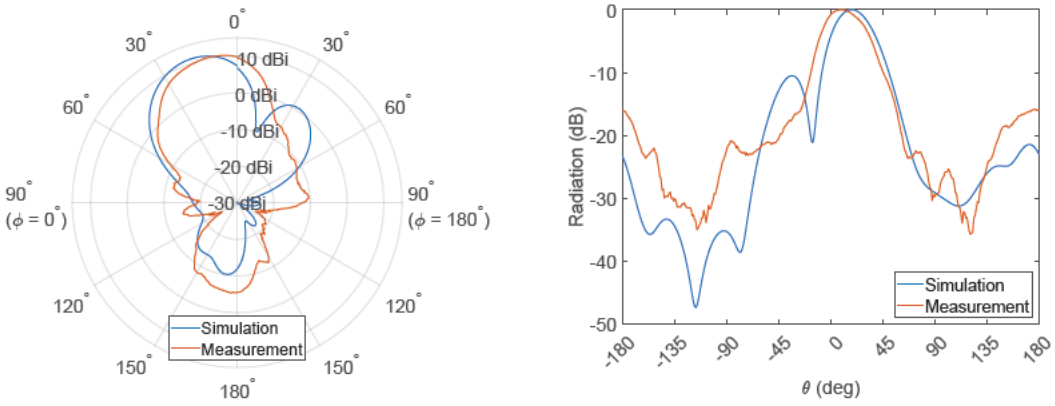

(a) Polar (b) Cartesian

Figure 5.22: E-planes of the measured and simulated linear three-element array in polar and Cartesian form with desired radiation toward $\theta_0 = 20\,°$

There is a good agreement in realized gain between the simulated and measured pattern for figure 5.21. Furthermore, the measured pattern exhibits a sidelobe at $\theta = -40\,°$, too. From figure 5.22 it is apparent that the scanning of the fabricated antenna toward $\theta_0 = 20\,°$ suffers. The maximum radiation is measured at $\theta = 10\,°$. In contrary, the beam of the simulated antenna achieves a scan angle of $\theta = 18\,°$.

The beam steering of the measured and simulated linear array toward a desired radiation of $\theta_0 = 25\,°$ is shown in figure 5.23.

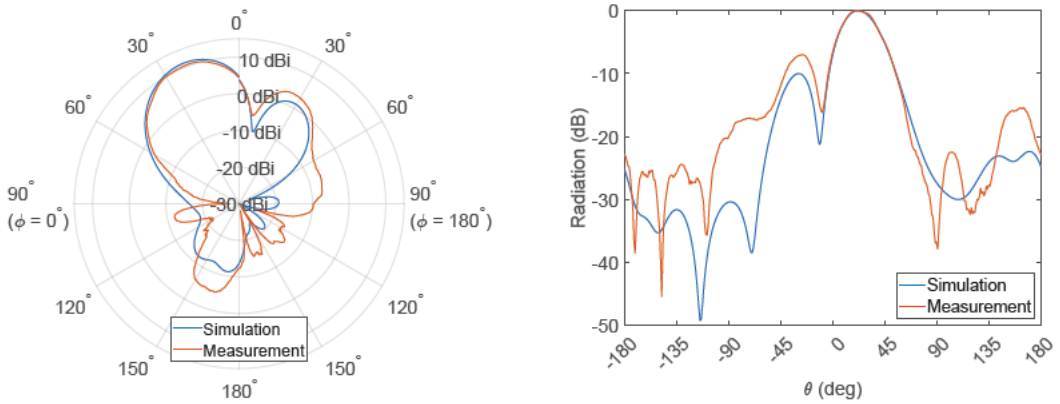

(a) Polar (b) Cartesian

Figure 5.23: E-planes of the measured and simulated linear three-element array in polar and Cartesian form with desired radiation toward $\theta_0 = 25\,°$

From the figure one can see that a good agreement in the shape of the maximum and the first sidelobe is achieved. The achieved scan angle of the simulation is 22 °, that of the measurement is 20 °. The realized gain of the simulated antenna is about 0,7 dB greater than that of the measured antenna. Furthermore, the relative sidelobe level of the measured antenna is about 3 dB greater than that of the simulated antenna. As the relative sidelobe level of this measurement is about −7 dB, the defined requirements of section 3.5 are not fulfilled for this scan angle. The beam steering toward $\theta_0 = 30\,°$ and $\theta_0 = 35\,°$ for $\phi_0 = 0\,°$ is shown in appendix F.1.

The measured parameters of the linear array are summarised and compared with the simulated parameters in table 5.8.

D. scan angle θ_0	**A. Scan angle θ_0**		**Realized gain**		**Relative sidelobe level**	
	Simu.	**Measure.**	**Simu.**	**Measure.**	**Simu.**	**Measure.**
$-35\,^\circ$	$-28\,^\circ$	$-33\,^\circ$	11 dBi	7,84 dBi	$-9{,}4$ dB	-5 dB
$-30\,^\circ$	$-25\,^\circ$	$-23\,^\circ$	11,15 dBi	9,51 dBi	$-9{,}73$ dB	$-7{,}26$ dB
$-25\,^\circ$	$-22\,^\circ$	$-24\,^\circ$	11,2 dBi	9,82 dBi	$-9{,}98$ dB	$-7{,}92$ dB
$-20\,^\circ$	$-18\,^\circ$	$-11\,^\circ$	11,2 dBi	11,55 dBi	$-10{,}48$ dB	$-12{,}49$ dB
$-15\,^\circ$	$-13\,^\circ$	$-18\,^\circ$	11,21 dBi	9,56 dBi	$-11{,}45$ dB	$-10{,}03$ dB
$-10\,^\circ$	$-9\,^\circ$	$-11\,^\circ$	11,26 dBi	8,83 dBi	$-13{,}06$ dB	$-11{,}6$ dB
$-5\,^\circ$	$-4\,^\circ$	$-4\,^\circ$	11,34 dBi	11,69 dBi	$-15{,}51$ dB	$-15{,}39$ dB
$0\,^\circ$	$0\,^\circ$	$1\,^\circ$	11,37 dBi	11,58 dBi	$-19{,}16$ dB	$-11{,}83$ dB
$5\,^\circ$	$4\,^\circ$	$6\,^\circ$	11,34 dBi	10,53 dBi	$-15{,}5$ dB	$-15{,}3$ dB
$10\,^\circ$	$9\,^\circ$	$12\,^\circ$	11,27 dBi	8,29 dBi	$-13{,}06$ dB	$-12{,}49$ dB
$15\,^\circ$	$13\,^\circ$	$16\,^\circ$	11,23 dBi	10,18 dBi	$-11{,}47$ dB	$-15{,}02$ dB
$20\,^\circ$	$18\,^\circ$	$10\,^\circ$	11,22 dBi	10,46 dBi	$-10{,}5$ dB	$-15{,}81$ dB
$25\,^\circ$	$22\,^\circ$	$20\,^\circ$	11,22 dBi	10,49 dBi	$-10{,}1$ dB	$-6{,}99$ dB
$30\,^\circ$	$25\,^\circ$	$21\,^\circ$	11,16 dBi	11,72 dBi	$-9{,}74$ dB	$-9{,}41$ dB
$35\,^\circ$	$28\,^\circ$	$30\,^\circ$	11,01 dBi	6,94 dBi	$-9{,}4$ dB	$-8{,}23$ dB

Table 5.8: Comparison of the simulated and measured parameters of the linear three-element array

From the table it is apparent that there occur partially poor agreements between measurements and simulations in the achieved scan angle, the realized gain and the relative sidelobe level. Furthermore, the figures of the patterns above indicate greater radiation of the fabricated array for undesired angles. Overall, one can see that the beam of the array is successfully steered. For greater angles off broadside the realized gain decreases and the relative sidelobe level increases. In the following the occurred errors and deviations between measurement and simulation are explained.

5.6.2 Performance of the fabricated linear array

Achieved scan angle

The achieved scan angle θ_0 suffers from inaccuracies in the measurement setup described in section 5.4.

Realized gain

The measured realized gain suffers from attenuated excitation magnitudes due to cable flexing and the phase shifter. Magnitude errors from the phase shifter are listed in table 5.7. An investigation of the described flatness error in section 5.4 has to be investigated in the future. Assuming the antenna beam is not straight to the receiver antenna, one can expect variations in the realized gain.

Relative sidelobe level

Referring to section 2.4.3, higher sidelobe levels can be caused by phase and magnitude errors as well as fabrication errors. It is assumed that the described errors in section 5.4 cause higher sidelobe levels. Furthermore, one has to consider undesired radiation of the feed network module.

The measured radiation of the linear array for $\theta_0 = 0\,°$ and the measured radiation of the feed network module are displayed in figure 5.24.

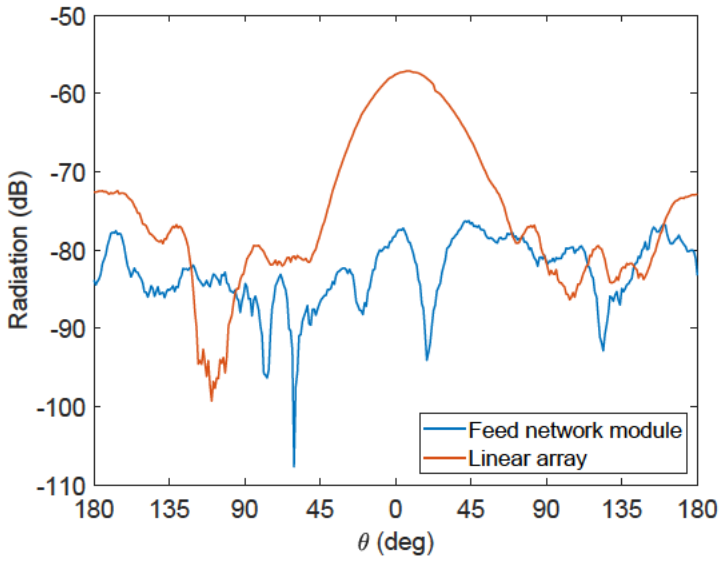

Figure 5.24: Radiation of the feed network module and fabricated linear three-element array with broadside radiation

The figure shows the undesired radiation of the feed network module, which is measured without a connected antenna. The comparison of this radiation with that of the linear array reveals that the level for angles from 60 ° to 160 ° off broadside partially are of similar value. To exclude high radiation levels caused by the module, the attenuation of the undesired radiation has to be improved in the future.

The high level in back radiation in several patterns has to be investigated in the future as well. From figure 5.24 one can see that there is about 10 dB difference between radiation of the module and back radiation of the antenna. Thus, it is assumed that the back radiation is not caused by the module. Referring to appendix F, there a several patterns with a good agreement in back radiation between simulation and measurement. Therefore, it is assumed that systematic errors cause radiation from the antenna feed.

To conclude, the measured parameters of the linear array are compared with the defined requirements in table 5.9. The listed values are related to the achieved scan range from $\theta_0 = -18\,^\circ$ to $\theta_0 = 16\,^\circ$ in the E-plane.

Parameter	**Required**	**Measured**	**Satisfied**
Scan angle θ_0	$> \pm\, 20\,^\circ$	$-18\,^\circ$ to $16\,^\circ$	×
Relative side lobe level	$< -10\,\mathrm{dB}$	$-10{,}03\,\mathrm{dB}$	✓
Realized gain	$> 10\,\mathrm{dBi}$	$8{,}29\,\mathrm{dBi}$	×
Realized gain variation	$< 1\,\mathrm{dB}$	$3{,}4\,\mathrm{dB}$	×
Mutual coupling	$< -10\,\mathrm{dB}$	$-13{,}54\,\mathrm{dB}$	✓

Table 5.9: Comparison of the measured and required parameters of the linear three-element array for the achieved scan range for 5,6 GHz

The beam of the linear array can be steered from $\theta_0 = -18\,^\circ$ to $\theta_0 = 16\,^\circ$, this is apparent from table 5.8. The requirement of the relative sidelobe level limits the scan range. The highest sidelobe in the achieved scan range is $-10{,}03\,\mathrm{dB}$ at $\theta_0 = -18\,^\circ$. At $\theta_0 = 12\,^\circ$ a realized gain of $8{,}29\,\mathrm{dBi}$ is measured. Thus, the requirement of at least $10\,\mathrm{dBi}$ is not fulfilled. The required maximum variation in realized gain is not satisfied as the measured variation is $3{,}4\,\mathrm{dB}$.

As consequence of the measurements, the mount of the antenna is strengthened. However, for the given conditions it is difficult to enhance the overall performance. Due to the inaccuracies in the measurement setup, no further linear arrays with different spacings are fabricated.

5.7 Planar array

Firstly, the scattering parameters of the nine elements are measured. Then, the radiation characteristic is measured.

The resonant frequency of each element is listed in table 5.10.

Element	**Resonant frequency f_0**	**Deviation**
1	5,66 GHz	1,07 %
2	5,64 GHz	0,71 %
3	5,625 GHz	0,45 %
4	5,63 GHz	0,54 %
5	5,655 GHz	0,98 %
6	5,63 GHz	0,54 %
7	5,65 GHz	0,89 %
8	5,645 GHz	0,8 %
9	5,67 GHz	1,25 %

Table 5.10: Measured resonant frequencies of the planar array

The maximum deviation is 1,25 %. As the resonant frequencies of all elements are consequently greater than 5,6 GHz, it is assumed that there is a small change of the substrate's dielectric constant in comparison to that of the linear array. Referring to table 5.6 the maximum deviation of the linear array is 0,2 %.

The mutual coupling in E-plane and in H-plane is shown in figure 5.25 for exemplary ports.

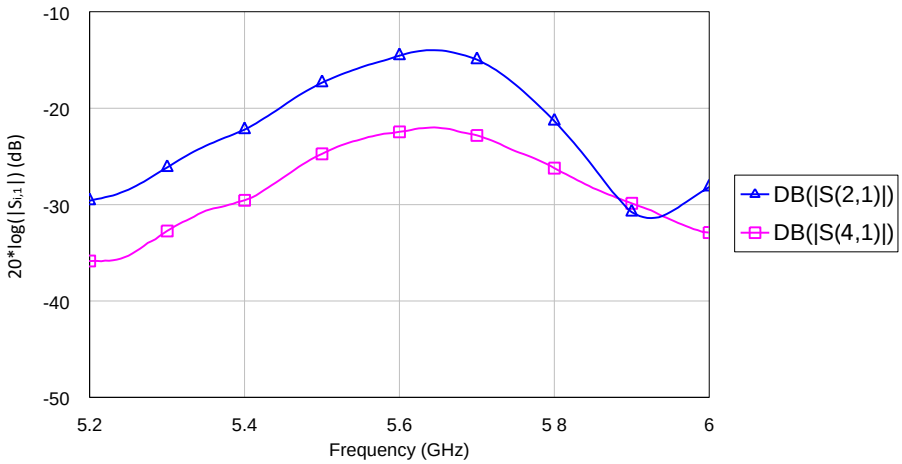

Figure 5.25: Mutual coupling of the fabricated planar 3x3 array in E-plane and H-plane

The figure shows the E-plane coupling for $|S_{2,1}|$ and the H-plane coupling for $|S_{4,1}|$. At 5,6 GHz the E-plane coupling is about $-14{,}55$ dB and the H-plane coupling is about $-22{,}46$ dB. Thus, the required values of at maximum -10 dB in the E-plane and -20 dB in the H-plane are fulfilled.

5.7.1 Measurement of the radiation characteristic

The radiation patterns of the planar array are presented for scanning in the E-plane and H-plane in the following. All phase shifters are adjusted before the measurements. Due to the feed network module, there occur phase and magnitudes error of the same degree as shown in table 5.7 for the linear array. For both E-plane and H-plane the estimated realized gain of the fabricated planar array is significantly greater than that of the simulated one. For this reason, there is a huge difference in the polar characteristics.

The radiation patterns in the E-plane toward a desired radiation of $\theta_0 = 0\,°$ are displayed in figure 5.26 for the measured and simulated planar array.

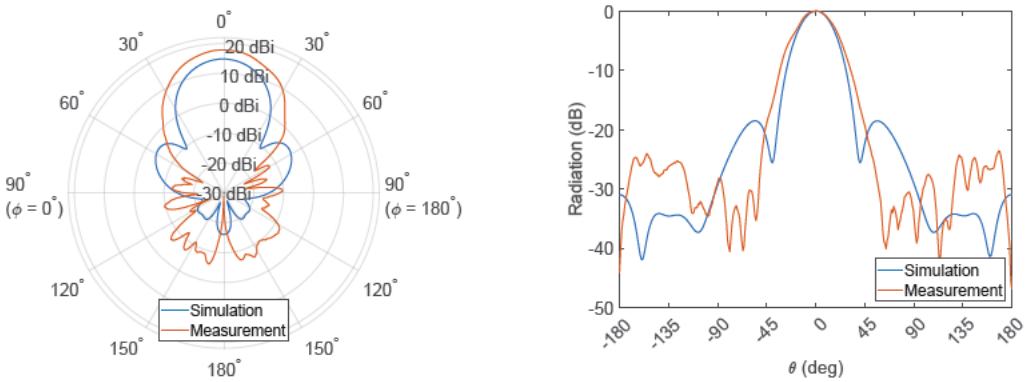

(a) Polar (b) Cartesian

Figure 5.26: E-planes of the measured and simulated planar 3x3 array in polar and Cartesian form with desired radiation toward $\theta_0 = 0\,°$

The measured and simulated radiation characteristic for desired radiation toward $\theta_0 = 5\,°$ is displayed in figure 5.27.

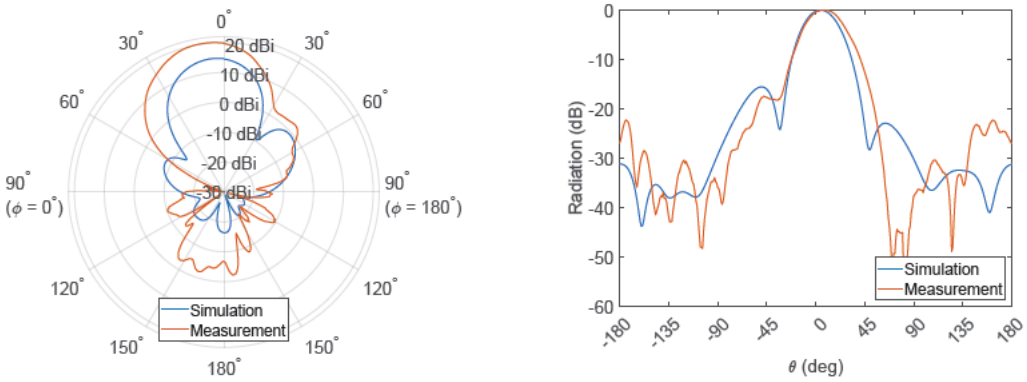

(a) Polar (b) Cartesian

Figure 5.27: E-planes of the measured and simulated planar 3x3 array in polar and Cartesian form with desired radiation toward $\theta_0 = 5\,°$

The back radiation of the fabricated array in both figures 5.26 and 5.27 is greater than that of the simulated array. The simulated array with $\theta_0 = 0\,°$ has sidelobes of about $-18{,}5\,\mathrm{dB}$ at $\theta = 45\,°$, whereas the sidelobe level of the fabricated array is about $-30\,\mathrm{dB}$ for this direction. Furthermore, one can see that the realized gain of the fabricated array with desired radiation toward $\theta_0 = 0\,°$ is about $2{,}5\,\mathrm{dB}$ less than that of the fabricated array with desired radiation toward $\theta_0 = 5\,°$.

The beam steering toward a desired radiation of $\theta_0 = 10\,°$ for the measured and simulated planar array is displayed in figure 5.28.

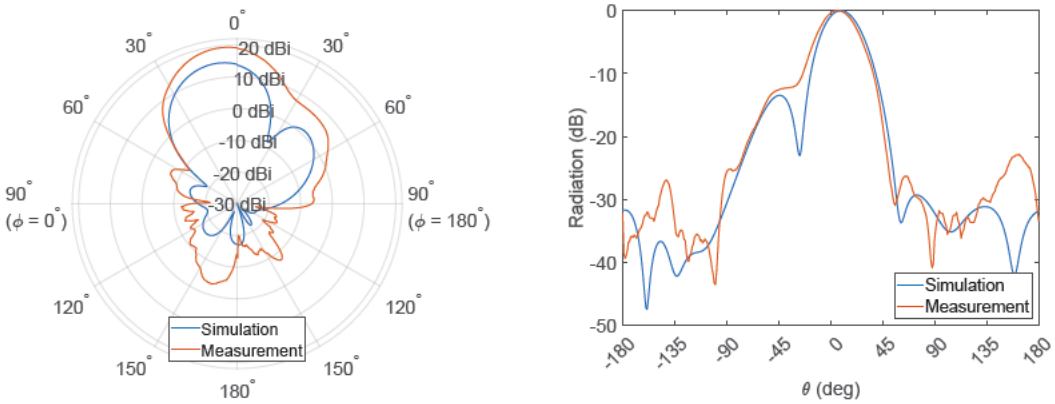

(a) Polar (b) Cartesian

Figure 5.28: E-planes of the measured and simulated planar 3x3 array in polar and Cartesian form with desired radiation toward $\theta_0 = 10\,°$

The measured and simulated radiation characteristic for desired radiation toward $\theta_0 = 15\,°$ is displayed in figure 5.29.

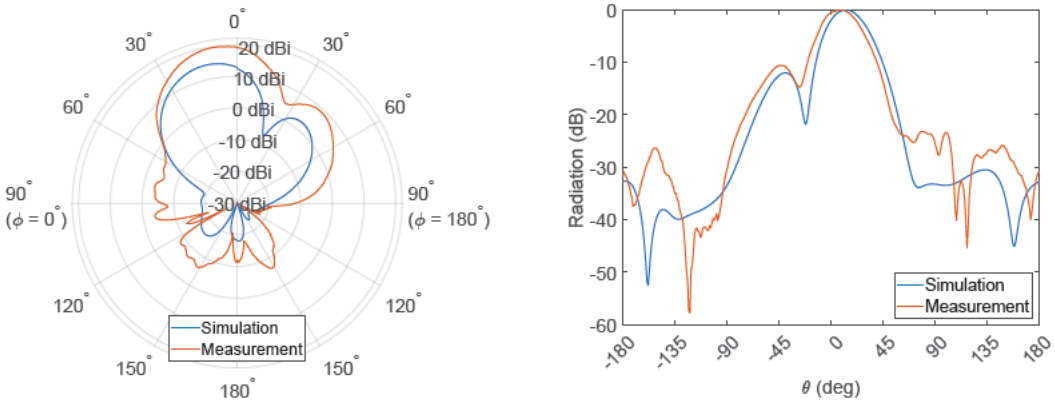

(a) Polar (b) Cartesian

Figure 5.29: E-planes of the measured and simulated planar 3x3 array in polar and Cartesian form with desired radiation toward $\theta_0 = 15\,°$

The Cartesian figures 5.28b and 5.29b show a good agreement between the shape of the simulated and measured pattern. From figure 5.29 it is apparent that the maximum radiation of the fabricated array runs after the desired radiation. For desired radiation toward $\theta_0 = 15\,°$ the simulated array achieves $13\,°$ and the fabricated $8\,°$.

The beam steering toward a desired radiation of $\theta_0 = 20\,°$ for the measured and simulated planar array is displayed in figure 5.30.

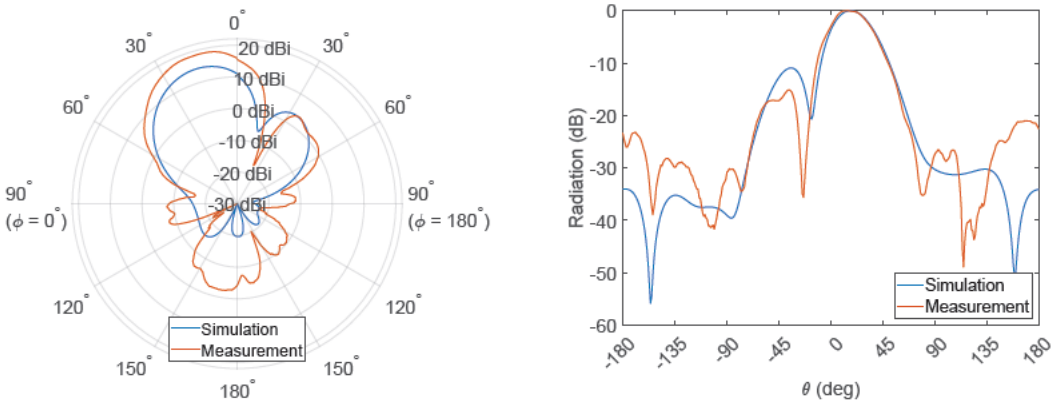

(a) Polar (b) Cartesian

Figure 5.30: E-planes of the measured and simulated planar 3x3 array in polar and Cartesian form with desired radiation toward $\theta_0 = 20\,°$

The measured and simulated radiation characteristic for desired radiation toward $\theta_0 = 25\,°$ is displayed in figure 5.31.

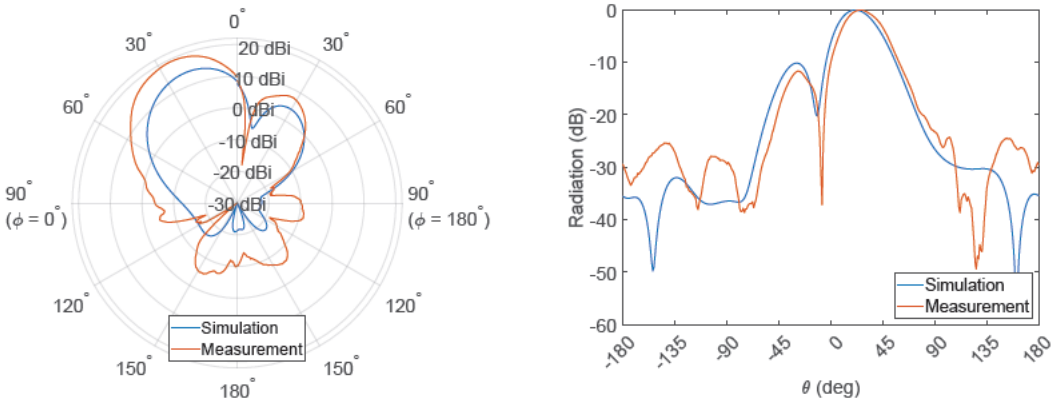

(a) Polar (b) Cartesian

Figure 5.31: E-planes of the measured and simulated planar 3x3 array in polar and Cartesian form with desired radiation toward $\theta_0 = 25\,°$

Both figures 5.30 and 5.31 show that the relative sidelobe level of the simulated planar array is slightly greater than that of the measured one. The back radiation of the fabricated array with desired radiation toward $\theta_0 = 20\,°$ is greater than that of the fabricated array with desired radiation toward $\theta_0 = 25\,°$.

The beam steering toward a desired radiation of $\theta_0 = 30\,°$ for the measured and simulated planar array is displayed in figure 5.32.

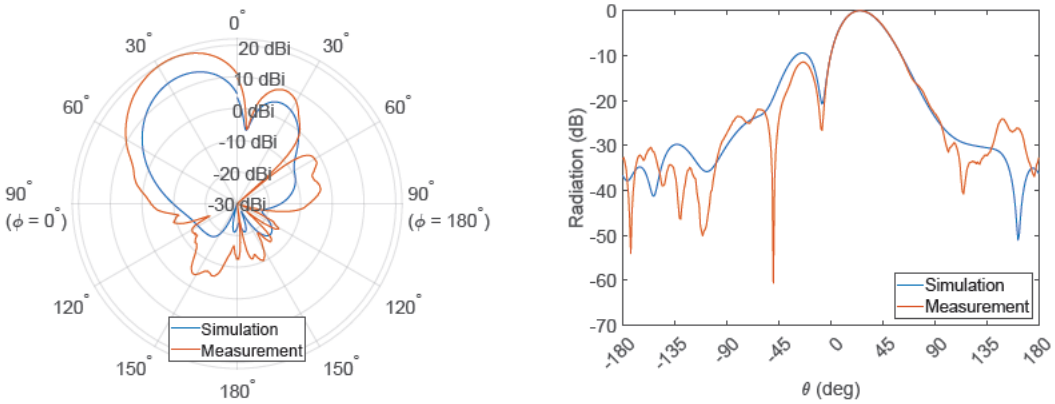

(a) Polar (b) Cartesian

Figure 5.32: E-planes of the measured and simulated planar 3x3 array in polar and Cartesian form with desired radiation toward $\theta_0 = 30\,°$

The measured and simulated radiation characteristic for desired radiation toward $\theta_0 = 35\,°$ is displayed in figure 5.33.

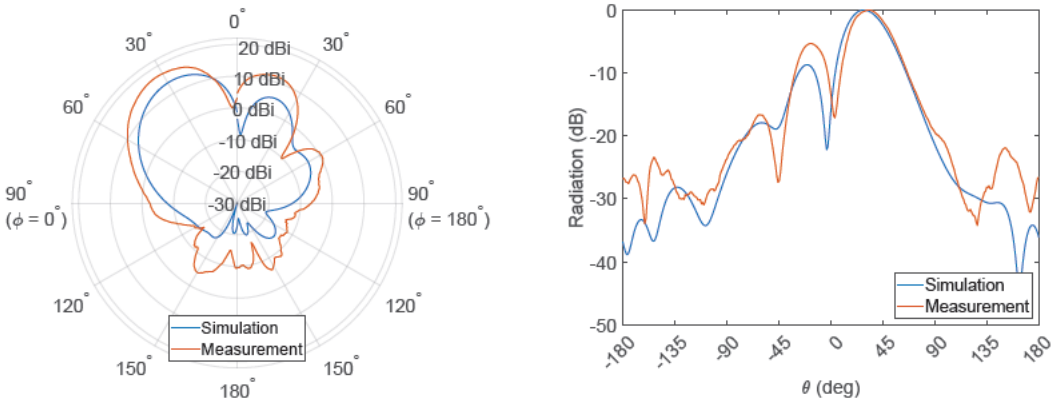

(a) Polar (b) Cartesian

Figure 5.33: E-planes of the measured and simulated planar 3x3 array in polar and Cartesian form with desired radiation toward $\theta_0 = 35\,°$

The difference in realized gain of the fabricated antenna between desired radiation toward $\theta_0 = 30\,°$ and $\theta_0 = 35\,°$ is about 3 dB. Furthermore, one can see from figure 5.33 that the relative sidelobe level of the fabricated planar array is about -5 dB. Thus, this scan angle does not fulfill the requirements.

The table 5.11 lists the simulated and measured performance of the planar array for beam steering in the E-plane.

D. scan	**A. Scan angle θ_0**		**Realized gain**		**Relative sidelobe level**	
angle θ_0	**Simu.**	**Measure.**	**Simu.**	**Measure.**	**Simu.**	**Measure.**
$-35\,^\circ$	$-28\,^\circ$	$-29\,^\circ$	13,78 dBi	17,25 dBi	$-8{,}7$ dB	$-4{,}95$ dB
$-30\,^\circ$	$-25\,^\circ$	$-26\,^\circ$	14,02 dBi	19,3 dBi	$-9{,}41$ dB	$-11{,}5$ dB
$-25\,^\circ$	$-21\,^\circ$	$-21\,^\circ$	14,23 dBi	19,35 dBi	$-10{,}13$ dB	$-9{,}68$ dB
$-20\,^\circ$	$-17\,^\circ$	$-20\,^\circ$	14,41 dBi	18,76 dBi	$-10{,}94$ dB	$-12{,}5$ dB
$-15\,^\circ$	$13\,^\circ$	$-13\,^\circ$	14,57 dBi	19,46 dBi	$-11{,}99$ dB	$-13{,}91$ dB
$-10\,^\circ$	$-8\,^\circ$	$-15\,^\circ$	14,71 dBi	20,03 dBi	$-13{,}47$ dB	$-10{,}57$ dB
$-5\,^\circ$	$-4\,^\circ$	$-9\,^\circ$	14,8 dBi	19,01 dBi	$-15{,}56$ dB	$-23{,}78$ dB
$0\,^\circ$	$0\,^\circ$	$0\,^\circ$	14,83 dBi	17,87 dBi	$-18{,}51$ dB	$-23{,}59$ dB
$5\,^\circ$	$4\,^\circ$	$7\,^\circ$	14,8 dBi	20,21 dBi	$-15{,}55$ dB	$-17{,}44$ dB
$10\,^\circ$	$8\,^\circ$	$6\,^\circ$	14,71 dBi	19,42 dBi	$-13{,}47$ dB	$-12{,}4$ dB
$15\,^\circ$	$13\,^\circ$	$8\,^\circ$	14,57 dBi	19,62 dBi	$-11{,}99$ dB	$-10{,}57$ dB
$20\,^\circ$	$17\,^\circ$	$13\,^\circ$	14,41 dBi	18,68 dBi	$-10{,}94$ dB	$-15{,}13$ dB
$25\,^\circ$	$21\,^\circ$	$25\,^\circ$	14,23 dBi	19,25 dBi	$-10{,}13$ dB	$-11{,}65$ dB
$30\,^\circ$	$25\,^\circ$	$24\,^\circ$	14,02 dBi	20,23 dBi	$-9{,}41$ dB	$-11{,}43$ dB
$35\,^\circ$	$28\,^\circ$	$33\,^\circ$	13,78 dBi	17,17 dBi	$-8{,}7$ dB	$-5{,}33$ dB

Table 5.11: Comparison of the simulated and measured parameters of the planar 3x3 array for scanning in the E-plane

The table shows good agreement between the achieved scan angles of the simulated and measured patterns in general. However, there are a few measured patterns with a deviation greater than $3\,^\circ$ between maximum radiation of simulation and measurement. The deviation in realized gain of simulation and measurement is at least 3 dB for all scan angles and the maximum deviation is about 5,4 dB at a desired scan angle of $\theta_0 = 5\,^\circ$. Referring to table 5.8, the agreement in realized gain regarding the linear array was significantly better. According to the defined requirements the relative sidelobe level must be maximum -10 dB for the measured characteristics. Thus, the patterns with an achieved scan angle of $\theta_0 = -21\,^\circ$ and $\theta_0 = 33\,^\circ$ do not satisfy this requirement. As the measurement with an achieved scan angle of $\theta_0 = -26\,^\circ$ exhibits a relative sidelobe level below -10 dB, the achieved scan range of the fabricated 3x3 planar array in the E-plane is assumed from $-26\,^\circ$ to $24\,^\circ$. Especially, the measured relative sidelobe levels of $\theta_0 = 0\,^\circ$ and $\theta_0 = -5\,^\circ$ are very good in relation to this measurement setup. The measured and simulated radiation characteristics for $\phi_0 = 180\,^\circ$ are shown in appendix G.1.

The radiation patterns in the H-plane toward a desired radiation of $\theta_0 = 0\,°$ are displayed in figure 5.34 for the measured and simulated planar array.

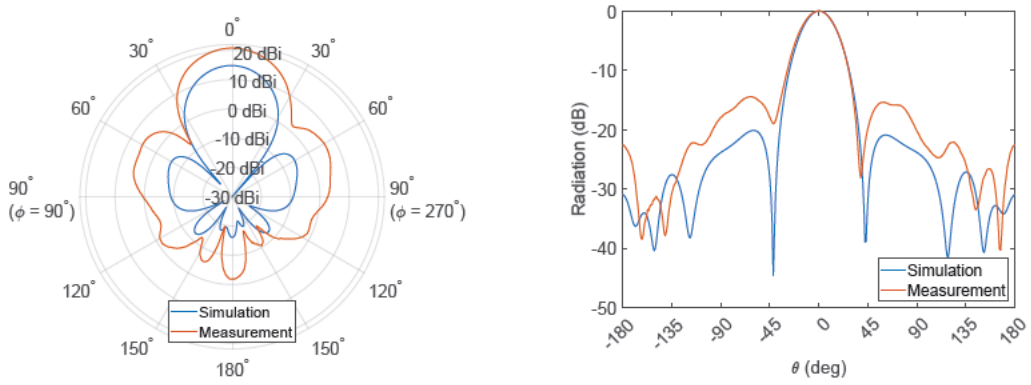

(a) Polar (b) Cartesian

Figure 5.34: H-planes of the measured and simulated planar 3x3 array in polar and Cartesian form with desired radiation toward $\theta_0 = 0\,°$

The beam steering in the H-plane toward a desired radiation of $\theta_0 = 5\,°$ is shown in figure 5.35 for the measured and simulated planar array.

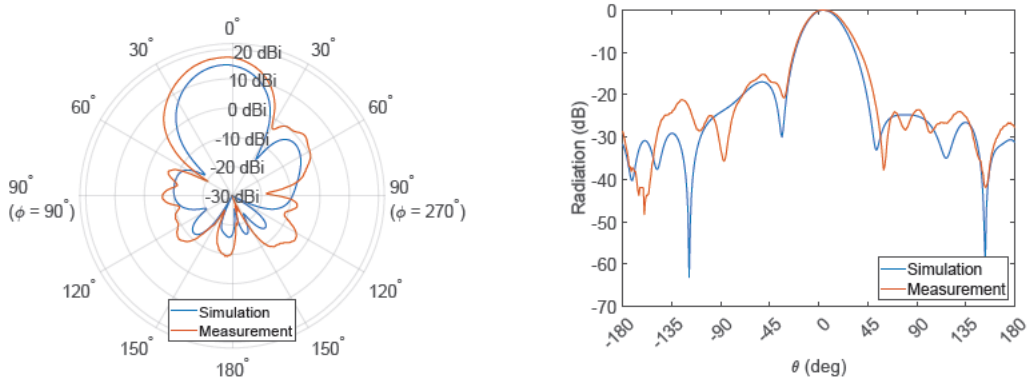

(a) Polar (b) Cartesian

Figure 5.35: H-planes of the measured and simulated planar 3x3 array in polar and Cartesian form with desired radiation toward $\theta_0 = 5\,°$

Figure 5.34b shows that the sidelobes at $\theta = 60\,°$ of the fabricated array are about 5 dB greater than those of the simulated array. Furthermore, the back radiation of the fabricated antenna is high in comparison to the simulated one. The agreement in pattern shape between the simulated and measured array for desired radiation toward $\theta_0 = 5\,°$ is significantly better. The realized gain of the fabricated antenna for radiation toward $0\,°$ is about 3 dB greater than for radiation toward $5\,°$.

The radiation patterns in the H-plane toward a desired radiation of $\theta_0 = 10\,°$ are displayed in figure 5.36 for the measured and simulated planar array.

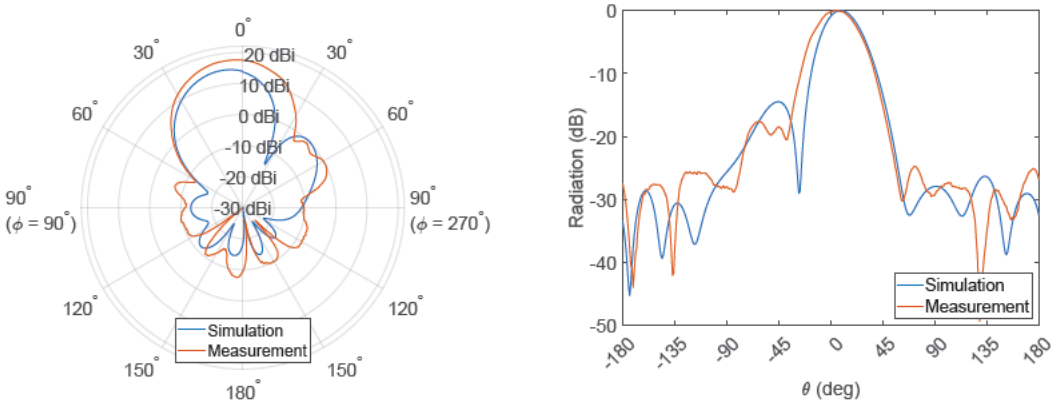

(a) Polar (b) Cartesian

Figure 5.36: H-planes of the measured and simulated planar 3x3 array in polar and Cartesian form with desired radiation toward $\theta_0 = 10\,°$

The beam steering in the H-plane toward a desired radiation of $\theta_0 = 15\,°$ is shown in figure 5.37 for the measured and simulated planar array.

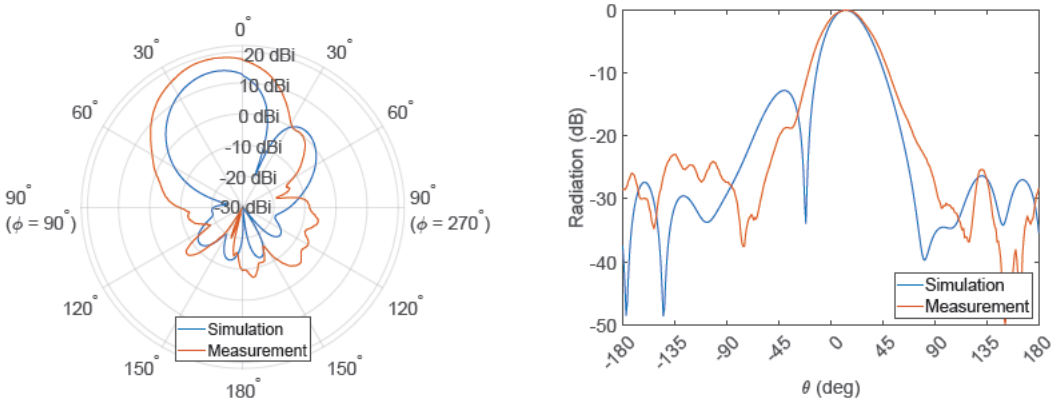

(a) Polar (b) Cartesian

Figure 5.37: H-planes of the measured and simulated planar 3x3 array in polar and Cartesian form with desired radiation toward $\theta_0 = 15\,°$

From figure 5.36 one can see that the achieved scan angles differ. The achieved scan angle of the fabricated array is only $4\,°$, whereas the achieved scan angle of the simulated array is $8\,°$. Overall, the Cartesian figures 5.36b and 5.37b show good agreement between the measured and simulated patterns.

The radiation patterns in the H-plane toward a desired radiation of $\theta_0 = 20\,°$ are displayed in figure 5.34 for the measured and simulated planar array.

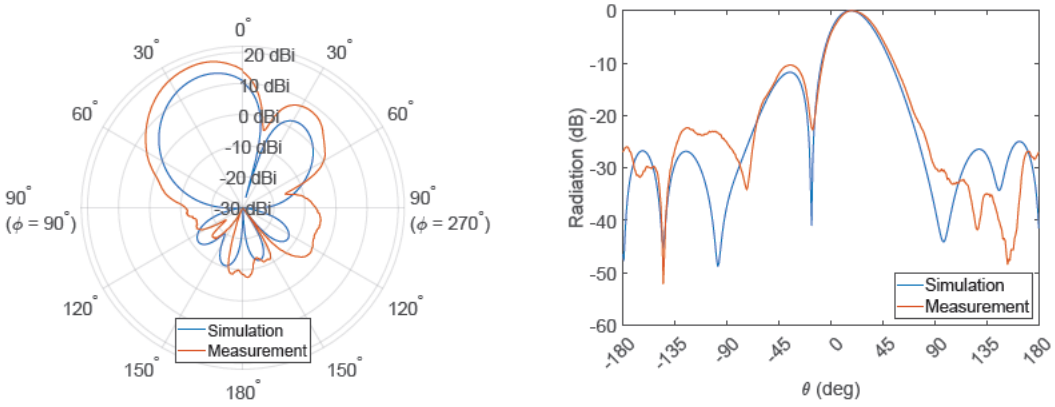

(a) Polar (b) Cartesian

Figure 5.38: H-planes of the measured and simulated planar 3x3 array in polar and Cartesian form with desired radiation toward $\theta_0 = 20\,°$

The beam steering in the H-plane toward a desired radiation of $\theta_0 = 25\,°$ is shown in figure 5.39 for the measured and simulated planar array.

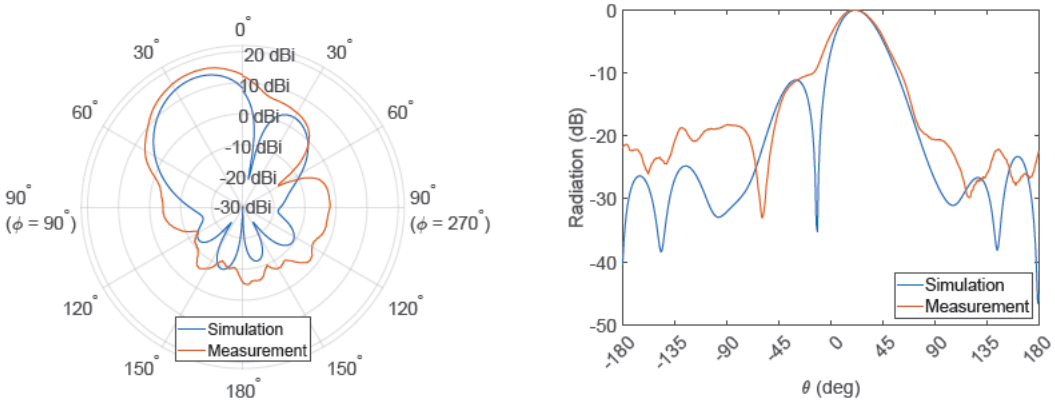

(a) Polar (b) Cartesian

Figure 5.39: H-planes of the measured and simulated planar 3x3 array in polar and Cartesian form with desired radiation toward $\theta_0 = 25\,°$

The realized gain of the fabricated array with radiation toward $\theta_0 = 20\,°$ is about 2 dB greater than for the array with radiation toward $\theta_0 = 25\,°$.

The radiation patterns in the H-plane toward a desired radiation of $\theta_0 = 30\,°$ are displayed in figure 5.40 for the measured and simulated planar array.

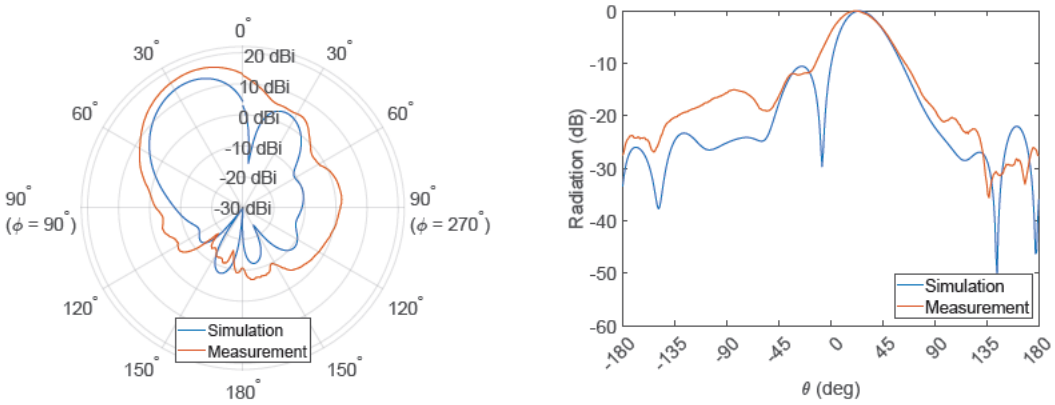

(a) Polar (b) Cartesian

Figure 5.40: H-planes of the measured and simulated planar 3x3 array in polar and Cartesian form with desired radiation toward $\theta_0 = 30\,°$

The beam steering in the H-plane toward a desired radiation of $\theta_0 = 35\,°$ is shown in figure 5.41 for the measured and simulated planar array.

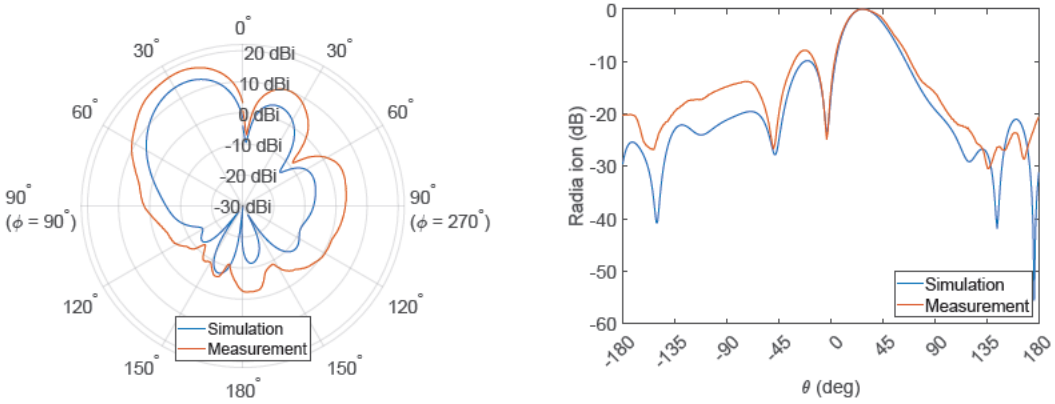

(a) Polar (b) Cartesian

Figure 5.41: H-planes of the measured and simulated planar 3x3 array in polar and Cartesian form with desired radiation toward $\theta_0 = 35\,°$

Figure 5.40 shows a noticeable variation in the achieved scan angle. The achieved scan angle in the simulation is 25 °, whereas the fabricated array achieves a scan angle of 20 °. From figure 5.41b it is apparent that the relative sidelobe level of the fabricated array is greater than −10 dB. Thus, the corresponding scan angle of $\theta_0 = 27\,°$ does not fulfill the requirements.

The performance of the simulated and measure planar array is listed in table 5.12 for beam steering in the H-plane.

D. scan	**A. scan angle θ_0**		**Realized gain**		**Relative sidelobe level**	
angle θ_0	**Simu.**	**Measure.**	**Simu.**	**Measure.**	**Simu.**	**Measure.**
$-35\,^\circ$	$-28\,^\circ$	$-34\,^\circ$	13,94 dBi	18,44 dBi	$-9{,}98$ dB	$-7{,}04$ dB
$-30\,^\circ$	$-25\,^\circ$	$-28\,^\circ$	14,15 dBi	17,46 dBi	$-10{,}64$ dB	$-8{,}73$ dB
$-25\,^\circ$	$-21\,^\circ$	$-22\,^\circ$	14,29 dBi	17,39 dBi	$-11{,}18$ dB	$-10{,}13$ dB
$-20\,^\circ$	$-17\,^\circ$	$-21\,^\circ$	14,41 dBi	17,73 dBi	$-11{,}81$ dB	$-9{,}23$ dB
$-15\,^\circ$	$-13\,^\circ$	$-13\,^\circ$	14,53 dBi	18,82 dBi	$-12{,}88$ dB	$-15{,}36$ dB
$-10\,^\circ$	$-8\,^\circ$	$-14\,^\circ$	14,67 dBi	17,78 dBi	$-14{,}7$ dB	$-11{,}7$ dB
$-5\,^\circ$	$-4\,^\circ$	$-9\,^\circ$	14,79 dBi	18,72 dBi	$-17{,}43$ dB	$-13{,}96$ dB
$0\,^\circ$	$0\,^\circ$	$0\,^\circ$	14,83 dBi	20,78 dBi	$-20{,}14$ dB	$-14{,}45$ dB
$5\,^\circ$	$4\,^\circ$	$3\,^\circ$	14,8 dBi	17,37 dBi	$-16{,}96$ dB	$-15{,}18$ dB
$10\,^\circ$	$8\,^\circ$	$4\,^\circ$	14,69 dBi	17,65 dBi	$-14{,}48$ dB	$-17{,}64$ dB
$15\,^\circ$	$12\,^\circ$	$11\,^\circ$	14,57 dBi	18,8 dBi	$-12{,}79$ dB	$-18{,}66$ dB
$20\,^\circ$	$17\,^\circ$	$18\,^\circ$	14,45 dBi	18,46 dBi	$-11{,}76$ dB	$-10{,}36$ dB
$25\,^\circ$	$21\,^\circ$	$19\,^\circ$	14,35 dBi	16,31 dBi	$-11{,}13$ dB	$-11{,}13$ dB
$30\,^\circ$	$25\,^\circ$	$20\,^\circ$	14,21 dBi	17,01 dBi	$-10{,}55$ dB	$-11{,}94$ dB
$35\,^\circ$	$28\,^\circ$	$27\,^\circ$	14 dBi	17,85 dBi	$-9{,}86$ dB	$-7{,}88$ dB

Table 5.12: Comparison of the simulated and measured parameters of the planar 3x3 array for scanning in the H-plane

Similar to the scan in the E-plane, there is a huge difference in realized gain. On the one hand, the simulation and measurement differ and, on the other hand, there is a great variation in the measured realized gain. The maximum deviation between simulation and measurement is about 6 dB and the maximum variation in the measured values is 4,47 dB. Nevertheless, the Cartesian figures illustrate good agreement between the simulated and measured shapes. The relative sidelobe level becomes greater than -10 dB for $\theta_0 = 27\,^\circ$ and $\theta_0 = -21\,^\circ$. However, there is a measurement with $\theta_0 = -22\,^\circ$ and a relative sidelobe level of $-10{,}13$ dB. Therefore, a scan range from $-22\,^\circ$ to $20\,^\circ$ is assumed in the H-plane. Relative sidelobe levels below -10 dB are measured for these scan angles.

5.7.2 Performance of the fabricated planar array

Achieved scan angle

The achieved scan angles of the fabricated planar array partially differ from the simulation. A maximum deviation of 7 ° in the E-plane and of 6 ° in the H-plane is measured. Section 5.4 describes the reasons for deviations in the scan angle.

Realized gain

The measured realized gain of the fabricated planar array is consequently greater than that of the simulated one. For this reason, the radiation of the horn antenna is examined again. Initially, the measurement setup described in section 5.4 was aligned before the measurements of the fabricated antennas. For reasons of comparison the realized gain of all fabricated antennas is estimated with the same measured data set of the reference antenna for the E-plane and H-plane, respectively. Further measurements of the reference antenna are performed in E-plane and H-plane to verify its realized gain. It is observed that there are huge variations in the measured radiation of the reference antenna. The measurement results of the first and second measurement sequence are listed in table 5.13.

Measurement	**Measured realized gain E-p.**	**Measured realized gain H-p.**
First sequence	−55,46 dB	−54,94 dBi
Second sequence	−56,31 dB	−60,29 dBi

Table 5.13: Measured maximum realized gain of the reference antenna in E-plane and H-plane

The measured realized gain of the second sequence is less than in the first sequence. Especially, the realized gain variation in the H-plane is huge. Small changes in the alignment of the receiver antenna can be caused due to a slight touch. As about 1,5 months have passed between the two measurement sequences, it is assumed that the initial alignment is distorted. The offset is apparent from table 5.13 and is −0,85 dB in E-plane and −5,35 dB in H-plane. According to equation D.1, the realized gain of the planar array would increase in relation to the results of the second sequence.

The considerations of the reference antenna reveal that the measurement setup is inaccurate and the results suffer from reproducibility. A better setup is required for more precise results.

All resonant frequencies of the antenna elements are slightly greater than 5,6 GHz (see table 5.10). Therefore, the input impedance of the elements at 5,6 GHz, that are listed in appendix G.3, are worse than in the simulation. As the realized gain depends on a matched input impedance, it is assumed that the realized gain of the fabricated planar array is less than that of the simulated one.

Relative sidelobe level

Overall, the measure relative sidelobe level of the fabricated planar array are acceptable. Deviations between simulation and measurement can be explained with inaccuracies in the measurement setup. Good agreements in the pattern shape are obtained as well. Due to the measurement setup, the magnitude excitation of the array is nonuniform. Favorable nonuniform magnitude distributions can cause small sidelobes. Common techniques to design low sidelobe arrays use nonuniform magnitude distributions such as binomial or *Tschebyscheff* [1, p. 323]. As an example, it is assumed that the magnitude distribution of the measured patterns for $\theta_0 = 0\,^\circ$ and $\theta_0 = -5\,^\circ$ cause the relative sidelobe levels below $-23\,\mathrm{dB}$ (see table 5.11).

Table 5.14 summarizes the overall performance of the planar array and compares the measured values with the requirements. For reasons of clarity, the figures of merit are listed for E- and H-plane. The values are taken from table 5.11 and 5.12.

Parameter	**Required**	**Measured**	**Satisfied**
Scan angle θ_0 in E-plane	$> \pm 20\,^\circ$	$-26\,^\circ$ to $24\,^\circ$	✓
Scan angle θ_0 in H-plane	$> \pm 20\,^\circ$	$-22\,^\circ$ to $20\,^\circ$	✓
Relative side lobe level in E-plane	$< -10\,\mathrm{dB}$	$-10{,}57\,\mathrm{dB}$	✓
Relative side lobe level in H-plane	$< -10\,\mathrm{dB}$	$-10{,}13\,\mathrm{dB}$	✓
Realized gain in E-plane	$> 13\,\mathrm{dBi}$	$17{,}87\,\mathrm{dBi}$	✓
Realized gain in H-plane	$> 13\,\mathrm{dBi}$	$16{,}31\,\mathrm{dBi}$	✓
Realized gain variation in E-plane	$< 1\,\mathrm{dB}$	$2{,}36\,\mathrm{dB}$	×
Realized gain variation in H-plane	$< 1\,\mathrm{dB}$	$4{,}47\,\mathrm{dB}$	×
Mutual coupling in E-plane	$< -10\,\mathrm{dB}$	$-14{,}55\,\mathrm{dB}$	✓
Mutual coupling in H-plane	$< -20\,\mathrm{dB}$	$-22{,}46\,\mathrm{dB}$	✓

Table 5.14: Comparison of the measured and required parameters of the planar 3x3 array for the achieved scan range for 5,6 GHz

According to the measurements, the fabricated planar array can scan from $-26\,^\circ$ to $24\,^\circ$ in E-plane and from $-22\,^\circ$ to $20\,^\circ$ in H-plane. For these scan ranges the measured relative sidelobe levels are below $-10\,\mathrm{dB}$ and the realized gain is at least 16 dBi. However, the estimated realized gain is doubtful. The variation in realized gain over the desired scan range is about 4,5 dB. As the required maximum variation is 1 dB, the planar array does not fulfill the defined requirements. Mutual coupling in E-plane is below $-10\,\mathrm{dB}$ and below $-20\,\mathrm{dB}$ in H-plane.

6 Final consideration

6.1 Summary and conclusion

In this thesis, a phased array antenna demonstrator for 5,6 GHz was developed. The demonstrator consists of a junction circuit, phase shifters and a 3x3 planar microstrip array. The junction circuit and nine phase shifters are printed on the same circuit board, which can be attached below the microstrip array. Coaxial cables and SMA connectors are used to connect feed network and antenna.

A 16-way Wilkinson power divider is used for the junction circuit. Nine phase shifters are directly appended to the output ports of the divider. Seven remaining ports of the divider circuit are internally terminated with 50 Ω. The phase shifter is realized by a quadrature hybrid with two identical reflection loads in form of two series-resonated varactor diodes. The feed network is equipped with an internal DC supply for phase tuning. Each phase shifter is manually adjustable through a potentiometer. The developed feed network has a wide relative phase shift range of about 240 ° and constant return loss. However, the circuit suffers from large insertion loss variation, which is about 4,5 dB.

Each rectangular microstrip patch of the 3x3 planar array is fed with a coaxial feed probe. The substrate is 0,76 mm thick *RO4350B* with $\varepsilon_r = 3{,}66$. The array was excited with a uniform magnitude distribution and has a spacing of one-half wavelength in x- and y-direction, respectively. Scanned beams of at least 20 ° with a relative sidelobe level below −10 dB were achieved in E- and H-plane. The measurement setup was adjusted by hand. Therefore, the measurements suffer from inaccuracy. Magnitude and phase errors were caused due to cable flexing. These errors partially affect the achieved scan angle and relative sidelobe level. A more stable mount and more flexible cables are required to eliminate such errors. On the current state, the setup has a poor reproducibility due to the described errors.

Overall, the developed system can demonstrate beam steering and strong directivity toward the desired direction. The realized gain of the planar array is estimated by comparison to a known reference antenna. However, it is observed that this method does not provide good agreement with simulations from *CST Studio Suite*. The realized gain of the fabricated antenna is at least 16,3 dBi for all scan angles, whereas simulations in *CST Studio Suite* have revealed a realized gain of 14,2 dBi. Furthermore, variations in realized gain up to 4,5 dB were measured. It is assumed that the *Gain-Comparison Measurement* is affected by the measurement setup. For the precise determination of the realized gain a more accurate setup is required.

6.2 Outlook

Several components of the phased array antenna demonstrator can be enhanced and create a basis for continuation. Furthermore, an improved measurement setup is crucial for reproducible low-error results.

The phase shifter suffers from large insertion loss variation, which is caused by the parasitic elements of the varactor diodes. By shunting the diodes with a resistor, the parasitic effects can be minimized. A good introduction is provided by [5], where an insertion loss variation of 0,6 dB is achieved. In this way the variation of the exciting magnitudes can be reduced. Furthermore, it is observed that the used coaxial cables strongly affect the magnitude variation and cause phase errors. Thus, smaller cables with higher flexibility should be used.

As the *Gain-Comparison Measurement* is affected by the setup, the gain determination is inaccurate. The mount of the fabricated antenna needs to be strengthened to eliminate the described flatness and rotation error (see section 5.4). Furthermore, the alignment of receiving and transmitting antenna should be adjusted more precise. It is assumed that the gain measurement can be enormously improved.

By the integration of amplifiers into the feed network one can adjust the exciting magnitudes of the antenna. This enables to excite the antenna with a nonuniform magnitude distribution. In this way one can adjust the shape of the radiation pattern and minimize the sidelobes. A good introduction is provided by [1, p. 323-345], where the theory to nonuniform distributions is explained.

The bandwidth of the fabricated microstrip patches is about 2 %. One can increase the bandwidth by feeding the patch with a noncontacting feed. As such methods are complicate to fabricate, the feasibility has to be examined through practical tests. Another method to enhance the bandwidth is to stick a parasitic patch and a probe-feed patch together. It is assumed that stacked patches can be fabricated at *HAW Hamburg*. In [13, p. 84] the bandwidth enhancement of such antennas is shown. Typical achievements are bandwidths of 10 % to 20 %.

As the measurement effort of the planar array is enormous, it is recommended to place emphasis on linear arrays. By increasing the number of elements, one can achieve wider scan angles. An example of a linear six-element array is shown in the electronic appendix A.16.

Bibliography

[1] Balanis, C. A.: *Antenna Theory: Analysis and Design*. 4th edition. John Wiley and Sons, 2016

[2] Carver, K. ; Mink, J.: Microstrip antenna technology. In: *IEEE Transactions on Antennas and Propagation* 29 (1981), Nr. 1, S. 2–24

[3] Derneryd, A. ; Lind, A.: Extended analysis of rectangular microstrip resonator antennas. In: *IEEE Transactions on Antennas and Propagation* 27 (1979), Nr. 6, S. 846–849

[4] Kark, K. W.: *Antennen und Strahlungsfelder*. Springer, 2017. – ISBN 9783658139650

[5] Lin, Chien-San ; Chang, Sheng-Fuh ; Chang, Chia-Chan ; Shu, Yi-Hao: Design of a Reflection-Type Phase Shifter With Wide Relative Phase Shift and Constant Insertion Loss. In: *IEEE Transactions on Microwave Theory and Techniques* 55 (2007), Nr. 9, S. 1862–1868

[6] Mailloux, R. ; McIlvenna, J. ; Kernweis, N.: Microstrip array technology. In: *IEEE Transactions on Antennas and Propagation* 29 (1981), Nr. 1, S. 25–37

[7] EPCOS AG: Multilayer ceramic capacitors. (2006). – URL `https://www.modelithics.com/models/Vendor/Epcos/B37930K5.pdf`. – Last access 01.08.2021

[8] Rogers Corporation: *RO4000 Series*. Rogers Corporation, 2018. – URL `https://rogerscorp.com/-/media/project/rogerscorp/documents/advanced-connectivity-solutions/english/data-sheets/ro4000-laminates-ro4003c-and-ro4350b---data-sheet.pdf`. – Last access 01.08.2021

[9] Skyworks Solutions: *SMV123x Series: Hyperabrupt Junction Tuning Varacots*. Skyworks Solutions, 2020. – URL `https://www.skyworksinc.com/-/media/SkyWorks/Documents/Products/101-200/SMV123x_Series_200058AA.pdf`. – Last access 01.08.2021

[10] Würth Elektronik eiSos GmbH & Co.KG: WE-CAIR Air coil 744910054. (2021). – URL `https://www.we-online.de/catalog/datasheet/744910054.pdf`. – Last access 01.08.2021

[11] Pozar, D.M.: Input impedance and mutual coupling of rectangular microstrip antennas. In: *IEEE Transactions on Antennas and Propagation* 30 (1982), Nr. 6, S. 1191–1196

[12] Pozar, D.M.: A microstrip antenna aperture coupled to a microstrip line. In: *Electronics Letters* 21 (1985), Nr. 2, S. 49–50

[13] Pozar, D.M.: Microstrip antennas. In: *Proceedings of the IEEE* 80 (1992), Nr. 1, S. 79–91

[14] Pozar, D.M.: *Microwave Engineering*. John Wiley and Sons, 2004

[15] Pozar, D.M. ; Kaufman, B.: Increasing the bandwidth of a microstrip antenna by proximity coupling. In: *Electronics Letters* 23 (1987), Nr. 8, S. 368–369

[16] Pozar, D.M. ; Kaufman, B.: Design considerations for low sidelobe microstrip arrays. In: *IEEE Transactions on Antennas and Propagation* 38 (1990), Nr. 8, S. 1176–1185

[17] Pues, H.F. ; Capelle, A.R. Van de: An impedance-matching technique for increasing the bandwidth of microstrip antennas. In: *IEEE Transactions on Antennas and Propagation* 37 (1989), Nr. 11, S. 1345–1354

[18] Schrank, H.: Low sidelobe phased array antennas. In: *IEEE Antennas and Propagation Society Newsletter* 25 (1983), Nr. 2, S. 4–9

Appendix

A Guide for the electronic appendix

A data medium is attached to this thesis. The structure of the data medium can be obtained from the following.

A.1 Simulation of the phase shifter

- **Simulation file in *AWR*:**
  SimulationResults\MicrostripCircuits\PhaseShifter\Design\

A.2 Measurements results of the phase shifter

- **Measurement results in *AWR*:**
  MeasurementResults\MicrostripCircuits\PhaseShifter\Analysis\
- **Scattering parameters:**
  MeasurementResults\MicrostripCircuits\PhaseShifter\ScatteringParameters\

A.3 Simulation of the two-way Wilkinson power divider in *AWR*

- **Simulation file in *AWR*:**
  SimulationResults\MicrostripCircuits\Two-WayWilkinsonPowerDivider\Design\

A.4 Measurements results of the two-way Wilkinson power divider

- **Measurement results in *AWR*:**
  MeasurementResults\MicrostripCircuits\Two-WayWilkinsonPowerDivider\Analysis\
- **Scattering parameters:**
  MeasurementResults\MicrostripCircuits\Two-WayWilkinsonPowerDivider\
  ScatteringParameters\

A.5 Simulation of the 16-way Wilkinson power divider in *AWR*

- **Simulation file in *AWR*:**
  SimulationResults\MicrostripCircuits\16-WayWilkinsonPowerDivider\Design\

A.6 Measurements results of the 16-way Wilkinson power divider

- **Measurement results in *AWR*:**
  MeasurementResults\MicrostripCircuits\16-WayWilkinsonPowerDivider\Analysis\
- **Scattering parameters:**
  MeasurementResults\MicrostripCircuits\16-WayWilkinsonPowerDivider\
  ScatteringParameters\

A.7 Layout of the feed network module in *AWR*

- **Simulation file in *AWR*:**
  SimulationResults\MicrostripCircuits\FeedNetworkModule\Design\

A.8 Measurement results of the feed network module in *AWR*

- **Measurement results in *AWR*:**
  MeasurementResults\MicrostripCircuits\FeedNetworkModule\Analysis\
- **Scattering parameters:**
  MeasurementResults\MicrostripCircuits\FeedNetworkModule\
  ScatteringParameters\

A.9 Simulation of the microstrip antenna in *CST*

- **Simulation file in *CST*:**
  SimulationResults\Antennas\MicrostripAntenna\Design\
- **Scattering parameters:**
  SimulationResults\Antennas\MicrostripAntenna\ScatteringParameters\
- **Radiation characteristic:**
  SimulationResults\Antennas\MicrostripAntenna\RadiationCharacteristic\

A.10 Measurement of the microstrip antenna

- **Measurement results in *AWR*:**
  MeasurementResults\Antennas\MicrostripAntenna\Analysis\
- **Scattering parameters:**
  MeasurementResults\Antennas\MicrostripAntenna\ScatteringParameters\
- **Radiation characteristic:**
  MeasurementResults/Antennas/MicrostripAntenna/RadiationCharacteristic/

A.11 Simulation of the linear three-element array in *CST*

- **Simulation file in *CST*:**
  SimulationResults\Antennas\LinearArray\Design\
- **Scattering parameters:**
  SimulationResults\Antennas\LinearArray\ScatteringParameters\
- **Radiation characteristic:**
  SimulationResults\Antennas\LinearArray\RadiationCharacteristic\

A.12 Measurement of the linear three-element array

- **Measurement results in *AWR*:**
  MeasurementResults\Antennas\LinearArray\Analysis\
- **Scattering parameters:**
  MeasurementResults\Antennas\LinearArray\ScatteringParameters\
- **Radiation characteristic:**
  MeasurementResults\Antennas\LinearArray\RadiationCharacteristic\

A.13 Simulation of the planar 3x3 array in *CST*

- **Simulation file in *CST*:**
  SimulationResults\Antennas\PlanarArray\Design\
- **Scattering parameters:**
  SimulationResults\Antennas\PlanarArray\ScatteringParameters\
- **Radiation characteristic:**
  SimulationResults\Antennas\PlanarArray\RadiationCharacteristic\

A.14 Measurement of the planar 3x3 array

- **Measurement results in *AWR*:**
  MeasurementResults\Antennas\PlanarArray\Analysis\
- **Scattering parameters:**
  MeasurementResults\Antennas\PlanarArray\ScatteringParameters\
- **Radiation characteristic:**
  MeasurementResults\Antennas\PlanarArray\RadiationCharacteristic\

A.15 Measurement results of the reference antenna

- **Radiation characteristic:**
  MeasurementResults\Antennas\ReferenceAntenna\RadiationCharacteristic\

A.16 Simulation of the linear six-element array in *CST*

- **Simulation file in *CST*:**
  SimulationResults\Antennas\LinearArraySixElements\Design\

A.17 *SPICE* model of the varactor diode *SMV1231*

- ***SPICE* model:**
  FurtherInformation\VaractorDiode\

A.18 Scattering parameters of the *WE-CAIR Air coil*

- **Scattering parameters:**
  FurtherInformation\Coil\

A.19 Matlab source code for plot creation

- **Matlab scripts:**
  FurtherInformation\Matlab\

B Formulas

The characteristic impedance of a coaxial cable is given by [4, p. 168]

$$Z = \frac{Z_F}{2\,\pi\sqrt{\varepsilon_r}} ln\Big(\frac{D}{d}\Big), \tag{B.1}$$

where Z_F is the impedance of free space.

C Extended presentation of the phase shifter

C.1 Initial phase shifter design

The simulation and measurement result of the first phase shifter design, where the microstrip line between the diodes has a length of 3,67 mm, are shown in the following. The design is not used as it does not provide enough relative phase shift.

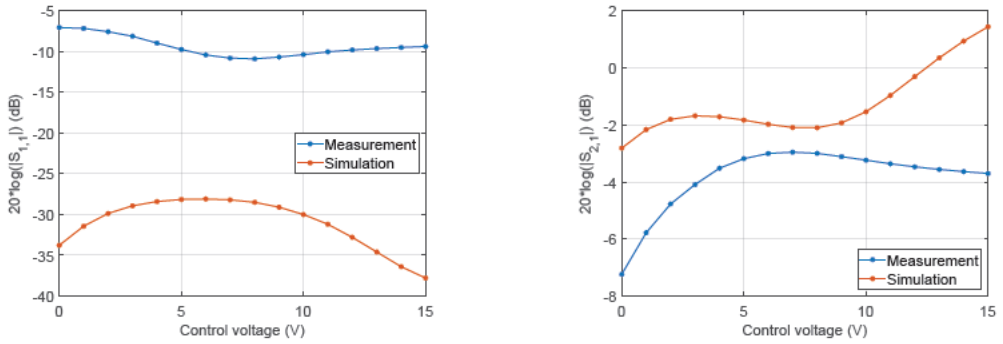

(a) Return loss (b) Insertion loss

Figure C.1: Simulated and measured performance of the phase shifter versus control voltage at 5,6 GHz

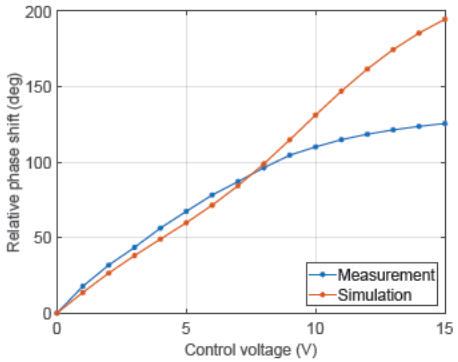

Figure C.2: Simulated and measured relative phase shift of the phase shifter versus control voltage at 5,6 GHz

The poor return loss and insertion loss variation in the measurement is due to the absence of bends in the feed lines.

C.2 Bandwidth of the simulated phase shifter

The insertion loss, return loss and the relative phase shift versus control voltage are shown for 5,32 GHz and 5,88 GHz.

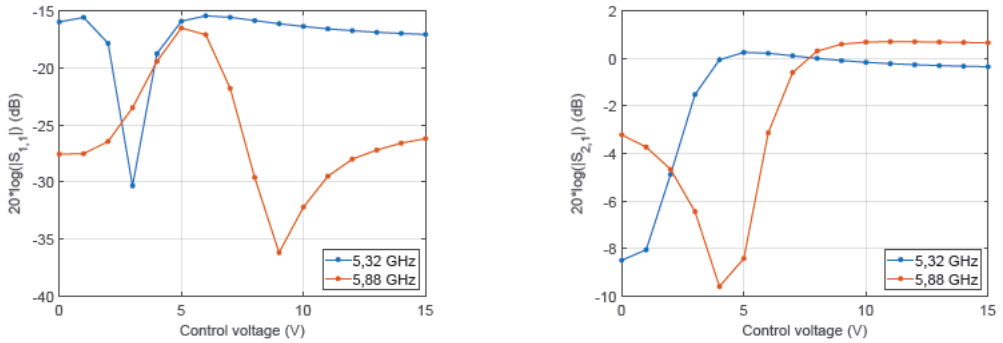

(a) Return loss (b) Insertion loss

Figure C.3: Simulated performance of the phase shifter versus control voltage at 5,32 GHz and 5,88 GHz

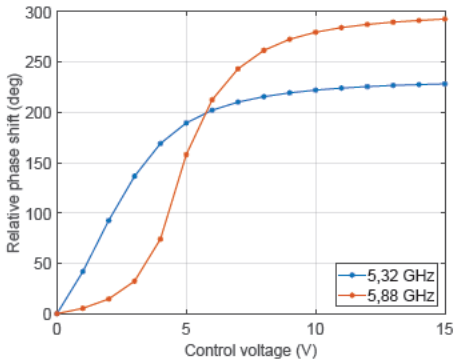

Figure C.4: Simulated relative phase shift of the phase shifter versus control voltage at 5,32 GHz and 5,88 GHz

C.3 Bandwidth of the measured phase shifter

The insertion loss, return loss and the relative phase shift versus control voltage are shown for 5,32 GHz and 5,88 GHz.

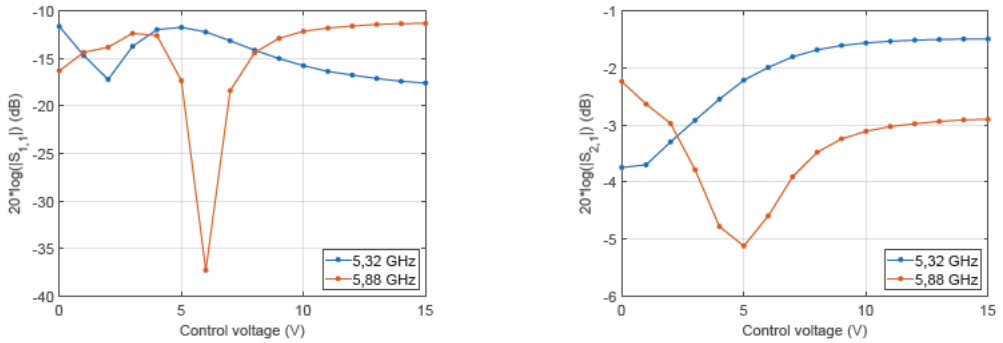

(a) Return loss (b) Insertion loss

Figure C.5: Measured performance of the phase shifter versus control voltage at 5,32 GHz and 5,88 GHz

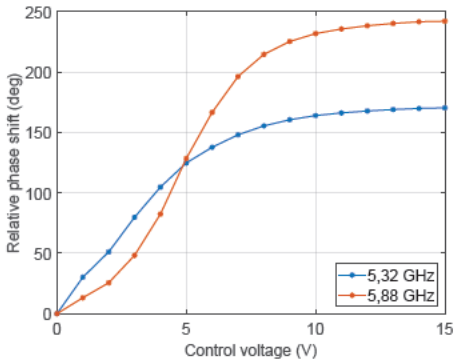

Figure C.6: Measured relative phase shift of the phase shifter versus control voltage at 5,32 GHz and 5,88 GHz

D Measurement of the realized gain

The horn antenna *Quad Ridged Broadband Horn Antenna QRH11* from *RFspin s.r.o.* is used to determine the realize gain of all fabricated antennas. To establish identical conditions, all measurements include the phase shifter, which is placed between network analyzer and antenna. Only the realized gain in the E-plane and H-plane of the reference antenna is known. Therefore, the realized gain of the fabricated antennas can be roughly determined by comparison of the measured realized gain to that of the reference antenna. The realized gain of an antenna under test (AUT) is estimated by

$$G_{re}(\text{AUT}) = G_{re}(\text{Horn antenna}) - \big(|G_{re,measured}(\text{AUT})| - |G_{re,measured}(\text{Horn antenna})|\big). \tag{D.1}$$

The measured values and the determined realized gain in the E-plane are shown in table D.1. The values of the array are related to broadside radiation.

Antenna	**Measured realized gain**	**Determined realized gain**
Horn antenna	−55,46 dB	12,2 dBi
Microstrip antenna	−61,27 dB	6,39 dBi
Linear three-element array	−56,08 dB	11,58 dBi
Planar 3x3 array	−49,79 dB	17,87 dBi

Table D.1: Measurement values of the realized gain in the E-plane

The measured values and the determined realized gain in the H-plane are shown in table D.2.

Antenna	**Measured realized gain**	**Determined realized gain**
Horn antenna	−54,94 dB	12,3 dBi
Microstrip antenna	−61,51 dB	5,73 dBi
Linear three-element array	−56,05 dB	11,19 dBi
Planar 3x3 array	−46,46 dB	20,78 dBi

Table D.2: Measurement values of the realized gain in the H-plane

The data sets of the measurement results of the horn antenna can be obtained in the electronic appendix A.15. The realized gain of all fabricated antennas is estimated in relation to the data sets *HornAntennaE.txt* and *HornAntennaH.txt*.

E Extended presentation of the feed network module

E.1 Performance of the feed network module

Port	Measured relative phase shift
2	243,03 °
3	239,06 °
4	250,41 °
5	246,85 °
6	251,85 °
7	243,04 °
8	259,81 °
9	247,44 °
10	242,72 °

Table E.1: Measured relative phase shift of the feed network module at 5,6 GHz

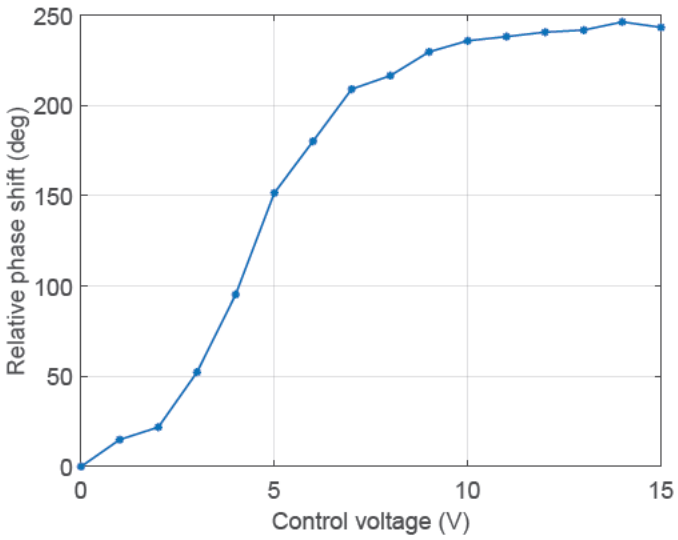

Figure E.1: Exemplary measured relative phase shift at port 2 of the feed network module versus control voltage at 5,6 GHz

The measurements above are performed after the fabrication of the circuit. As the SMA connector are not suitable for intensive use, the performance of the module can change. Referring to table 5.7, where the adjusted phases and magnitudes for the linear array are listed, one can see that the insertion loss suffers from intensive use. It is observed that the insertion loss decreases over time.

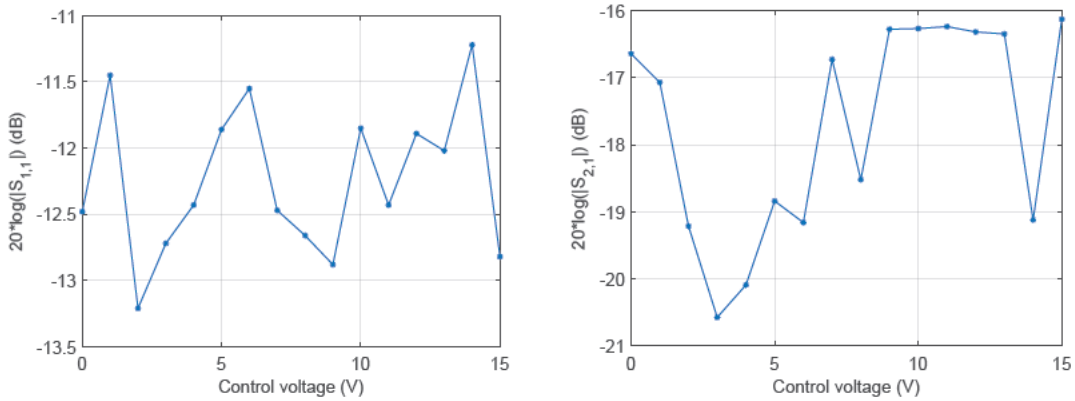

(a) Return Loss $|S_{1,1}|$ (b) Insertion Loss $|S_{2,1}|$

Figure E.2: Exemplary performance of the feed network module versus control voltage at 5,6 GHz

E.2 Radiation of the feed network module

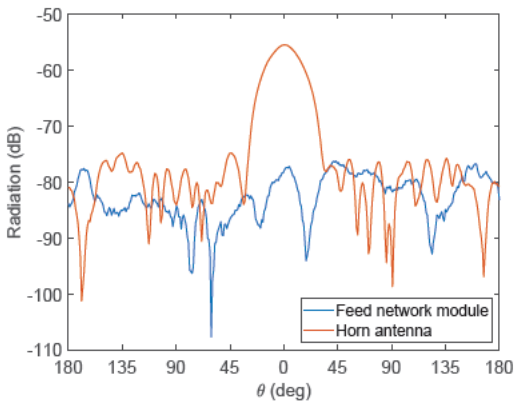

Figure E.3: Radiation of the Feed network module and the horn antenna in the E-plane

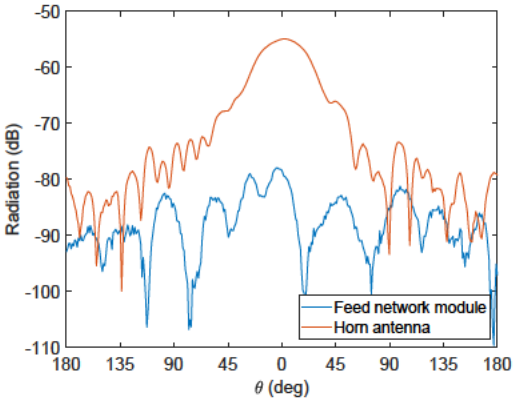

Figure E.4: Radiation of the Feed network module and the horn antenna in the H-plane

The maximum radiation of the feed network module relative to the maximum of the horn antenna is attenuated by $-20{,}79\,\mathrm{dB}$ in the E-plane and $-23{,}05\,\mathrm{dB}$ in the H-plane.

F Extended presentation of the linear three-element array

F.1 Beam steering in the E-plane

In the following the patterns for desired radiation toward $\theta_0 = 30\,°$ and $\theta_0 = 30\,°$ for $\phi_0 = 0\,°$ are displayed. Furthermore all simulated and measured patterns for beam steering toward $\phi_0 = 180\,°$ are shown.

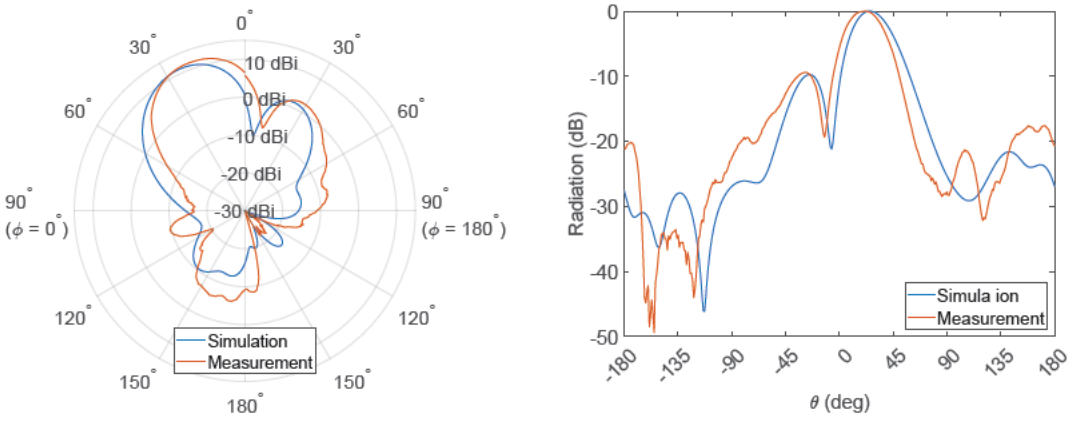

(a) Polar (b) Cartesian

Figure F.1: E-planes of the measured and simulated linear three-element array in polar and Cartesian form with desired radiation toward $\theta_0 = 30\,°$

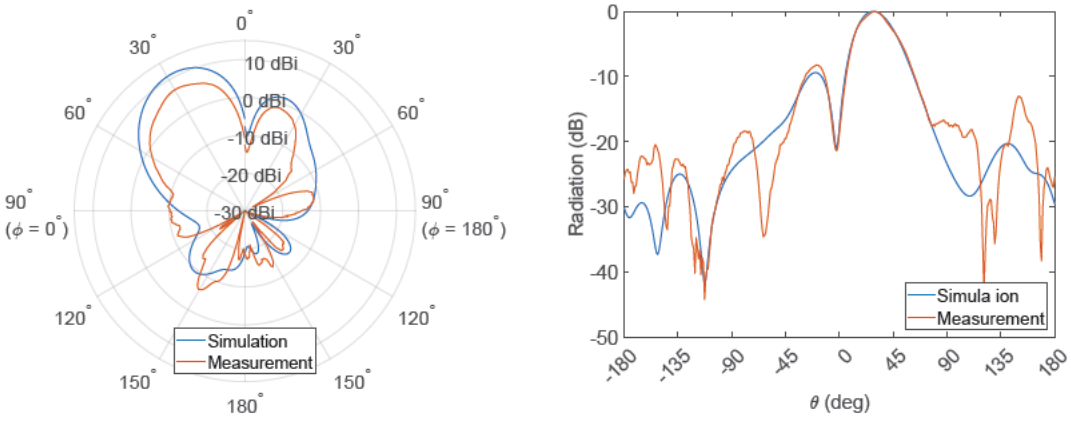

(a) Polar (b) Cartesian

Figure F.2: E-planes of the measured and simulated linear three-element array in polar and Cartesian form with desired radiation toward $\theta_0 = 35\,°$

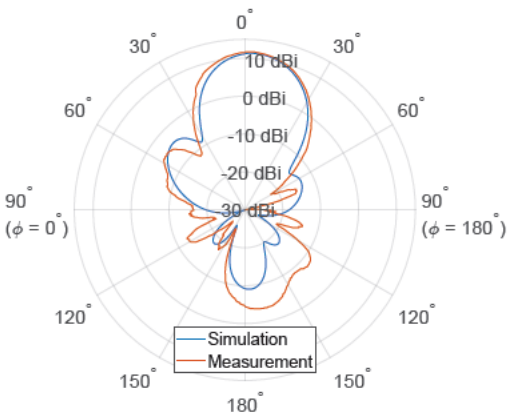

(a) Polar

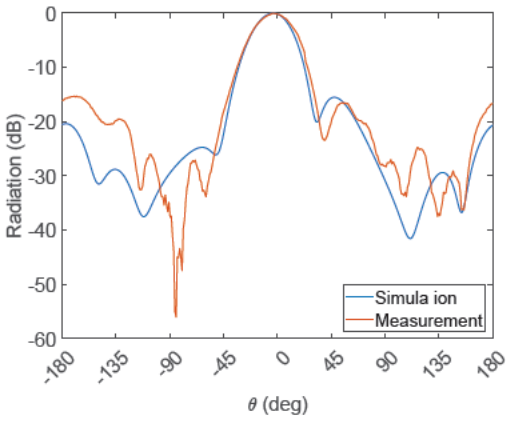

(b) Cartesian

Figure F.3: E-planes of the measured and simulated linear three-element array in polar and Cartesian form with desired radiation toward $\theta_0 = -5\,°$

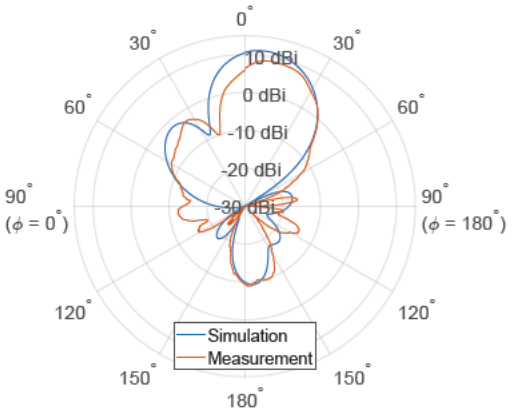

(a) Polar

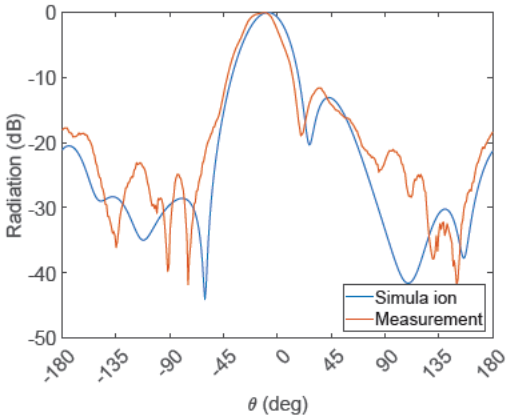

(b) Cartesian

Figure F.4: E-planes of the measured and simulated linear three-element array in polar and Cartesian form with desired radiation toward $\theta_0 = -10\,°$

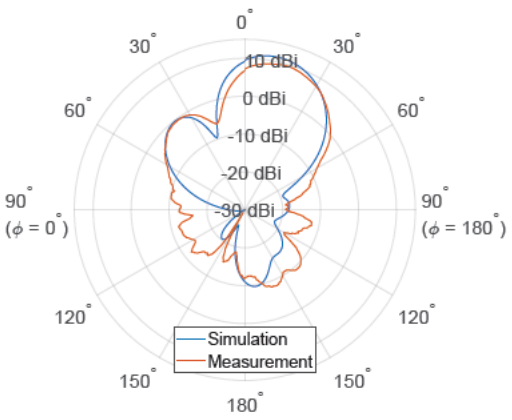

(a) Polar

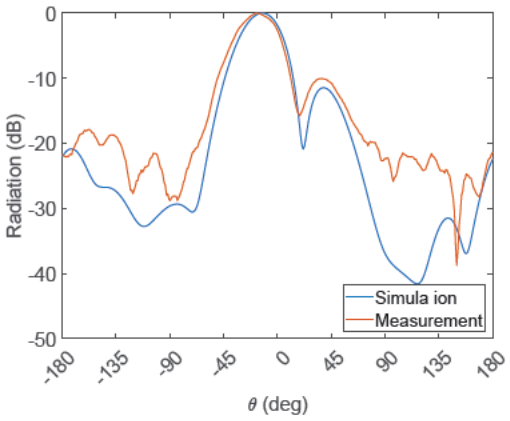

(b) Cartesian

Figure F.5: E-planes of the measured and simulated linear three-element array in polar and Cartesian form with desired radiation toward $\theta_0 = -15\,°$

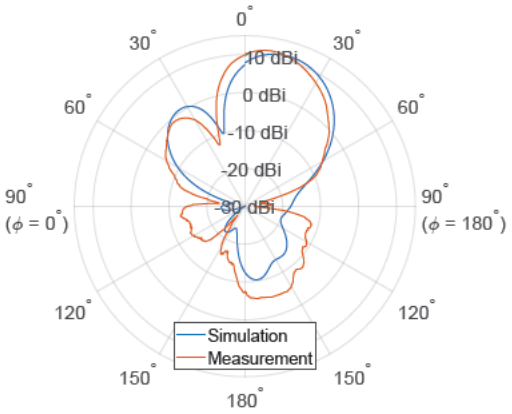

(a) Polar

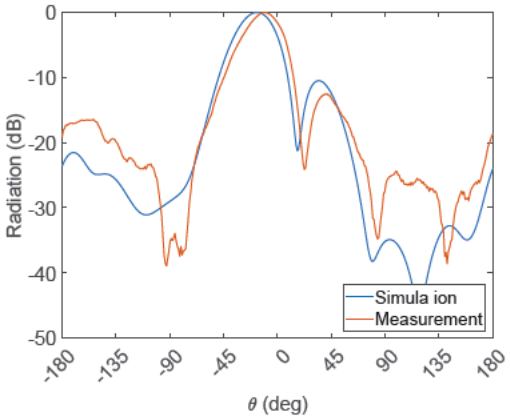

(b) Cartesian

Figure F.6: E-planes of the measured and simulated linear three-element array in polar and Cartesian form with desired radiation toward $\theta_0 = -20\,°$

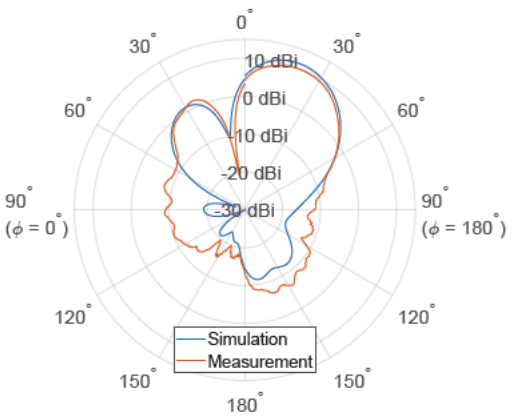

(a) Polar

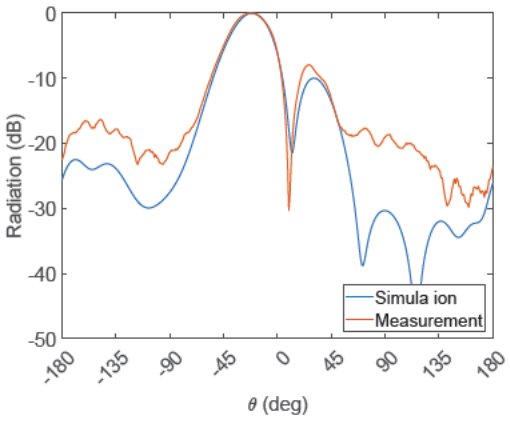

(b) Cartesian

Figure F.7: E-planes of the measured and simulated linear three-element array in polar and Cartesian form with desired radiation toward $\theta_0 = -25\,°$

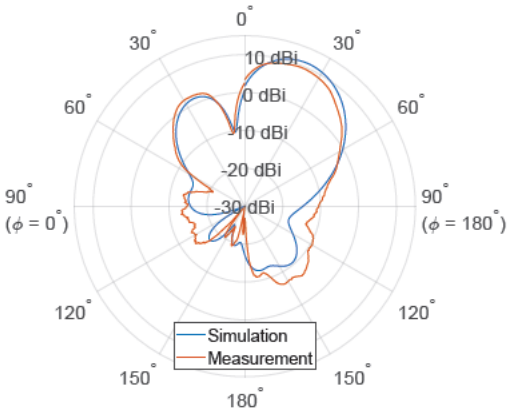

(a) Polar

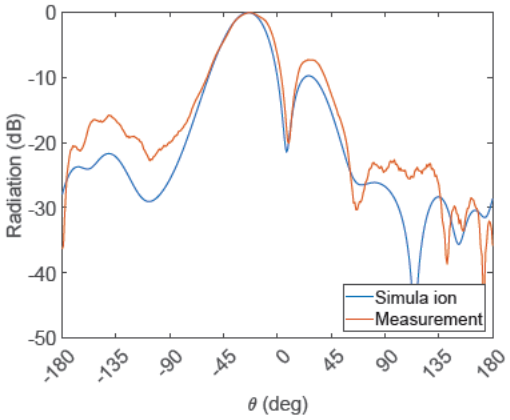

(b) Cartesian

Figure F.8: E-planes of the measured and simulated linear three-element array in polar and Cartesian form with desired radiation toward $\theta_0 = -30\,°$

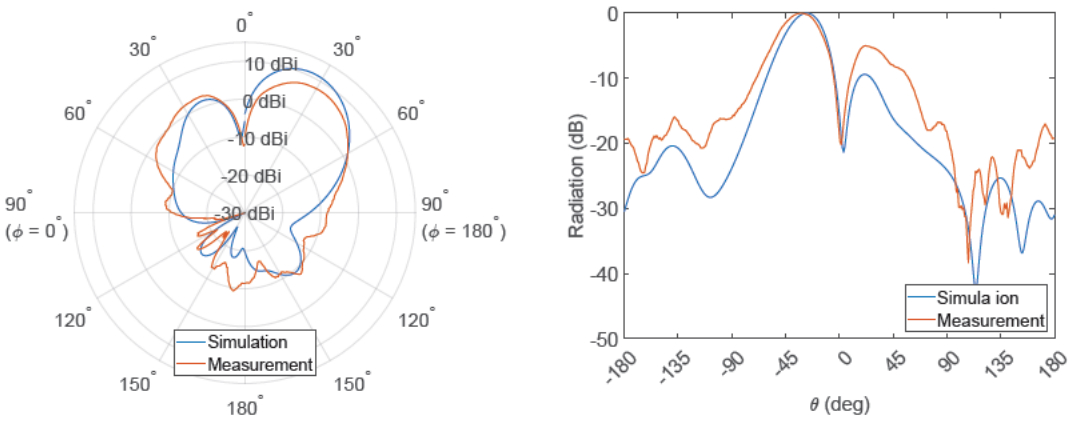

(a) Polar (b) Cartesian

Figure F.9: E-planes of the measured and simulated linear three-element array in polar and Cartesian form with desired radiation toward $\theta_0 = -35\,°$

F.2 Input impedance

Element	Z_{in}
1	$(57 + 1{,}5\mathrm{i})\,\Omega$
2	$(53{,}5 - 7{,}5\mathrm{i})\,\Omega$
3	$(52 - \mathrm{i})\,\Omega$

Table F.1: Measured input impedance of the linear three-element array elements at 5,6 GHz

G Extended presentation of the planar 3x3 array

G.1 Beam steering in the E-plane

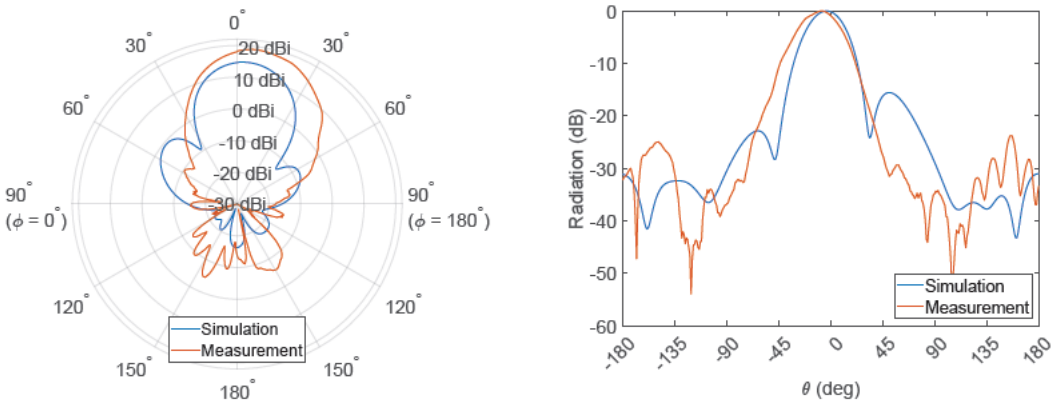

(a) Polar (b) Cartesian

Figure G.1: E-planes of the measured and simulated planar 3x3 array in polar and Cartesian form with desired radiation toward $\theta_0 = -5\,°$

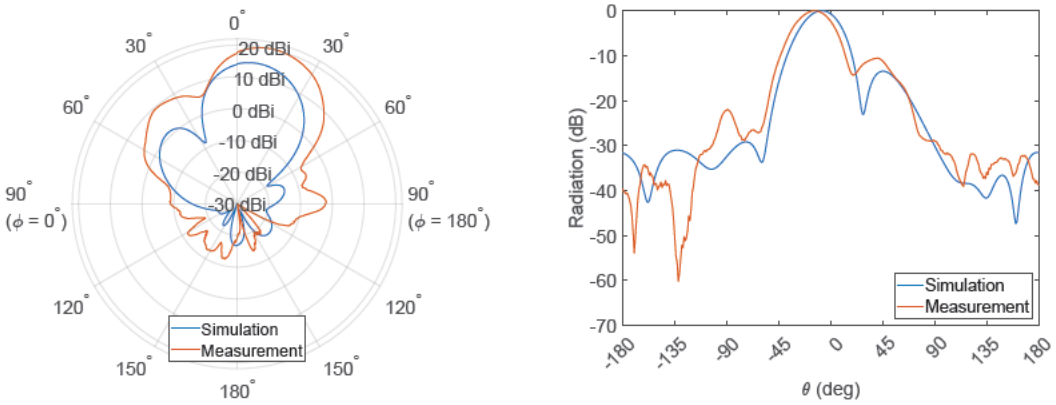

(a) Polar (b) Cartesian

Figure G.2: E-planes of the measured and simulated planar 3x3 array in polar and Cartesian form with desired radiation toward $\theta_0 = -10\,°$

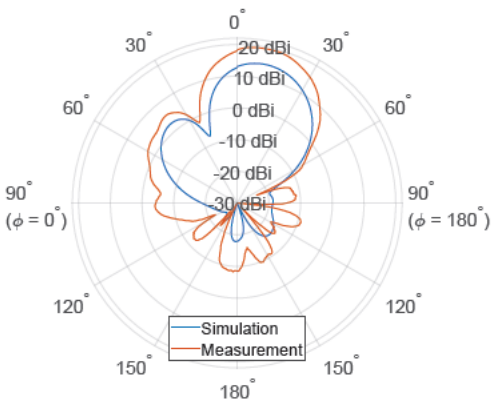

(a) Polar

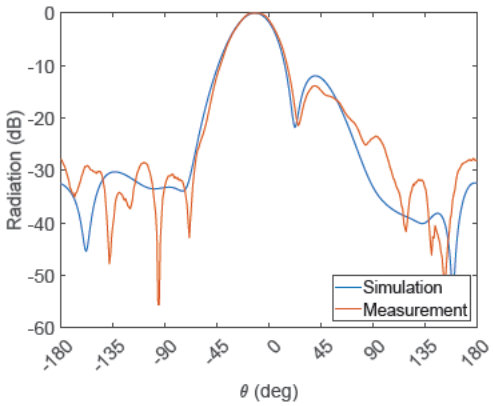

(b) Cartesian

Figure G.3: E-planes of the measured and simulated planar 3x3 array in polar and Cartesian form with desired radiation toward $\theta_0 = -15\,°$

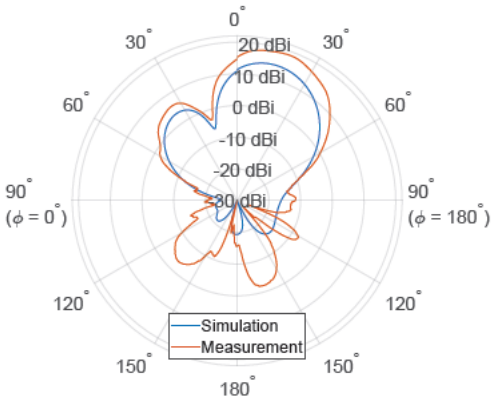

(a) Polar

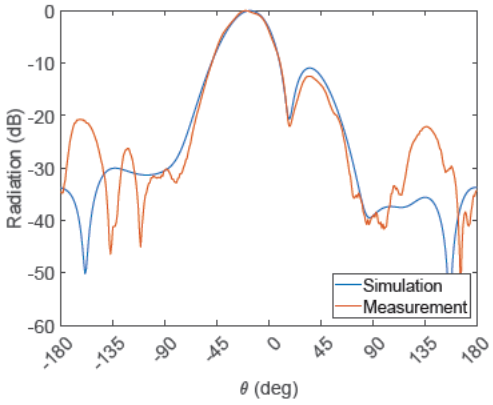

(b) Cartesian

Figure G.4: E-planes of the measured and simulated planar 3x3 array in polar and Cartesian form with desired radiation toward $\theta_0 = -20\,°$

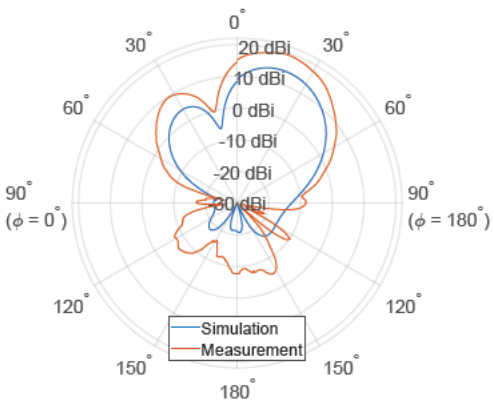

(a) Polar

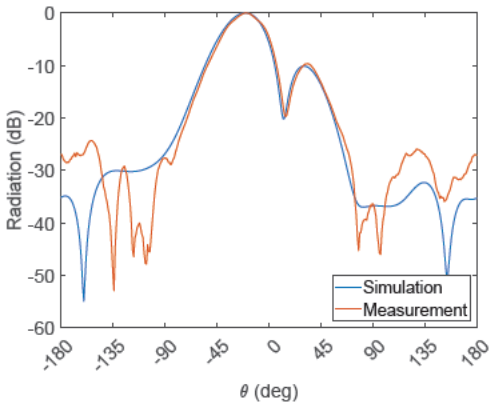

(b) Cartesian

Figure G.5: E-planes of the measured and simulated planar 3x3 array in polar and Cartesian form with desired radiation toward $\theta_0 = -25\,°$

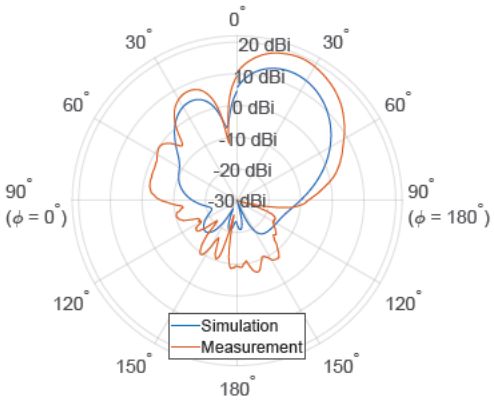

(a) Polar

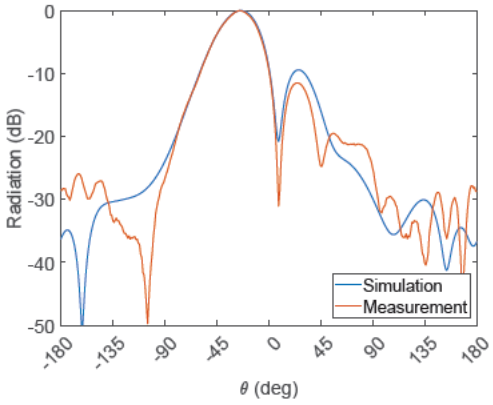

(b) Cartesian

Figure G.6: E-planes of the measured and simulated planar 3x3 array in polar and Cartesian form with desired radiation toward $\theta_0 = -30\,°$

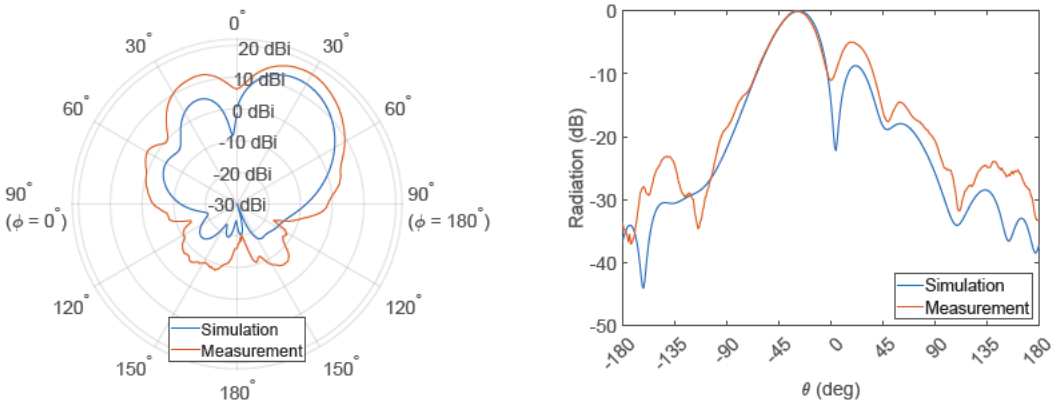

(a) Polar (b) Cartesian

Figure G.7: E-planes of the measured and simulated planar 3x3 array in polar and Cartesian form with desired radiation toward $\theta_0 = -35\,°$

G.2 Beam steering in the H-plane

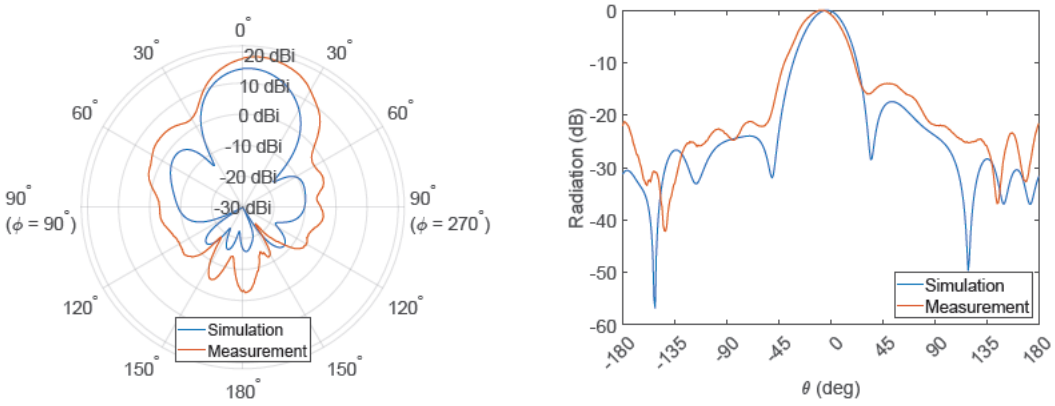

(a) Polar (b) Cartesian

Figure G.8: H-planes of the measured and simulated planar 3x3 array in polar and Cartesian form with desired radiation toward $\theta_0 = -5\,°$

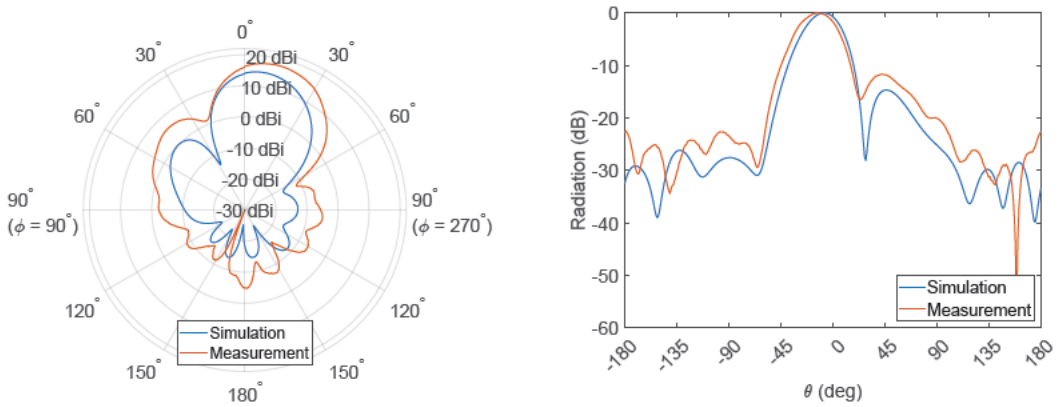

(a) Polar (b) Cartesian

Figure G.9: H-planes of the measured and simulated planar 3x3 array in polar and Cartesian form with desired radiation toward $\theta_0 = -10\,°$

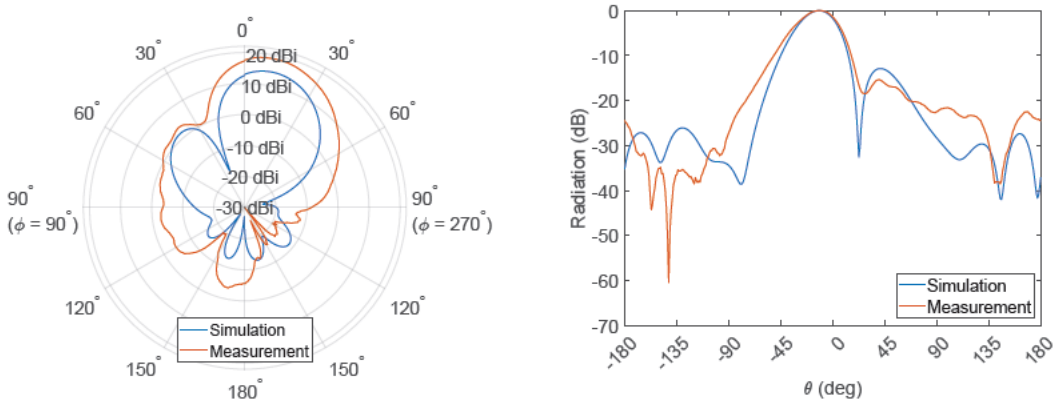

(a) Polar (b) Cartesian

Figure G.10: H-planes of the measured and simulated planar 3x3 array in polar and Cartesian form with desired radiation toward $\theta_0 = -15\,°$

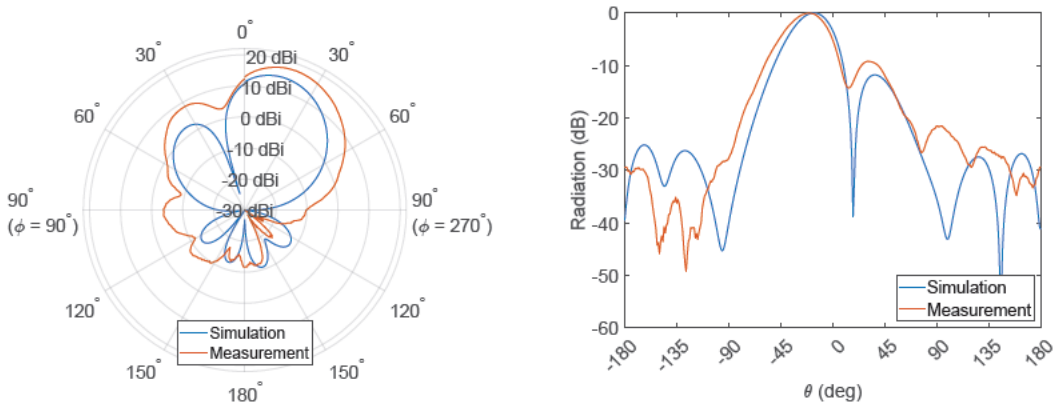

(a) Polar (b) Cartesian

Figure G.11: H-planes of the measured and simulated planar 3x3 array in polar and Cartesian form with desired radiation toward $\theta_0 = -20\,°$

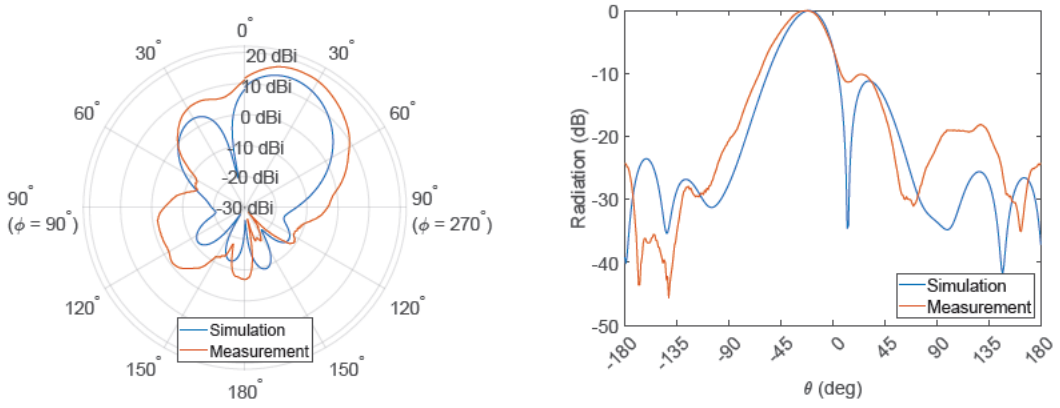

(a) Polar (b) Cartesian

Figure G.12: H-planes of the measured and simulated planar 3x3 array in polar and Cartesian form with desired radiation toward $\theta_0 = -25\,°$

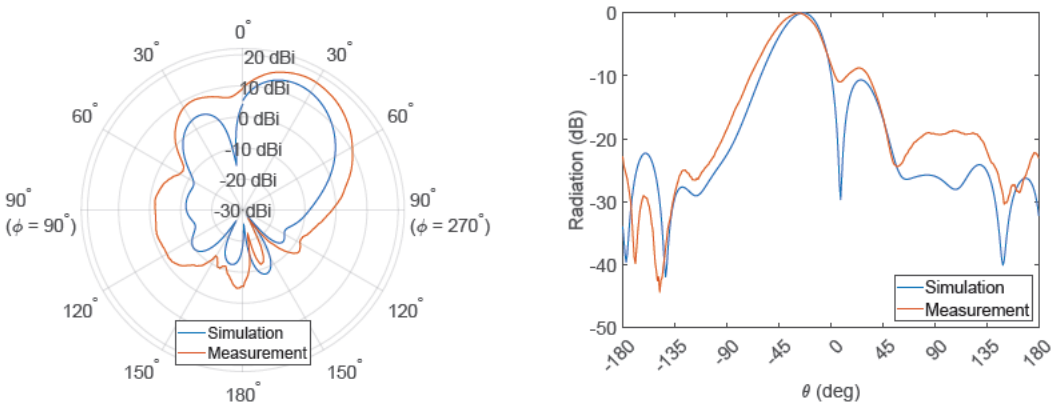

(a) Polar (b) Cartesian

Figure G.13: H-planes of the measured and simulated planar 3x3 array in polar and Cartesian form with desired radiation toward $\theta_0 = -30\,°$

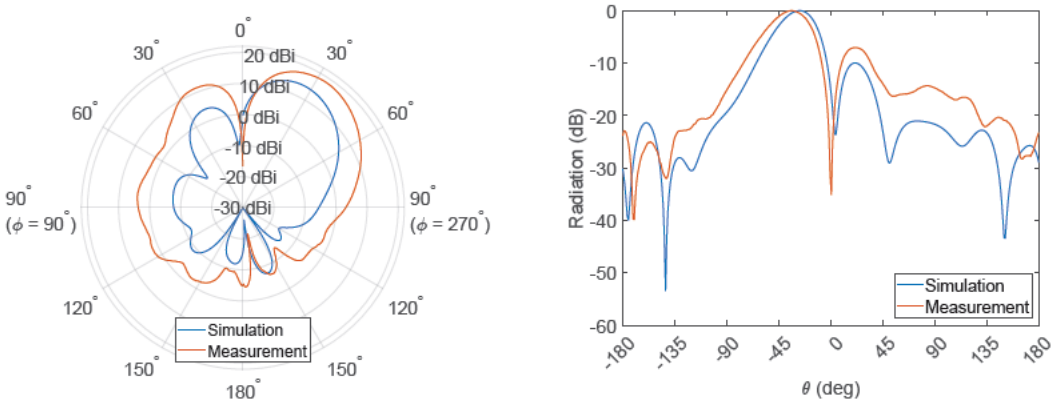

(a) Polar (b) Cartesian

Figure G.14: H-planes of the measured and simulated planar 3x3 array in polar and Cartesian form with desired radiation toward $\theta_0 = -35\,°$

G.3 Input impedance

Element	Z_{in}
1	$(58 - 36\text{i})\,\Omega$
2	$(59 - 24{,}5\text{i})\,\Omega$
3	$(59{,}5 - 18{,}5\text{i})\,\Omega$
4	$(59{,}5 - 20{,}5\text{i})\,\Omega$
5	$(57 - 35\text{i})\,\Omega$
6	$(51 - 20{,}5\text{i})\,\Omega$
7	$(47 - 28{,}5\text{i})\,\Omega$
8	$(50 - 27\text{i})\,\Omega$
9	$(59 - 40{,}5\text{i})\,\Omega$

Table G.1: Measured input impedance of the planar array elements at 5,6 GHz

The real part of the input impedance is well matched, whereas the imaginary part is high. It is assumed that there is an error in the feed and that there are variations in the substrate.

Erklärung zur selbstständigen Bearbeitung einer Abschlussarbeit

Hiermit versichere ich, dass ich die vorliegende Arbeit ohne fremde Hilfe selbständig verfasst und nur die angegebenen Hilfsmittel benutzt habe. Wörtlich oder dem Sinn nach aus anderen Werken entnommene Stellen sind unter Angabe der Quellen kenntlich gemacht.

Ort | Datum | Unterschrift im Original